Measurement of the Z Boson Transverse Momentum Distribution in $p\bar{p}$ Collisions at $\sqrt{s} = 1.8$ TeV with the DØ Detector

A Dissertation Presented

by

Zhi-Yu Jiang

to

The Graduate School

in Partial Fulfillment of the Requirements

for the Degree of

Doctor of Philosophy

in

Physics

State University of New York
at
Stony Brook

August 1995

State University of New York
at Stony Brook

The Graduate School

Zhi-Yu Jiang

We, the dissertation committee for the above candidate for the Doctor of Philosophy degree, hereby recommend acceptance of the dissertation.

Professor Robert L. McCarthy
Department of Physics

Professor Paul D. Grannis
Department of Physics

Professor Roderich Engelmann
Department of Physics

Professor George Sterman
Department of Physics

Dr. Melvin Month
Brookhaven National Laboratory

This dissertation is accepted by the Graduate School.

Graduate School

To My Parents

Contents

List of Figures

List of Tables

Acknowledgements

First of all, I must thank Professor Bob McCarthy for being an excellent advisor and coach throughout the years of my thesis research at DØ. Bob has been extremely helpful whenever I have problems. His kindness and fairness, experience in physics research, and dedication to students are essential to the completion of this work. Throughout my graduate years at Stony Brook, Professor Paul Grannis has been an example of excellence and constant inspiration. I appreciate the great many comments by Bob and Paul. Although those comments seemed daunting at times, they did help to make the thesis a much better one. I must thank Professor Rod Engelmann for his constant support, his much needed help and guidance during my first few years at Stony Brook, when I first set foot in America and had to adjust to a brand new culture as well as to achieve academic excellence. Without Rod's help and encouragement, I couldn't have gone so far. Professor Harry Weerts has been a driving force for this analysis. I am grateful for his consistent interest and appreciation. Dr. Melvin Month, director of the U.S. Particle Accelerator School (USPAS), has been a source of support, advice and encouragement. Professor George Sterman kindly served on my thesis committee with great theoretical insight.

I am indebted to Professor Claudio Pellegrini for his guidance and support for my two years at Brookhaven National Laboratory doing research on accelerator physics. Professor Chen-Ning Yang kindly acted as my advisor with great encouragement.

I have enjoyed my years at DØ. Everyone at DØ contributed to this work. Professor John Sculli let me take on his Toy Calorimeter Monte Carlo to begin with. Dr. Natalie Roe led the W/Z cross section group with great style, where we have shared our learning experience at DØ. I should thank Professor Michael Rijssenbeek for always having watchful eyes and listening ears to the analysis and Professor Chip Brock for his feedback and information on the latest theoretical development. Many thanks also go to the theorists: Dr. Peter Arnold, Dr. Glenn Ladinsky, and Professor C.-P. Yuan for helping me understand the theory.

When I first moved to Fermilab and joined DØ, Dr. Kathy Streets was a marvelous teacher to guide me through the DØ calorimeter electronics and data aquisition system quickly and to offer invaluable advice to my family. I am always thankful to her.

It has been a pleasure working with Dr. Rich Astur, Dr. Mike Tartaglia, Dr. Norman Graf, Dr. Danilo Puseljic, Dr. Marcel Demarteau, and Dr. Srini Rajagopalan. Rich was always ready to answer my questions and offer help. Dr. Darien Wood generously passed on what he learned with the UA2 detector and I enjoyed many discussions with him.

I'd also like to thank Dr. Haowei Xu, Dr. Jie Yang, Dr. Ning Gan, Dr.

Joey Thompson, Dr. Jim Cochran, Dr. Peter Grudberg, Dr. Paul Rubinov, and Dr. Scott Snyder for their friendship, comfort, and stimulation. Jimmy proofread the entire thesis with many good suggestions. Professor Jianming Qian, who was my college classmate, has been a good example and reliable source of technical consultation.

The winters here in Chicago have been made like springs because of my many friends and mentors: Brenda Kirk, Dr. Franscois Ostiguy, and Dr. Roy Rubinstein of Fermilab, Dr. Bill Wu, Dr. I-Hung Li of AT&T...

I am indebted to many teachers I have had, especially my violin teacher when I was a little kid and my high school physics teacher. They taught me not only art and science, but also to see things with beauty, imagination, and harmony, to be creative, and to be self-disciplined. Although I am proud of the endless pursuit of perfection in both science and art, I also cherish the intuition, spontaneity, and sparks of creativity and originality in daily life. Nature is awesome and full of beauty. This was true when I observed the characteristics of phase transition of solid state materials through x-ray scattering, and when I first saw the Z peak from the DØ data. I have benefited from the mixture of science and art when doing physics research. I am fortunate to have been their students.

Last but not least, I would like to thank my parents, my grandparents, and my younger brother for their love and and my wife for her patience, support, and the wonderful gift she brought me: my son Nicky.

Chapter 1

Introduction

1.1 Standard Model

Fundamental particles[1] are by definition structureless and indivisible.

There are believed to be two types of fundamental particles that make up all matter: leptons and quarks.

There are four types of fundamental interactions in nature that govern the relations of the fundamental particles: the gravitational, electromagnetic, weak, and strong forces. Each interaction has its own set of conservation rules and distinct characteristics. They can all be described by group gauge theories. Many attempts to understand the interrelations of these fields have been made. The dream that all four fundamental forces will be found to be the manifestation of a simple grand unified theory is being pursued by many theorists.

In the late 1960's, Glashow, Weinberg, and Salam[2] proposed a theory unifying the electromagnetic and weak forces by using the concept of spontaneous symmetry breaking in the nonabalian gauge theory based on the symmetry group $SU(2)\times U(1)$. The group $SU(2)$ describes the symmetry of the doublets in the weak isospin space, which are the left handed lepton families (e_L,ν_e), (μ_L,ν_μ) and (τ_L,ν_τ). The $U(1)$ group describes the symmetry in the weak hypercharge space. A scalar field with a non-vanishing vaccum expectation value selects a preferred direction in weak isospin plus hypercharge space and thereby "spontaneously breaks" the $SU(2)\times U(1)$ symmetry. When the symmetry is broken at low energies, the electromagnetic force is transmitted by a massless photon and the weak force is transmitted by three spin 1, massive bosons W^+, W^- and Z.

Very exciting events in the history of high energy physics occurred in 1983 when the W and Z bosons were first discovered at the CERN $\overline{p}p$ collider[4]. Their measured masses and other properties were close to those predicted by the theory.

The success of the electroweak theory was particularly heartening because it took place in the context of quantum field theory, previously thought to be useful only for describing electromagnetic processes. A parallel development, also relying on quantum field theory, was the emergence of a theory of strong interactions, now known as quantum chromodynamics (QCD). This theory describes why quarks are different from leptons (quarks have a new kind of charge dubbed "color", while leptons are colorless), and gives quantitative predictions for their interactions with one another via the exchange of quanta known as "gluons".

QCD is based on the $SU(3)$ symmetry group. $SU(3)$ is the symmetry representation of three-component color spin 1/2 quark or spin 1 gluon fields, which is transmitted by eight massless gluons. The most important feature of QCD is, however, the asymptotic freedom, which means α_s, the coupling of the field, vanishes logarithmically at high Q^2 as shown clearly in the following expression [3]:

$$\alpha_s(Q^2) = \frac{4\pi}{(11 - \frac{2}{3}n_f)\log(Q^2/\Lambda^2_{QCD})} \tag{1.1}$$

where n_f is the number of quark contributions to the vacuum polarization with $m_f^2 \leq Q^2$. Λ_{QCD} is a theoretical normalization parameter and can be determined by using experimental α_s values. This parameter is typically of the order 100 to 200 MeV. When the momentum transfer Q^2 is larger than this, α_s becomes small. The hard QCD processes which are characterized by short distance and high momentum transfer can then be expressed perturbatively in terms of α_s. Therefore, the hard process calculations can be done perturbatively just as in quantum electrodynamics (QED).

This picture of particle physics based on the existence of quarks and leptons interating via exchanges of photons, gluons, W and Z bosons (the electroweak theory, combined with the QCD theory) has come to be known as the "Standard Model"[1]. It has withstood many experimental tests so far. The recent exciting discovery of the top quark by the DØ and CDF collaborations[10] at Fermilab provides further support of the theory.

The "Standard Model" is not yet perfect. In order to have spontaneous symmetry breaking, there should exist a Higgs particle associated with a scalar field, which has not yet been found. The origin of the masses of all fermions needs further study. In QCD, there are still many questions to be answered and non-perturbative QCD is still at the phenomenological level.

A detailed understanding of the properties of W and Z bosons will not only test the "Standard Model", but may also lead to new discoveries. Several e^+e^- collider experiments[5] already have been done at CERN and SLAC to study the properties of the Z boson. The mass, width and decay properties of the Z have been measured to very high precision[6][7]. Precise measurements of the W mass and width and its other properties are being pursued at Fermilab[8][9].

1.2 Proton-Antiproton Collisions

This thesis is based on the study of proton-antiproton collisions at $\sqrt{s} =$ 1.8 TeV using the Fermilab Tevatron collider.

Proton-antiproton collisions are complicated by the fact both the proton and the antiproton are composed of three valence quarks (proton: uud, antiproton: $\overline{\mathrm{u}}\overline{\mathrm{u}}\overline{\mathrm{d}}$), gluons and "sea" quarks which appear as virtual pairs. In most proton-antiproton collisions, the partons (quarks or gluons) interact with each other with low momentum transfers. Occasionally the partons interact with either a large momentum transfer or an annihilation into an energetic state. For example, the partons could form an energetic virtual intermediate state or a real heavy particle such as a W or Z boson. The final state quarks or gluons fragment into hadrons that are almost collinear with the final state parton direction. The cluster of particles from the fragmentation of a parton is called a jet. The final state W or Z bosons can decay into leptons or into quarks which then fragment. The partons not involved in the energetic interaction are called "spectators" and contribute low energy and forward particles to the event. These low energy and forward particles make up what is called the "underlying event" as shown in Fig. 1.1.

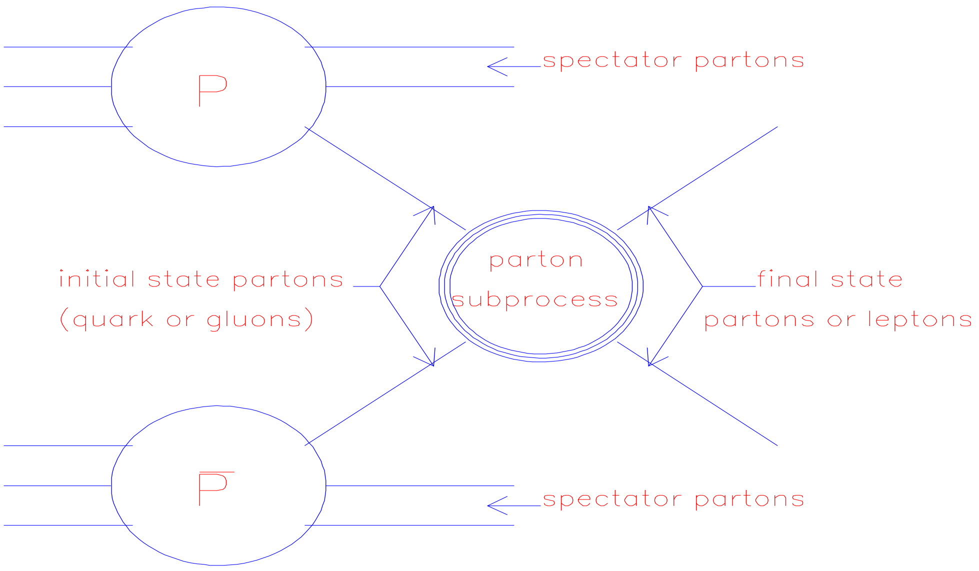

Figure 1.1: Schematics of the $\overline{p}p$ collision.

1.3 Z Production in $\overline{p}p$ Collision

The Z bosons produced in proton-antiproton collisions have both transverse and longitudinal momentum relative to the beam direction.

The transverse momentum is due to the initial parton transverse momenta and the production of gluons and quarks along with the gauge bosons. The contribution of the initial parton transverse momentum to Z p_T is on the order of 300 MeV/c [11]. Most often the Z is produced with a small p_T ($<$ 10 GeV/c). In these cases, one or both of the initial quarks undergoes initial state gluon radiation which gives the Z a small p_T. However, Z bosons can also be created with a large p_T ($>$ 30 GeV/c). In these cases, the Z recoils against an energetic quark or gluon. The Z can also recoil against a system of quarks and/or gluons (see Fig. 1.2).

The longitudinal momentum of Z is mostly due to the initial momentum imbalance of the two partons involved in the hard interaction. The initial longitudinal momentum of partons is described by the parton momentum distribution function (pdf) which represents the probability of finding a parton with momentum fraction $x = p/P_{\mathrm{proton}}$ between x and $x + dx$.

1.4 Z Production Model at a $\overline{p}p$ Collider

In the small p_T region ($p_T <$ 10 GeV/c), where soft initial state gluon radiation is expected to dominate, soft gluon resummation techniques[12][13]

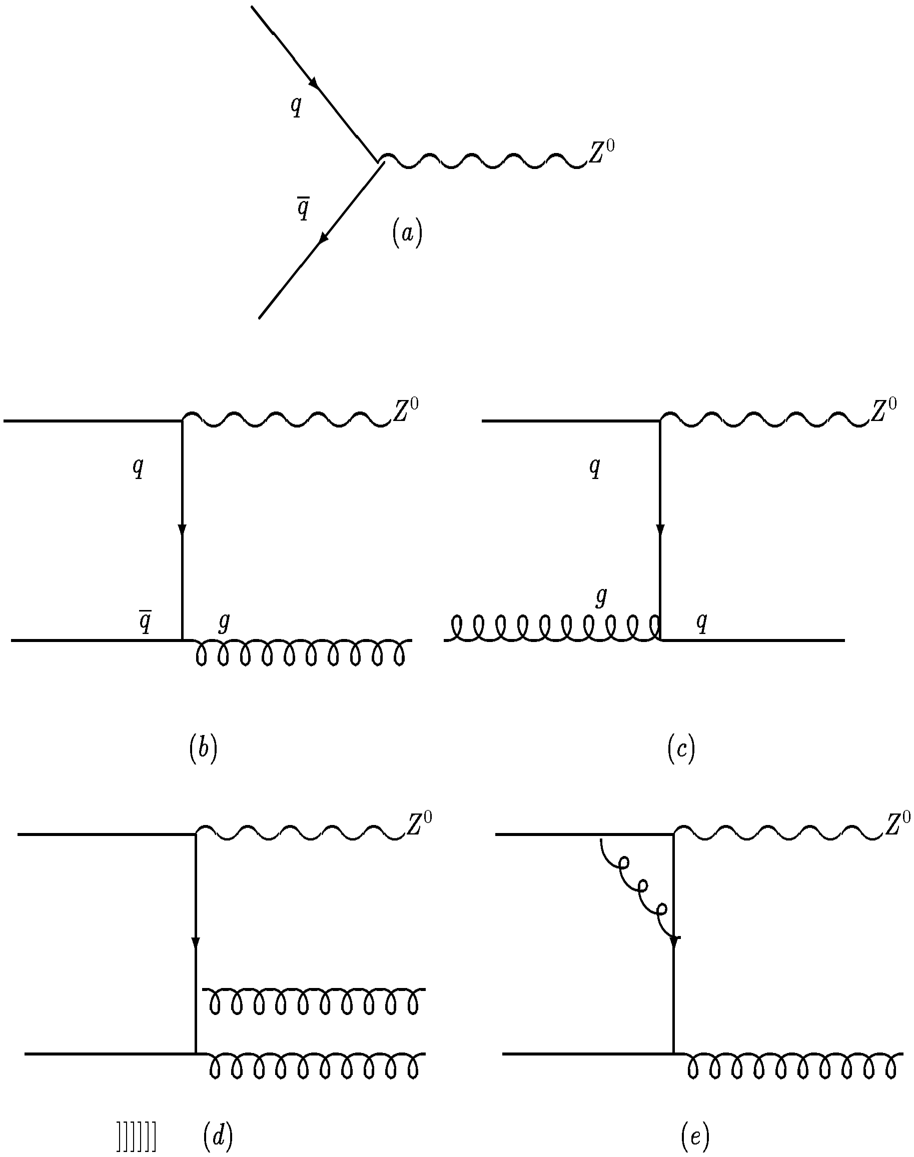

Figure 1.2: Feynman diagrams for Z production.

are used to calculate the differential production cross section. For the large p_T region ($p_T > 30$ GeV/c), the cross section is believed to be well described by perturbative QCD[13]. For the intermediate p_T, the resummation technique and perturbative QCD are matched to predict the cross section [13]. The resummation parameterization has been recently optimized to improve the description for the low p_T region [15].

The inclusive differential cross section as a function of p_T and rapidity y[1] for $p\overline{p} \longrightarrow Z + X$ production (X means anything produced along with the Z bosons) has the form [14]:

$$\frac{d\sigma(p\overline{p} \longrightarrow Z+X)}{dp_T dy} = \sum_{a,b} C_{a,b} \int_0^1 dx_a \int_0^1 dx_b f_a(x_a, Q^2) f_b(x_b, Q^2) \frac{d\hat{\sigma}}{dp_T dy} \left(x_a, x_b, ..., \alpha_s(Q^2)\right) \tag{1.2}$$

where Q^2 is the squared Z mass, $f_i(x_i, Q^2)$ is the parton distribution function which gives the probability that a parton of type i carries a fraction x_i of the parent hadron's momentum and

$$\frac{d\hat{\sigma}}{dp_T dy} \left(x_a, x_b, ..., \alpha_s(Q^2)\right) \tag{1.3}$$

is the relevant differential parton cross section. The sum is over all parton types a, b with color factor $C_{a,b}$.

At small p_T, the perturbative expansion in α_s is ruined because of the accompanying large logarithms ($\ln(\frac{Q^2}{p_T^2})$). However, it is possible to resum the

[1] $y = \ln[\frac{E+p_L^Z}{E-p_L^Z}]$ (E is total energy and p_L^Z is the longitudinal momentum of Z boson).

leading and next-to-leading $\ln(\frac{Q^2}{p_T^2})$ for each power of α_s to get an exponential factor. The procedure for summing these large logarithmic terms is generally referred to as "soft gluon resummation". The Collins-Soper-Sterman (CSS) resummation formalism[12] gives the form:

$$\begin{aligned} \frac{1}{p_T}\frac{d\hat{\sigma}}{dp_T dy} &= \frac{2\pi}{S}\sigma_o\delta(Q^2-M_Z^2)\left\{\frac{1}{(2\pi)^2}\int\int dq^2 d^2 b e^{i\vec{p_T}\cdot\vec{b}}\tilde{W}(b_*;q,x_a,x_b)\right. \\ &\left. \times e^{-S_{np}(b,q)} + Y(P_T;Q,x_a,x_b)\right\} \end{aligned} \tag{1.4}$$

where σ_o provides the process-dependent normalization, $b_* = \frac{b}{(1+b^2/b_{max}^2)^{1/2}}$, $b_{max} \sim 1/Q_0$ is characterized by a scale Q_0 at which perturbation theory is still valid and $\tilde{W}$ and Y are derived from perturbative calculations. The Y term contains the high p_T perturbative calculation. The resummation appears as an exponent, S_{np}, which has the form:

$$S_{np}(b,Q) = (g_1 + g_2 \ln(Q b_{max}/2))b^2 \tag{1.5}$$

where g_1 and g_2 are adjustable parameters.

Davies, Stirling and Webber [16] have performed a fit to ISR (R209) [17] and Fermilab (E288) [11] fixed target low p_T Drell-Yan data for the values of g_1 and g_2. There are three sets of numerical values that fit the data:

$$g_1 = 0.30 \ \text{GeV}^2, \ g_2 = 0.16 \ \text{GeV}^2 \ \text{(np1)} \tag{1.6}$$

$$g_1 = 0.15 \ \text{GeV}^2, \ g_2 = 0.41 \ \text{GeV}^2 \ \text{(np2)} \tag{1.7}$$

$$g_1 = 0.0 \ \text{GeV}^2, \ g_2 = 0.60 \ \text{GeV}^2 \ \text{(np3)} \tag{1.8}$$

The nonperturbative parameterization np2 is their preferred fit and was used by Arnold and Kauffman in their calculation. Arnold and Kauffman used all of the above fit parameters in their analysis of theoretical errors.

Recently, Ladinsky and Yuan improved the parameterization by including a dependence on x_a and x_b[15] as shown in the form:

$$S_{np}(b, Q, x_a, x_b) = g_1 b^2 + g_2 b^2 \ln(Q b_{max}/2) + g_1 g_3 b \ln(100 x_a x_b) \tag{1.9}$$

The inclusion of the x_a and x_b dependence is to account for changing average transverse momentum as a function of Q^2/s. In a recent fit to the R209 and E288 low p_T Drell-Yan data, the parameters g_1,g_2 and g_3 are determined and the values are [15]:

$$g_1^0 = 0.11^{+0.04}_{-0.03}\ \ \mathrm{GeV}^2,\ \ g_2^0 = 0.58^{+0.1}_{-0.2}\ \ \mathrm{GeV}^2,\ \ g_3^0 = -1.5^{+0.1}_{-0.1}\ \ \mathrm{GeV}^{-1} \tag{1.10}$$

The dominant theoretical error for the low p_T region is due to the uncertainty in these parameters.

1.5 Z Boson Decay

The Z boson has a very short lifetime ($< 10^{-24}$ sec, calculated from its width) and decays into quarks or leptons. About 70% of Z bosons decay into a quark and antiquark. Although this channel has the largest branching fraction, it is impossible to select a clean sample of Z events using this mode since the

the background from other QCD processes (QCD dijets, e.g.) overwhelms the signal. Z bosons can also decay into a pair of leptons and the branching fraction into each lepton pair is 3.366%[18]. The lepton channels can be used to select a clean sample of Z events. For the analysis presented in this thesis, we use the electron-positron[2] channel.

1.6 Schematic Diagram of the Analysis

As shown in Fig. 1.3, there are two streams of data for this analysis: Monte Carlo and real collider data. A fast Monte Carlo program[3] was developed to generate Z events and simulate the detector effects and selection cuts. The raw data are either compared with smeared [4] theory or unfolded to obtain the absolute differential cross section.

1.7 Thesis Organization

This thesis is organized as the following:

- Chapter 1 gives a brief introduction to the theoretical understanding of Z production.

---

[2]From now on "electron" will be used to describe both the electron and positron.

[3]See chapter 5 for details.

[4]To include detector and event selection effects.

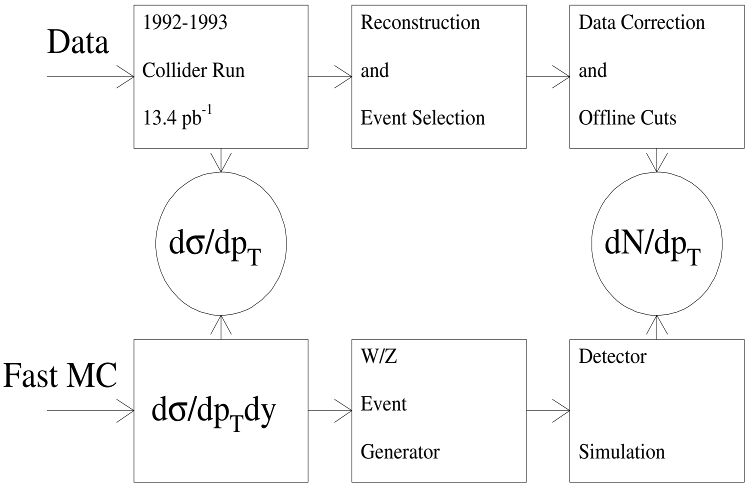

Figure 1.3: Block diagram of the analysis.

- Chapter 2 briefly discusses the modern technological wonder: the Fermilab Tevatron, a $\overline{p}p$ collider that made this thesis possible.

- In chapter 3, the DØ detector and its relevant sub-components for this analysis are outlined.

- In chapter 4, the data sample for this analysis and its quality are described.

- The fast Monte Carlo simulation, a critical part of this thesis, is described in chapter 5.

- In chapter 6, the measurement of the $\frac{dN(Z\rightarrow e^+e^-)}{dP_T}$ is discussed.

- In chapter 7, the measurement of the $\frac{d\sigma(p\overline{p} \longrightarrow Z+X)}{dP_T}$ is presented.

- The conclusion and discussion are given in Chapter 8.

Chapter 2

The Tevatron

Figure 2.1 shows the Tevatron complex.

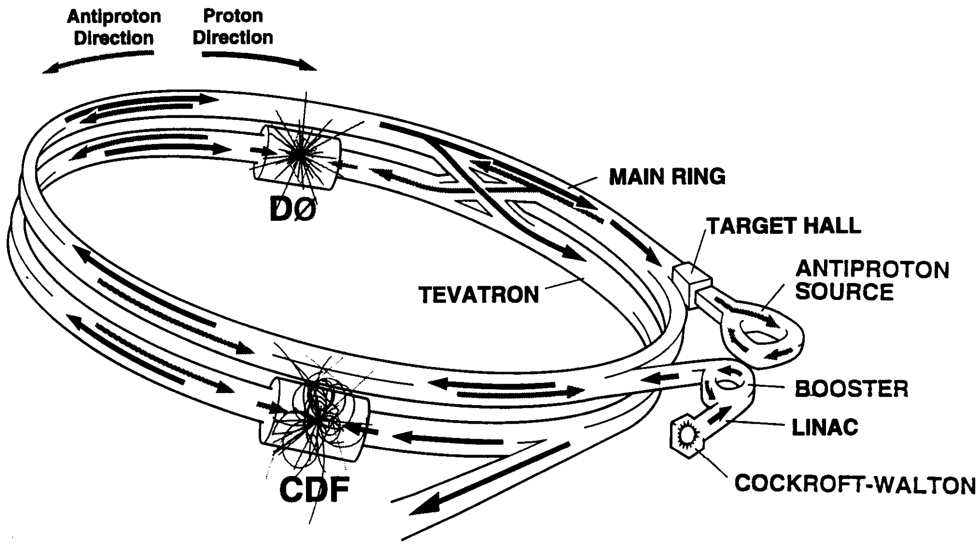

Figure 2.1: The Tevatron accelerator complex.

A Cockroft-Walton accelerator accelerates a beam of H^- ions to an energy of 750 keV. A Linac further accelerates the beam to an energy of 200 MeV. The beam is then shot through a carbon foil to strip off the electrons, leaving a beam of protons. A synchrotron (booster) then accelerates the beam to 8 GeV. The beam is then sent into the main ring and further accelerated to 120 GeV. Finally a superconducting synchrotron (the Tevatron) accelerates the beam to 900 GeV.

The antiprotons are produced by bombarding a copper and nickel target using the proton beam extracted from the main ring. The antiprotons are produced at a rate of 10^{-5}/incident proton. Because of the wide momentum spread, antiprotons are then focused and stored in a storage ring (accumulator), where the beams are compressed in phase space. When enough antiprotons have been accumulated, they are injected into the Main Ring and accelerated to 150 GeV and then to 900 GeV in the Tevatron moving in the direction opposite to that of the proton beam.

There are two collision regions, called BØ and DØ. The CDF detector located at BØ, and DØ detector, located at DØ are two collider detectors built to study the fragments of the collisions.

2.1 Luminosity

The instantaneous luminosity is an important parameter for the collider and it is defined as:

$$\mathcal{L} = \frac{R}{\sigma_{\rm tot}} \tag{2.1}$$

where R is the detector counting rate (events/sec) and $\sigma_{\rm tot}$ is the total $\overline{p}p$ production cross section (cm^2). The Luminosity has the unit of cm^{-2}s^{-1}.

The instantaneous luminosity is monitored according to equation 2.1 with the measured detector counting rate divided by the measured total $\overline{p}p$ production cross section.

Chapter 3

The DØ detector

The DØ Detector has excellent identification and measurement of electrons, jets, missing transverse energy ($\not\!\!E_T$), and muons.

The prime physics goals of the DØ Experiment include the study of the electroweak interaction, strong interaction, b quark production, search for the top quark, and phenomena beyond the standard model.

A cutaway isometric view of the detector is shown in Fig. 3.1.

The DØ detector[19][20] consists of central detectors, calorimeters and muon detectors. The relevant detectors for this analysis are briefly described in the following sections:

3.1 Central Detectors

Figure 3.2 shows the side view of the complete central tracking system.

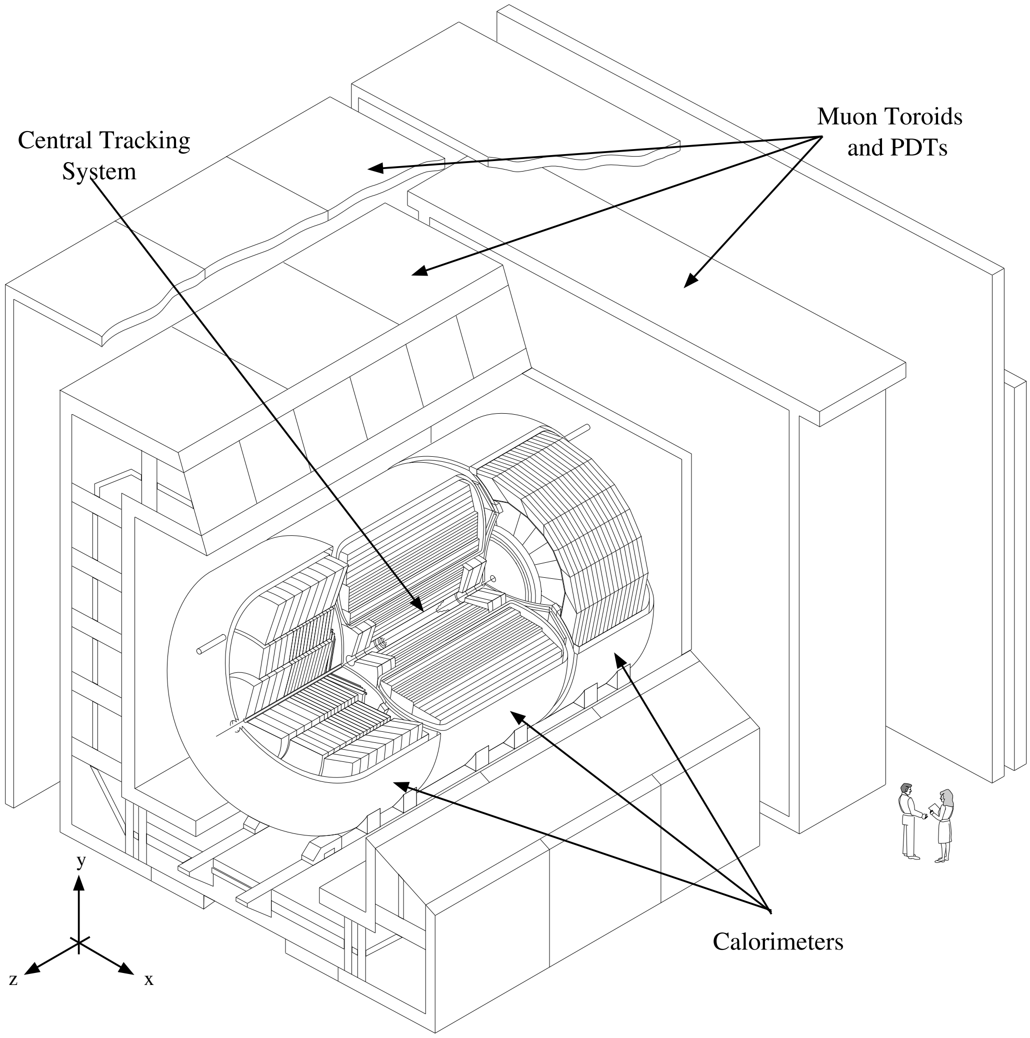

Figure 3.1: An isometric cutaway view of the DØ detector.

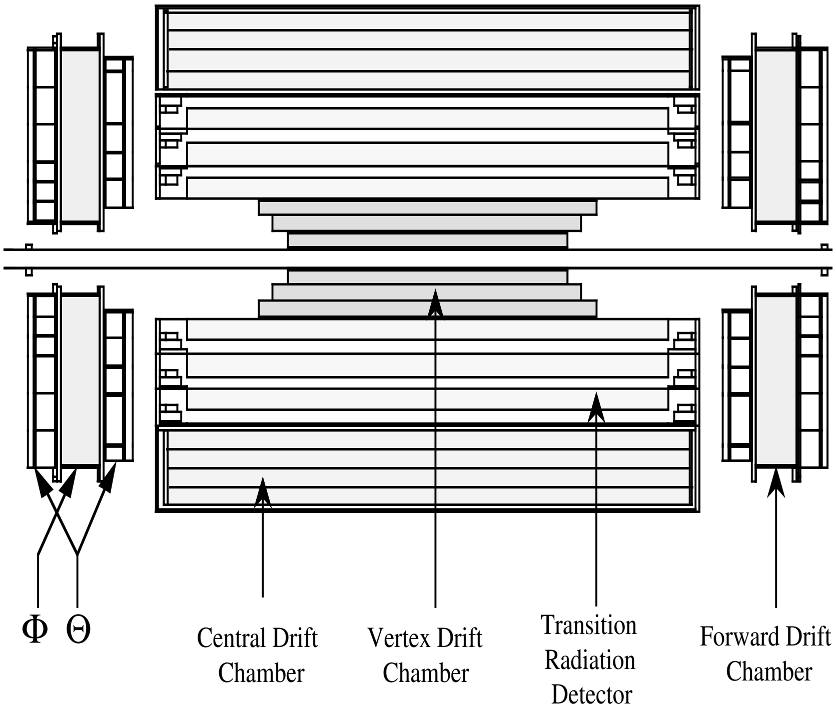

Figure 3.2: A side view of the DØ Central Tracking detectors.

3.1.1 Vertex (VTX) Chamber

The VTX chamber is the innermost tracking detector in DØ. It has an inner radius of 3.7 cm (just outside the beryllium beam pipe) and an outer active radius of r=16.2 cm. The typical resolution is 50 μm in the $r-\phi$ direction and 1 cm in the z direction[1].

---

[1]We adopt a right-handed coordinate system , in which the z-axis is along the proton direction and the y-axis is upward. The angles ϕ and θ are respectively the azimuthal and polar angles ($\theta = 0$ along the proton beam direction). The r-coordinate denotes the perpendicular distance from the beam axes. The pseudo-rapidity, $\eta \equiv -\ln(\tan(\theta/2))$, approximates the true rapidity $y = 1/2\ln((E+p_z)/(E-$

3.1.2 Transition Radiation Detector (TRD)

The TRD is between the VTX and the Central Drift Chamber and provides independent electron identification in addition to that given by the calorimeters and the tracking chambers.

The operation principle of the TRD is based on the phenomenon that when highly-relativistic particles ($\gamma \equiv \frac{E}{m} > 10^3$) traverse boundaries between media with different dielectric constants, transition radiation X-rays are produced. There are three separate units in the DØ TRD, each containing a radiator and an X-ray detection chamber. The effectiveness of electron ID by the TRD has been studied in detail in test beams[21]. An additional factor of about 50 for rejection of isolated pions is expected.

3.1.3 Central Drift Chamber (CDC)

The Central Drift Chamber is just outside the TRD and inside the Central Calorimeter. It reconstructs tracks of charged particles. The CDC is a cylindrical shell of length 184 cm and has an inner radius of 49.5 and an outer radius of 74.5 cm. There are four concentric rings of 32 azimuthal cells per ring. Each cell contains seven 30 μm gold-plated tungsten sense wires, read out at one end, and two delay lines embedded in the inner and outer shelves propagate signals induced from the nearest neighboring anode wire. Each delay line is read out at both ends.

The left-right ambiguity at the cell level is overcome by staggering the

---

p_z)), for finite angles in the limit that $(m/E) \to 0$.

adjacent wires within the cell in ϕ by $\pm$ 200 μm. Cells are also alternated in radius with one half cell offset to further aid in pattern recognition as shown in Fig. 3.3. The maximum drift distance is $\sim$ 7 cm.

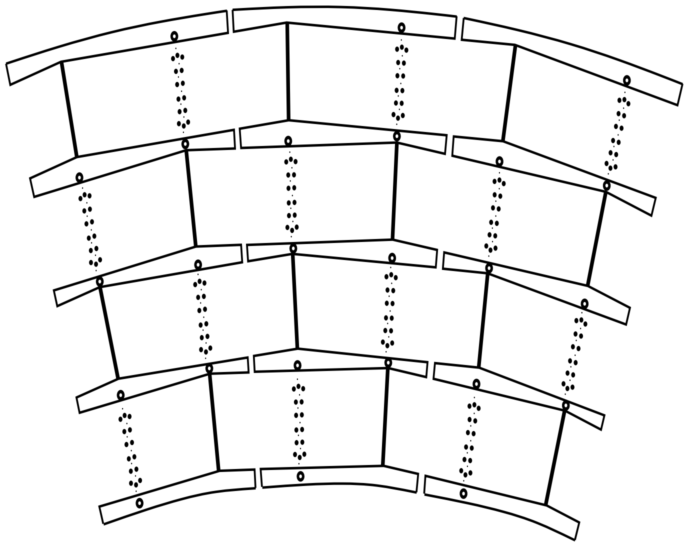

Figure 3.3: $r - \phi$ view of 3 of 32 central drift chamber modules. The circles are the cross sections of delay lines, the bold solid lines are the cell walls, and the dotted lines parallel to the walls indicate the locations of the sense wires.

The CDC is operated with Ar(92.5%)CH_4(4%)CO_2(3%) gas with 0.5% H_2O.

The inner sense wires are maintained at a voltage of 1.45 kV and the outer sense wires are held at 1.58 kV.

The $r - \phi$ resolution is about 150[19] μm and the z-resolution is $\sigma_z \simeq$

6 mm[22]. The efficiency for retaining single tracks, using the CDC and the VTX, is 98%.

3.1.4 Forward Drift Chambers (FDC)

The Forward Drift Chambers extend the coverage for charged particle tracking down to $\theta \approx 5^\circ$ with respect to both proton and antiproton beams. These chambers are located at either end of the concentric barrels of the VTX, TRD, and CDC and just before the end calorimeters.

There are three separate chambers in each FDC package: a Φ module with radial sense wires which measures the ϕ coordinate, sandwiched between two Θ modules which measure (approximately) the θ coordinate. Figure 3.4 is a diagram of one of these packages.

The FDC chambers are operated with the same gas as the CDC. The $r - \phi$ and θ position resolutions are about $200\,\mu$m [22].

3.1.5 Central Detector Electronics

The electronics for reading out signals from the Central Detectors are almost the same for all CD devices. The signals are processed in three stages: the preamplifiers mounted directly on the chambers themselves, the shapers located in the movable detector platform, and the flash ADC digitizers located in a Moving Counting House (MCH) about 20 meters away from the detector. Hardware zero suppression is employed to reduce the amount of data transmitted and to increase the data transfer speed.

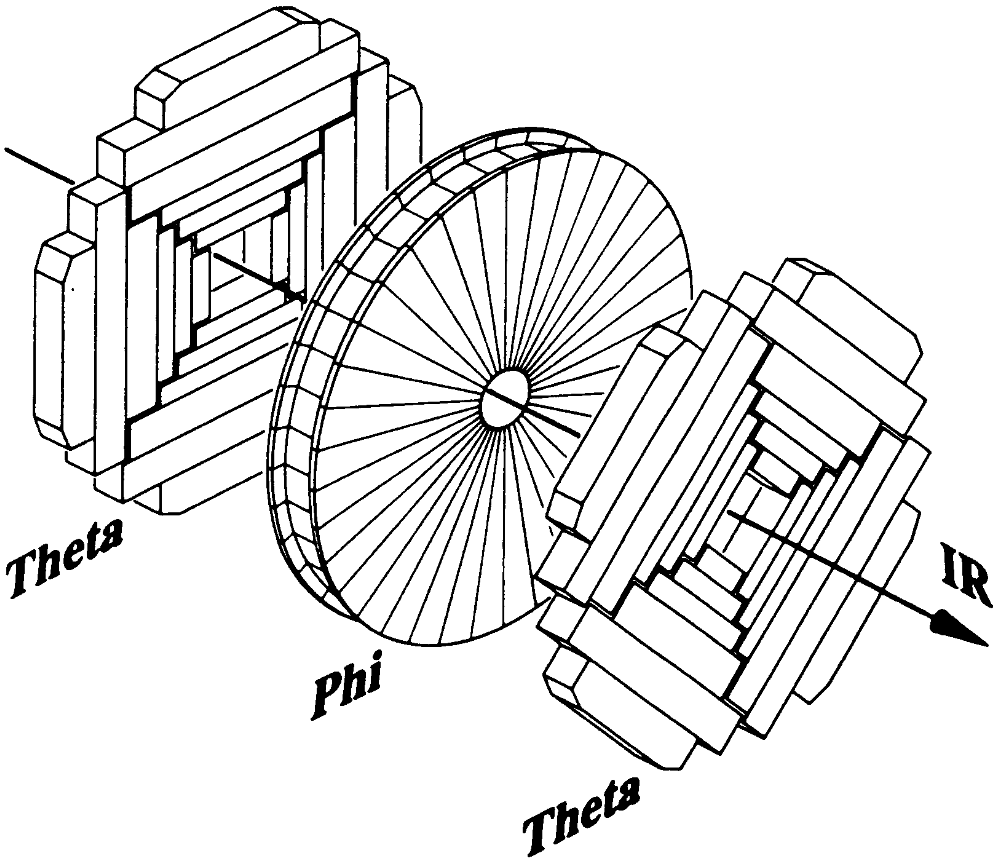

Figure 3.4: An exploded isometric view of one DØ Forward Drift Chamber. The arrow is pointing to the interaction region.

3.2 Calorimeters

The DØ calorimeter, shown in Fig 3.5, was designed to be nearly com-

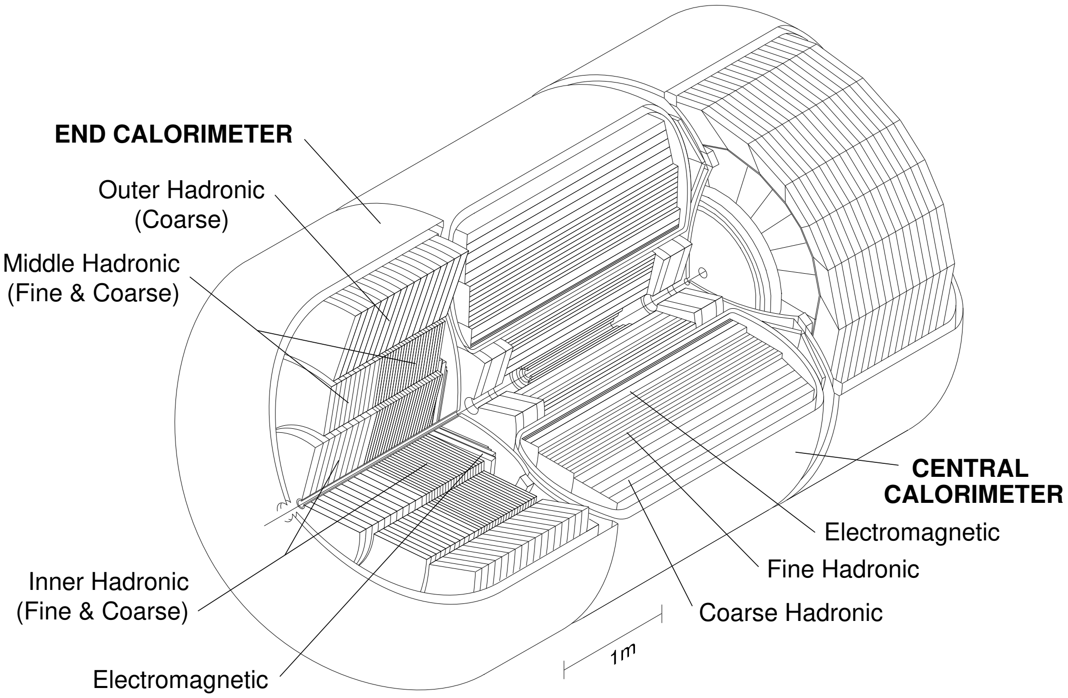

Figure 3.5: An isometric view of the DØ calorimeters

pensating, responding equally to hadrons and electrons (e/h=1.05) [23], This results in an excellent measurement of the energy of incident hadrons. It is achieved using liquid argon as the signal sampling material and uranium as the absorber. The calorimeter covers almost the entire 4π of solid angle.

There are 4 separate depth layers for the electromagnetic (EM) modules in central calorimeter (CC) and end calorimeter (EC). The first two layers (EM1 and EM2) are 2 radiation lengths (X_0) thick and are included to help measure the longitudinal shower development near the beginning of showers to discriminate photons and π^0s. The third layer (EM3) is at the maximum of the EM shower energy deposits with thickness of 6.8 radiation lengths (X_0) and the fourth (EM4) completes the EM coverage of approximately 20 X_0.

The fine hadronic modules (FH) are segmented into 3 or 4 layers and coarse hadronic modules (CH) are divided into one or three layers. The transverse sizes of towers in both EM and hadronic modules are $\Delta\eta = 0.1$ and $\Delta\phi = 2\pi/64 \approx 0.1$. EM3 is twice as finely segmented in both η and ϕ to better measure the EM shower centroids.

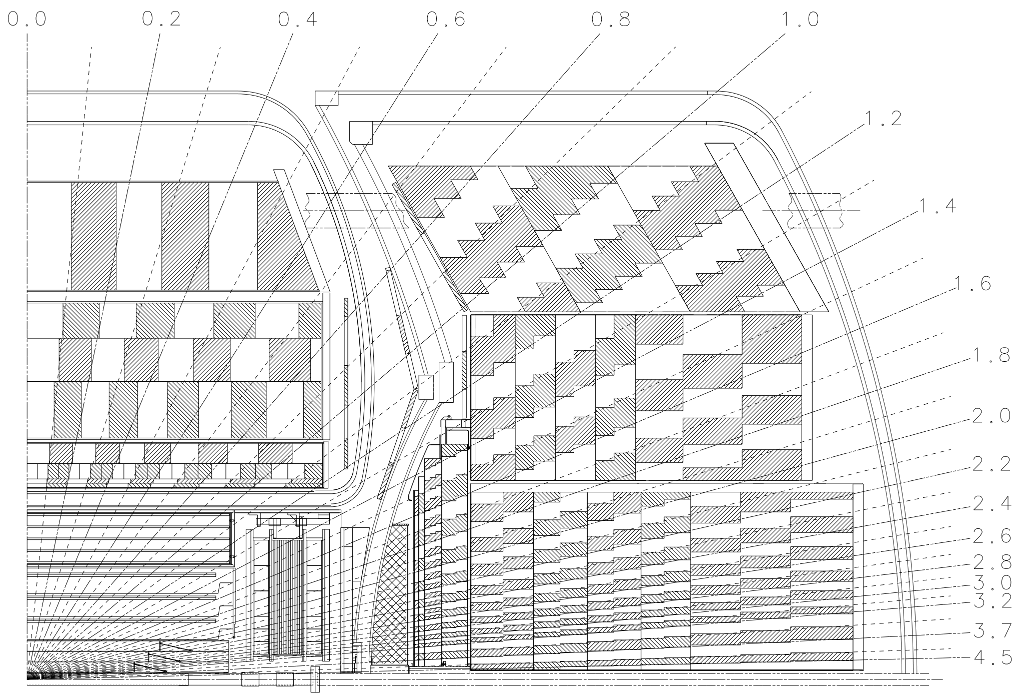

Figure 3.6: A side view of one quarter of the DØ calorimeters and central tracking detectors. The alternate shaded and unshaded areas show the calorimeter semi-projective towers and illustrate transverse and longitudinal segmentation. The numbers are the pseudorapidity η at each tower boundary. The Main Ring Bypass tube (the horizontal tube at the upper right) and the Intercryostat Detector (ICD) scintillator tiles, located on the inner face of the end cryostat are also shown.

A quadrant of the detector is shown in Fig. 3.6. The central region $|\eta| < 1.2$ is covered by Central Calorimeter (CC). The two end calorimeters, ECN and ECS, extend the η coverage to $|\eta| \simeq 4.0$.

3.2.1 Central Calorimeter

There are three concentric cylindrical shells in the CC. It consists of 32 EM modules in the inner ring, 16 fine hadronic (FH) modules in the surrounding ring, and 16 coarse hadronic (CH) modules in the outer ring. The EM, FH, and CH module boundaries are rotated so that no projective ray encounters more than one intermodule gap ("crack").

3.2.2 End Calorimeter

The two mirror-image end calorimeters (ECN and ECS) have four module types. There is one EM module and one inner hadronic (IH) module, shown schematically in Fig. 3.7. Outside the EM and IH, there are concentric rings of 16 middle and outer (MH and OH) hadronic modules.

3.2.3 Intercryostat Detectors (ICD) and Massless Gaps

In the region of $0.8 \leq |\eta| \leq 1.4$, a large amount of uninstrumented material is present. Two scintillation counter arrays called intercryostat detectors (ICD) that are mounted on the front surface of the ECs are used to correct for energy deposited in these uninstrumented regions. There are 384 scintillator

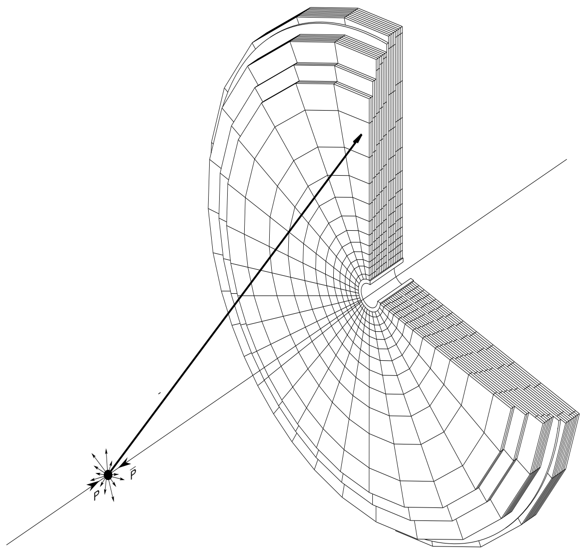

Figure 3.7: Schematics of the end EM calorimeter. The inner hadronic (IH) module is behind the EM module as the last layer away from the interaction region.

tiles of size $\Delta\eta = \Delta\phi = 0.1$ exactly matching the liquid argon calorimeter cells in each array. Separate single-cell structures called massless gaps are also installed in both CC and EC calorimeters.

3.2.4 Calorimeter Readout Electronics

Signals from the calorimeter modules are brought to four cryostat feedthrough ports in each cryostat. Short cables connect the output from the feedthrough boards to charge-sensitive hybrid preamplifiers. Output signals from the preamplifiers are transported on twisted pair cable some 30 m to the baseline subtractor (BLS) shaping and sampling hybrid circuits; input signals are integrated

(430 ns) and differentiated (33 μs). At the input to the BLS, a portion of the signal is extracted with $\simeq$ 100 ns rise time and added into trigger towers of $\Delta\eta = \Delta\phi = 0.2$ for use in event selection. The main signals are sampled just before a beam-crossing and 2.2 μs after; the difference is provided as a *dc* voltage proportional to the collected charge. Two storage capacitors for each channel allow double buffering at the analog level. Fast baseline restoration occurs in a few μs so as to minimize the effects of event pile-up. Depending on signal size, the BLS outputs can be amplified by 1 or by 8 so as to reduce the dynamic range requirements of the subsequent digitization.

The 24-channel 12-bit ADC circuits, together with the $\times 1$ or $\times 8$ amplifier allows an overall dynamic range of 2^{15}. Gain parameters are set so that about 3.75 MeV of deposited energy corresponds to one ADC count. Minimum ionizing particles deposit between 8 (EM1) and 90 (FH1) MeV in the layers of the calorimeters. Channels which have an absolute difference of signal and pedestal below an adjustable threshold can be suppressed from the readout buffer. Both single-channel random noise (electronics and uranium radioactivity) and multi-channel coherent noise have been measured in beam tests and in the DØ Hall. The single channel noise can be characterized as $2000 + 3100 \times \mathrm{C(nF)}$ electron charge. For many channels, the total random noise varies as $\sqrt{N}$, where N is the number of channels included; the total coherent noise varies typically as N.

A useful measure of coherent noise is the number of channels that can be summed before the coherent noise exceeds the random noise. In the DØ environment this number is typically >5000 channels.

Calibration of the various components of the electronics is accomplished by a precision pulser which injects charge through a large accurately known resistor at the front end of each preamplifier.

The system has been tested thoroughly and found to be linear, stable, and reliable. The failure rate of the signal channels in the detector is quite low.

3.2.5 Calorimeter Performance

The calorimeter modules were tested using pion, electron, and muon beams with energies between 2 and 150 GeV. The response to both electrons and pions is linear with beam energy to within 0.5% for energies between 10 and 150 GeV.

The relative resolution as a function of energy can be parameterized as

$$(\sigma_E/E)^2 = C^2 + S^2/E + N^2/E^2,$$

where the constants C, S, and N represent the calibration errors, sampling fluctuations and noise contributions respectively. We obtain from test beam [19] $C = 0.003 \pm 0.004$, $S = 0.157 \pm 0.005\sqrt{\mathrm{GeV}}$ for electrons in the ECEM and $C = 0.032 \pm 0.004$ and $S = 0.41 \pm 0.04\sqrt{\mathrm{GeV}}$ for pions in the ECMH. The noise contribution, $N = 0.4$ GeV, is dominantly due to uranium radioactivity, and is consistent with our previous discussion of random and coherent noise.

The calorimeter position resolution is important for identification of backgrounds to electrons from the near-overlap of photons and charged particles. For 100 GeV electrons, this resolution varies between 0.8 and 1.2 mm over the full range of impact positions; the position resolution varies approximately as $E^{-\frac{1}{2}}$.

3.3 Trigger and Data Acquisition

The DØ trigger and data acquisition systems are used to select and record interesting events. The trigger has three levels of increasingly sophisticated event characterization as shown in Fig. 3.8. The Level 0 scintillator-based trigger indicates the occurrence of an inelastic collision. At a luminosity of $\mathcal{L} = 5 \times 10^{30} \mathrm{cm}^{-2}\mathrm{s}^{-1}$, the Level 0 rate is about 150 kHz. Level 1 is a collection of hardware trigger elements arranged in a flexible software-driven architecture which allows easy modification. Many Level 1 triggers operate within the 3.5 μs time interval between beam crossings and thus contribute no dead time. The rate of successful Level 1 triggers is about 200 Hz. Candidates from Level 1 are passed on along the standard DØ data acquisition pathways to a farm of microprocessors which serve as event builders as well as the Level 2 trigger systems. Sophisticated algorithms reside in the Level 2 processors which reduce the rate to about 2 Hz before passing the events on to the Host computer for event monitoring and recording on permanent storage media. A schematic diagram of the the trigger and data acquisition system is shown in Fig. 3.9

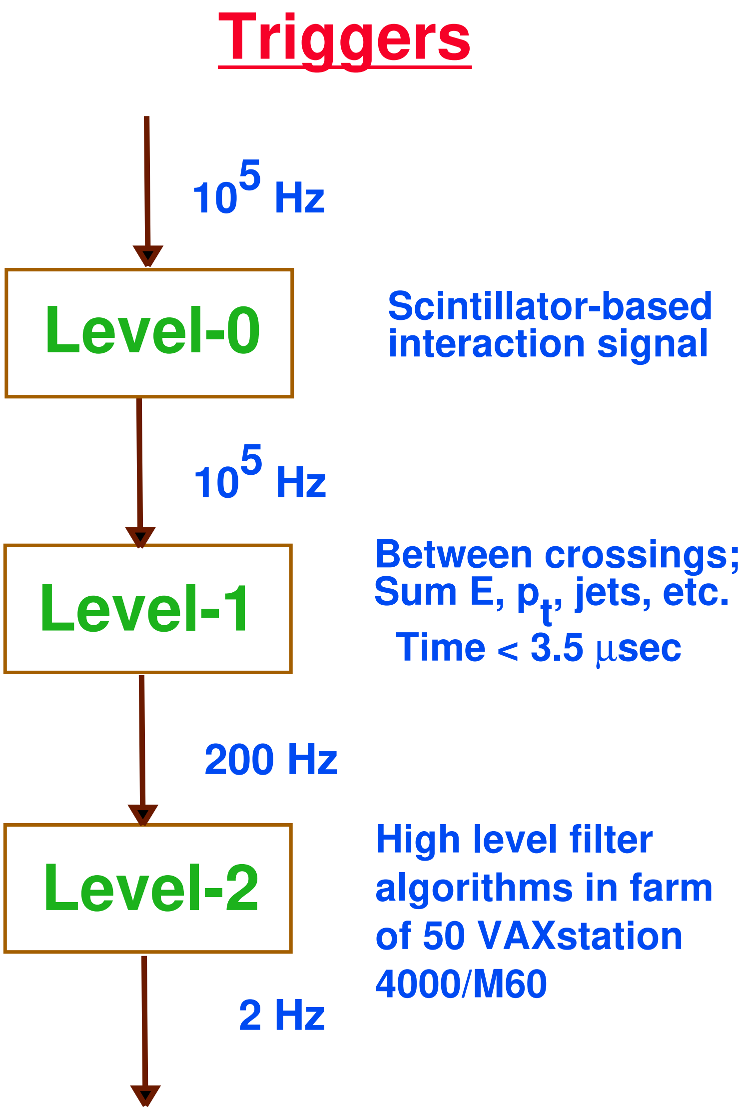

Figure 3.8: A schematic diagram of the DØ trigger system.

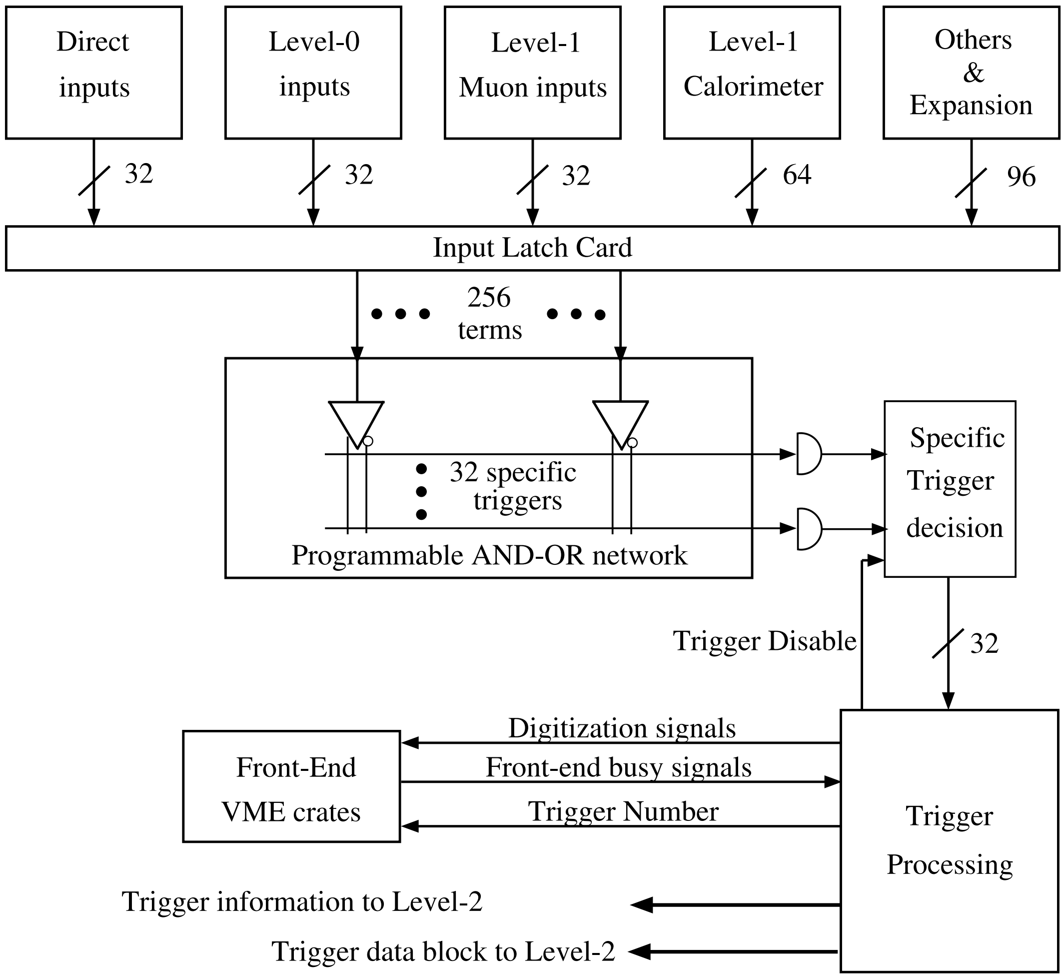

Figure 3.9: A schematic diagram of the DØ data acquisition and trigger system.

3.3.1 Level 0 Trigger

The Level 0 trigger registers the presence of inelastic collisions and serves as the luminosity monitor for the experiment. It uses two hodoscopes of scintillation counters mounted on the front surfaces of the end calorimeters. In addition to identifying inelastic collisions, the Level 0 trigger provides information on the z-coordinate of the primary collision vertex. The large spread of the Tevatron vertex distribution ($\sigma \simeq 30$ cm) has the potential for introducing substantial error in the transverse energy (E_T, see equation 3.1 for definition) used in the trigger. The z-coordinate is determined from the difference in arrival time for particles hitting the two Level 0 detectors. The Level 0 counters provide excellent time resolution (100-150 ps).

3.3.2 Level 1 Calorimeter Trigger

The system operates on the analog trigger pickoffs from the calorimeter BLS circuits, summed into $\Delta\eta = \Delta\phi = 0.2$ trigger towers out to $|\eta| = 4.0$. Separate trigger inputs are provided for the EM and hadronic sections (1280 of each) of the calorimeters. Each input signal voltage is analog-weighted by the sine of the trigger tower polar angle to give the transverse energy appropriate for an interaction vertex at $z = 0$.

The level 1 hardware trigger for this analysis requires 1 EM trigger tower ($\Delta\eta \times \Delta\phi = 0.2 \times 0.2$) above an E_T threshold of 10 or 12 GeV, where E_T is defined as:

$$E_T = E \times \sin\theta \tag{3.1}$$

E being the energy deposition of the tower and θ the polar angle of the tower with respect to the proton-beam direction (the origin is either assumed to be the center of the detector for the first one third of data or the event vertex measured by the Level 0 detector).

In the DØ trigger menu, this Level 1 trigger is initially called EM_1_MAX and later changed to EM_1_MED. The Level 1 trigger efficiencies are extracted from the data and discussed in section 5.2.1.

3.3.3 Level 2 Filter

The Level 2 filter works on the candidate list passed from the Level 1. For each Level 1 candidate trigger tower, Level 2 finds a readout tower ($\Delta\eta \times \Delta\phi = 0.1 \times 0.1$) with the highest energy and forms a 3×3 readout tower cluster around it. A cluster of energy in the calorimeter is identified as a "trigger electron" if (1) it is isolated and 90% of the energy is in the EM section of the calorimeter and (2) the shower shape is consistent with that expected for electrons[2]. For the Z events, we require that there is at least one trigger electron with a E_T above 20 GeV. In the DØ trigger menu, this Level 2 filter is called ELE_HIGH. The turn-on curves of the Level 2 filter are extracted from the data and discussed in section 5.2.1 also.

[2]See section 4.4 for definitions of isolation and shower shape.

The following list summarizes the Level 1 and Level 2 trigger conditions for the Z sample.

- Level 1 Trigger
  - EM_1_MAX or EM_1_MED
  - $E_T^{em} > 10$ *or* 12 GeV in a .2 x .2 (η x ϕ) tower (the threshold varied with running period; the bulk of the data used the 10 GeV threshold)
  - Coverage out to $|\eta| \leq 3.2$
- Level 2 Filter
  - ELE_HIGH
  - $E_T > 20$ GeV
  - Loose shower shape cuts
  - Isolation: $\frac{E^{total}(R_{iso}) - E^{em}(R_{core})}{E^{em}(R_{core})} < 0.15$ Depending on run period, with a roughly equal split, the isolation cone radii used were $R_{iso} =$ 0.4 or 0.6 in η, ϕ space; the core cone was always $R_{core} = 0.2$ in η, ϕ space.

All events that pass Level 1 and Level 2 requirements are recorded on tape for offline analysis.

Chapter 4

$Z \to e^+e^-$ Data Sample

4.1 Introduction

To reconstruct an event in terms of leptons and jets, we start with the data collected in terms of electronic charge-counter (ADC) or time-counter (TDC) units. These signals must go through a process of calibration and noise removal. Pattern recognition algorithms are then used to reconstruct the leptons and jets in each event. Because we are interested in events where a Z boson is produced and then subsequently decays into a pair of electrons, only a subset of the data is retained for further study. In this chapter, we describe the data collection, reconstruction, and reduction processes and discuss the quality of the sample.

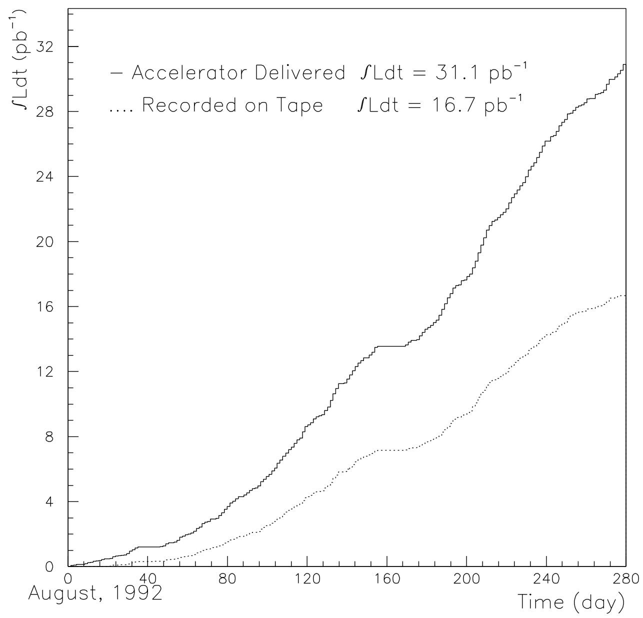

Figure 4.1: Run 1a Tevatron and DØ Performance.

4.2 The 1992-1993 Data Collection Period

4.2.1 The Integrated Luminosity

The data was collected during the 1992-1993 data collection period with 16.7 ± 2.0 pb^{-1} of data on tape. In the analysis, only a subset of data is used because the detector was being tuned during the first three months of data taking and it is hard to understand the data taken during that period.

The integrated luminosity delivered by the Tevatron Collider and recorded by the DØ detector is shown in Fig. 4.1 as a function of time.

There are two major inefficiencies in the DØ data collection, the dead time caused by the main ring veto and the DØ operating inefficiency.

Because of the noise caused by the accelerator main ring beam that passes through the DØ detector, proton-antiproton interactions that occur during the injection of beam into the main ring or when the beam in the main ring is near the DØ detector are vetoed. The operating inefficiency is mainly due to the detector maintenance downtime and time lapse between global data acquisition runs. The total loss due to the main ring vetoes is about 25% and the DØ operating efficiency is 80%. Overall, approximately 60% of the accelerator beam time is available for data taking.

4.3 Data Reconstruction

The data are recorded on 8mm tapes. The events are then reconstructed offline using a "farm" of computers. The event vertex and the tracks which point to the calorimeter energy clusters are found by the reconstruction program using the drift chamber hits. The reconstruction program then calculates the cluster energies, and uses a series of algorithms to identify electron, photon, muon, jet, and missing transverse energy ($\not\!\!E_T$). The full DØ reconstruction program DØRECO contains about 150,000 lines of code. Two output data files from each run with DØRECO are provided: the STA file contains the raw data plus the complete results of reconstruction. The STA events are used for reprocessing events of particular interest and in preparing displays. Each STA event contains approximately 600 Kbytes. The DST file contains a compressed version of the event with the most important information intended to serve the bulk of subsequent analysis needs. The DST contains summaries of tracks and calorimeter clusters as well as all parameters for electrons, photons, muons, jets, taus and missing transverse energy. The DST event size is approximately 20 Kbytes. Both versions utilize identical ZEBRA database structures.

4.3.1 Electron/Photon

The "nearest neighbor" algorithm is used for finding the electron or photon. An EM tower with the highest energy is used as a seed and neighboring cells over 50 MeV are added to it to form a cluster. For electron or photon candidates, the energy in the EM portion of the calorimeter must exceed 90% of the total energy, and the highest energy tower ($\Delta\eta \times \Delta\phi = 0.1 \times 0.1$) is required to contain more than 40% of the cluster energy. The E_T of the cluster must be greater than 1.5 GeV. Electron candidates are further required to have a track in the central or forward drift chambers which points from the event vertex to the calorimeter cluster center.

4.3.2 $\not{E}_T$

The $\not{E}_T$ is defined as:

$$\vec{\not{E}_T} = -\sum_i \vec{E_T^i} \tag{4.1}$$

where E_T^i is the E_T in cell i. The sum is over all the cells in the calorimeter.

4.3.3 Jets

DØRECO constructs jets according to several different algorithms. One is the nearest neighbor algorithm and the other one is known as the cone algorithm and is most commonly used for three different cone sizes ($\Delta R =$

$\sqrt{\Delta\eta^2 + \Delta\phi^2} = 0.3,\ 0.5,$ and 0.7). The cone algorithm works as follows: It starts with the highest E_T calorimeter tower. A precluster is formed from all contiguous towers within $|\Delta\eta| < 0.3$ and $|\Delta\phi| < 0.3$ with $E_T > 1$ GeV. For each precluster, the "E_T weighted" centroid defines the axis of the corresponding jet candidate. The energy within cones of $\Delta R = 0.3,\ 0.5,$ or 0.7 around the axis is summed and a new "E_T weighted" center is obtained. Starting with this new center the process is repeated several times until the center is stable. Once the jet is formed DØRECO requires that the E_T be greater than 8 GeV if the object is to be defined as a jet. As with all reconstructed objects, the definition of a jet is relative; a 0.7 cone jet which just passes the E_T threshold will probably not survive as a 0.3 cone jet.

4.4 $Z \rightarrow e^+e^-$ Event Selection

The sample selected with the single electron trigger contains not only Z bosons, but also W bosons, as well as background events. we must apply additional cuts to obtain a sample of clean Z events.

4.4.1 Electron Identification(ID)

Because the large fluctuations in the fragmentation process could make a jet appear like an electron, the electron candidates reconstructed by DØRECO may actually be jets. This is the case when the jet mostly consists of π^0's and its decay photons convert into pairs of electrons with very small angular spread. Further cuts on electron quality parameters are needed to identify good electrons. The cuts are described below:

Cluster EM Fraction:

The EM fraction cut simply requires that most of the cluster energy be contained within the EM calorimeter. The electromagnetic calorimeter being 21 X_0 thick makes this a highly efficient cut. This cut is already applied at the data reconstruction stage (larger than 90% EM fraction).

Cluster Shower Shape:

The cluster shower shape is required to be consistent with that of an electron. This requirement is imposed as a cut on the cluster χ^2 determined from the energy distribution within the cluster.

The transverse and longitudinal energy depositions of both test beam and Monte Carlo electrons are measured and a covariance matrix (M_{ij}) is constructed from these measurements.

$$M_{ij}(\eta, E) = \frac{1}{N} \sum_{n=1}^{N} (x_i^n - \overline{x_i})(x_j^n - \overline{x_j}) \tag{4.2}$$

where N is the number of electrons, x_i^n the energy deposited in each calorimeter cell for electron n and $\overline{x_i}$ is the average energy deposited in the calorimeter cell i. The covariance matrix contains both energy and η dependencies. For each event, the measured energy depositions for an electron candidate are compared with that expected from the reference sample and a χ^2 quantity is constructed:

$$\chi^2 = \sum_{i,j} (x_i^k - \overline{x_i}) H_{ij} (x_j^k - \overline{x_j}) \tag{4.3}$$

where $H = M^{-1}$ and k denotes the electron candidate. The electron candidates are rejected if their χ^2's are large. This requirement on the cluster shower shape provides high rejection of pions, while retaining good efficiency for electrons[24] [25].

Cluster Isolation:

The cluster is required to be isolated from other sources of energy in the events. The isolation variable (Iso) is defined as a ratio:

$$\text{Iso} = \frac{E(0.4) - EM(0.2)}{EM(0.2)} \tag{4.4}$$

where total energy in a cone defined by a radius $\sqrt{\Delta\eta^2 + \Delta\phi^2} < 0.4$ centered on the electron is denoted by $E(0.4)$, while $EM(0.2)$ is the electromagnetic energy in a cone of radius 0.2. The cut is effectively requiring the electron energy to be deposited within a cone of 0.2 and to be isolated within a cone of 0.4 from other particles in the event.

Cluster Track Matching Significance:

The calorimeter cluster is required to be well matched to a reconstructed central or forward track. The cluster centroid is determined from the calorimeter energy deposition in the EM3 layer and the track parameters fitted from the hits in the drift chambers are extrapolated to the shower position. The track matching significance (S) is defined as:

$$S = \sqrt{(\frac{\Delta\phi}{\sigma_\phi})^2 + (\frac{\Delta z}{\sigma_z})^2} \tag{4.5}$$

for the central calorimeter and

$$S = \sqrt{(\frac{\Delta\phi}{\sigma_\phi})^2 + (\frac{\Delta\rho}{\sigma_\rho})^2} \tag{4.6}$$

for the end calorimeter, where ρ z,and ϕ are cylindrical coordinates and $\Delta\phi$, Δz and $\Delta\rho$ are the differences between the measured centroid and projected track positions at the calorimeter EM layer 3. The σ's are the resolutions in z,ϕ, and ρ.

4.4.2 Electron Fiducial Region

Because the electron identification and energy resolution rely heavily on calorimeter information, we restrict electrons to regions of the calorimeter away from the edges between modules. This is the region where electron detection efficiency is uniform and energy measurement is reliable. There is no EM coverage in the intercryostat region, so electrons that went into this area are lost.

There are phi "cracks" between the 32 EM calorimeter modules in the central calorimeter. Since the response to electron energy is not uniform and the electron ID efficiency are not well understood in these "crack" regions, it is necessary to either cut out the electrons going into these regions or correct the calorimeter response when we need to include those electrons. The calorimeter energy response has been studied in the test beam run for calorimeter calibration. Fig. 4.2 [26] shows that about 0.005 radian in phi away from the module edge, the calorimeter energy response to a 100 GeV electron beam is almost uniform and energy loss due to the leakage through the "crack" is very small. We choose to cut out electrons within 0.01 radian in phi from the center of the "crack" to guarantee 100% and uniform energy response.

Since there are a lot of energy depositions from the underlying events in

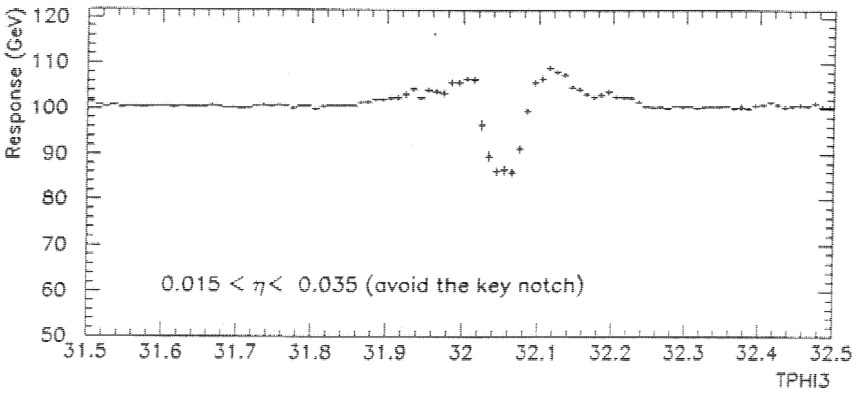

Figure 4.2: Mean response to 100 GeV electrons vs TPHI3 in the vicinity of the module crack, where TPHI3 $= \Phi \times 64./2\pi$ and the crack is at $\Phi = \pi$.

the end calorimeter regions around the beam pipe, the electron ID efficiency is hard to understand, so we cut out these regions too.

In the unit of detector η[1], the electron fiducial regions are defined as $|\eta| < 1.1$ (CC), where complete four EM layer coverage is available and $1.5 < |\eta| < 2.5$ (EC).

4.4.3 Electron Energy Correction

The absolute energy scale of the DØ calorimeter is provided initially by test beam energy calibrations. There were two test runs to study and calibrate the calorimeter modules. In the second test, a quadrant of the calorimeter (central and end calorimeters) was calibrated using beams of electrons and

[1]See section 3.1.1 for the η definition. The difference is that the detector η is always calculated from the detector center.

pions. The EM energy scale is set by using the measured relationship of the calorimeter pulse height (in ADC counts) and the beam momentum. The calorimeter electronics in the test beam and at DØ differ somewhat, primarily in the lengths of cables used and the times at which the analog signals are sampled. They are compared by using a stable pulse generator to inject equal charges in both systems. Various other differences between the test beam and the DØ detector, such as the high voltage (HV) applied across the liquid argon gap and the measured purity of the liquid argon, are also taken into account. Using this initial energy scale calibration, the measured Z mass was found to be lower than that measured by the LEP experiments. This observation triggered an extensive re-examination of the EM energy scale. The resulting Z mass is still a few percent lower than the Z mass measured by the LEP experiments.

In this analysis, the absolute energy scale of the EM calorimeters is set by scaling the invariant mass peak to the LEP value for the Z mass[5] before the kinematic cuts. Table 4.1 shows the electron energy scale correction factors at different regions:

	CC	ECN	ECS
Correction Factor	1.072 ± 0.002	1.025 ± 0.005	1.012 ± 0.007

Table 4.1: Electron energy scale correction factors.

4.4.4 Selection of $Z \to e^+e^-$ Events

For the $Z \to e^+e^-$ data sample, we require:

- Events passing single electron trigger with a E_T threshold of 20 GeV.
- At least one vertex found.
- Both electron candidates in fiducial region.
- Both electron candidates with $E_T > 25$ GeV after the EM energy scale correction discussed in the last section.
- Di-electron invariant mass between 75 GeV/c^2 and 105 GeV/c^2.
- Both electron candidates passing electron ID cuts.

  There are three sets of electron ID cuts (standard, tight, and loose) for this analysis as defined in Table 4.2, Table 4.3, and Table 4.4.

Cut name \ Cut region	CC	EC
EM fraction	0.90	0.90
Isolation	0.15	0.15
Track Matching Significance	10.	10.
χ^2	100	200

Table 4.2: Standard electron ID cuts.

We either require (a): both electrons to pass the standard electron ID cuts or (b): either one of the electrons to pass the tight cuts and the second electron to pass the loose cuts. Since only one electron is required to have a track in the (b) sample, this effectively increases the selection

Cut name \ Cut region	CC	EC
EM fraction	0.95	0.95
Isolation	0.10	0.10
Track Matching Significance	5.	10.
χ^2	100	100

Table 4.3: Tight electron ID cuts.

Cut name \ Cut region	CC	EC
EM fraction	0.95	0.95
Isolation	0.10	0.10
Track Matching Significance	NA	NA
χ^2	100	100

Table 4.4: Loose electron ID cuts. NA means the cut is not applied.

efficiency so that we can have more Z events. Because the electron tracking angles (θ in EC and ϕ in CC specifically[2]) are better measured than the calorimeter angles, it is desirable to use these angles in calculating Z p_T. So in this analysis, we first use the (a) sample to do the shape measurement and constrain the production models then use the (b) sample to do the absolute differential cross section measurement. There are total of 625 and 758 events in (a) and (b) sample respectively.

Figure 4.3 shows the di-electron invariant mass distribution for the (a) sample, where a clear Z mass peak is seen. The mass peak is fitted with a Breit-Wigner convoluted with a Gaussian resolution plus a linear background

[2]See section 5.2.1 for details.

shape. The observed p_T distribution of these Z candidates events is shown in Fig. 4.4. Both plots are after the EM energy scale correction.

4.5 Electron Selection Efficiencies

4.5.1 Electron ID and Tracking Efficiencies

The electron ID and tracking efficiencies are measured from a sample of electrons selected from the Z data sample described below.

The selection of the sample is similar to that described in section 4.4.4 except we only require the first electron to pass trigger and electron ID cuts and leave the second electron untouched, guaranteeing that the second electron is unbiased by any trigger and offline requirements. We then apply each set of electron ID cuts discussed in section 4.4.4 on the second electron to study the efficiencies. The electron ID efficiencies for each set of cuts are shown in Table 4.5.

The tracking efficiency is a measure of how well the central detector finds the track associated with a real electron and it is measured as the ratio of the number of Z electrons found with a track to the number of Z electrons found with or without a track. The tracking efficiencies are shown in Table 4.6.

The combined electron-ID and tracking efficiencies for the standard and tight cuts are calculated as the products of electron-ID efficiency and tracking

	CC	EC
$\varepsilon^{eid}_{standard}$	$91.0 \pm 1.5 \pm 0.9\%$	$87.7 \pm 2.4 \pm 1.4\%$
$\varepsilon^{eid}_{tight}$	$85.1 \pm 1.6 \pm 0.9\%$	$83.9 \pm 2.6 \pm 0.9\%$
$\varepsilon^{eid}_{loose}$	$88.5 \pm 1.6 \pm 0.3\%$	$89.6 \pm 2.1 \pm 0.6\%$

Table 4.5: Electron ID efficiencies $\pm$ statistical errors $\pm$ systematic errors for the standard, tight, and loose electron ID cuts. In the study, the standard and tight cuts are applied to the electron candidates with tracks and the loose cut is applied to the electron candidates with and without tracks.

	CC	EC
$\varepsilon^{tracking}$	$87.7 \pm 1.3 \pm 0.3\%$	$83.6 \pm 2.1 \pm 0.4\%$

Table 4.6: Electron tracking efficiency $\pm$ statistical errors $\pm$ systematic errors.

efficiency:

$$\varepsilon = \varepsilon^{eid} \cdot \varepsilon^{tracking} \tag{4.7}$$

and the results are listed in Table 4.7 along with the electron ID efficiency for the loose cut $\varepsilon_{loose} = \varepsilon^{eid}_{loose}$.

We plot the efficiencies of the electron ID cuts as a function of Z p_T as shown in Fig. 4.5[27]. There is no significant dependence on Z p_T for the electron ID cut efficiencies.

	CC	EC
$\varepsilon_{standard}$	$79.8 \pm 2.0\%$	$73.3 \pm 3.0\%$
ε_{tight}	$74.6 \pm 2.0\%$	$70.1 \pm 2.9\%$
ε_{loose}	$88.5 \pm 2.1\%$	$89.6 \pm 3.4\%$

Table 4.7: Combined electron ID and tracking efficiencies of the standard, tight, and loose electron ID cuts.

4.5.2 Trigger Efficiency and Bias Study

Since the level 2 electron filter has both shape and isolation cuts, we need to study the single electron trigger efficiency and its dependence on Z p_T.

The method to measure the trigger efficiency (Level 1 and Level 2 combined) and its dependence on Z p_T is simple: for events obtained with a single electron trigger after passing all the cuts discussed in section 4.4.4, if one electron is triggered, check if the other electron may pass the trigger also[3]; the passing rate of this electron is effectively the trigger efficiency.

Figure 4.6 shows that the isolation parameters of the two Z electrons as defined in section 4.4.1 are not correlated and the trigger efficiency as a function of Z p_T. The trigger efficiency has little dependence on p_T. Because each Z event has two chances to pass a single electron trigger, the trigger bias is negligible.

[3]We actually check if the Z event can pass a double electron trigger as well, where the double electron trigger requires both electrons to pass the single electron trigger.

4.6 Background Estimation

The possible background sources for the Z sample are:

- QCD multijets events with two jets faking electrons and passing the cuts.
- Drell-Yan continuum [14].
- $Z \to \tau\tau \to ee$.

The area under the linear line within the mass window in Fig. 4.3 gives the total number of QCD+Drell-Yan background events. From theoretical calculation [28] and Monte Carlo simulation[29] with PYTHIA[30], we obtain the percentage of the Drell-Yan background under the Z peak. The $Z \to \tau\tau \to ee$ background is studied using Monte Carlo data. 2500 Monte Carlo $Z \to \tau\tau \to ee$ events with full detector simulation are selected with the same selection cuts as in the Z data sample and their di-electron invariant mass peak is shown in Fig. 4.7. No event falls in the Z mass window and this background is mainly suppressed by the kinematics cuts. Taking the $Z \to \tau\tau \to ee$ branching faction (0.56%) into account, this Monte Carlo sample is equivalent to a data sample with ~ 0.45 millions $Z \to ee$ events in it. Therefore this background rate is $< 2.2 \cdot 10^{-6}$/per Z event and negligible in the data sample.

Table 4.8 summarizes the background estimation. The background is subtracted from the signal according to the percentage of the background in the total number of events.

	QCD	Drell-Yan	$Z \rightarrow \tau\tau \rightarrow ee$
Background (%)	3.5	1.3	0.0

Table 4.8: Background estimation of the Z data sample after standard electron ID cuts.

4.7 Background p_T Distribution

In order to study the background p_T distribution, the product of the isolation parameters defined in section 4.4.1 of the two electrons are plotted as a function of the invariant mass as shown in Fig. 4.8. It is clear that the background events are more uniformly distributed, whereas the signal events are highly clustered under the line of Iso1$*$Iso2$=$ 0.006.

Figure 4.9 shows the p_T distributions for the background events in different regions. There is a clear dependence of the p_T distribution on the invariant mass. We presume that the background events in B region give the best estimate of the p_T distribution of the background events in the S (signal) region. The similarity between the background and signal p_T distributions is due to the similarity in the production mechanisms: the p_T is due to the initial state parton radiations within the same mass window.

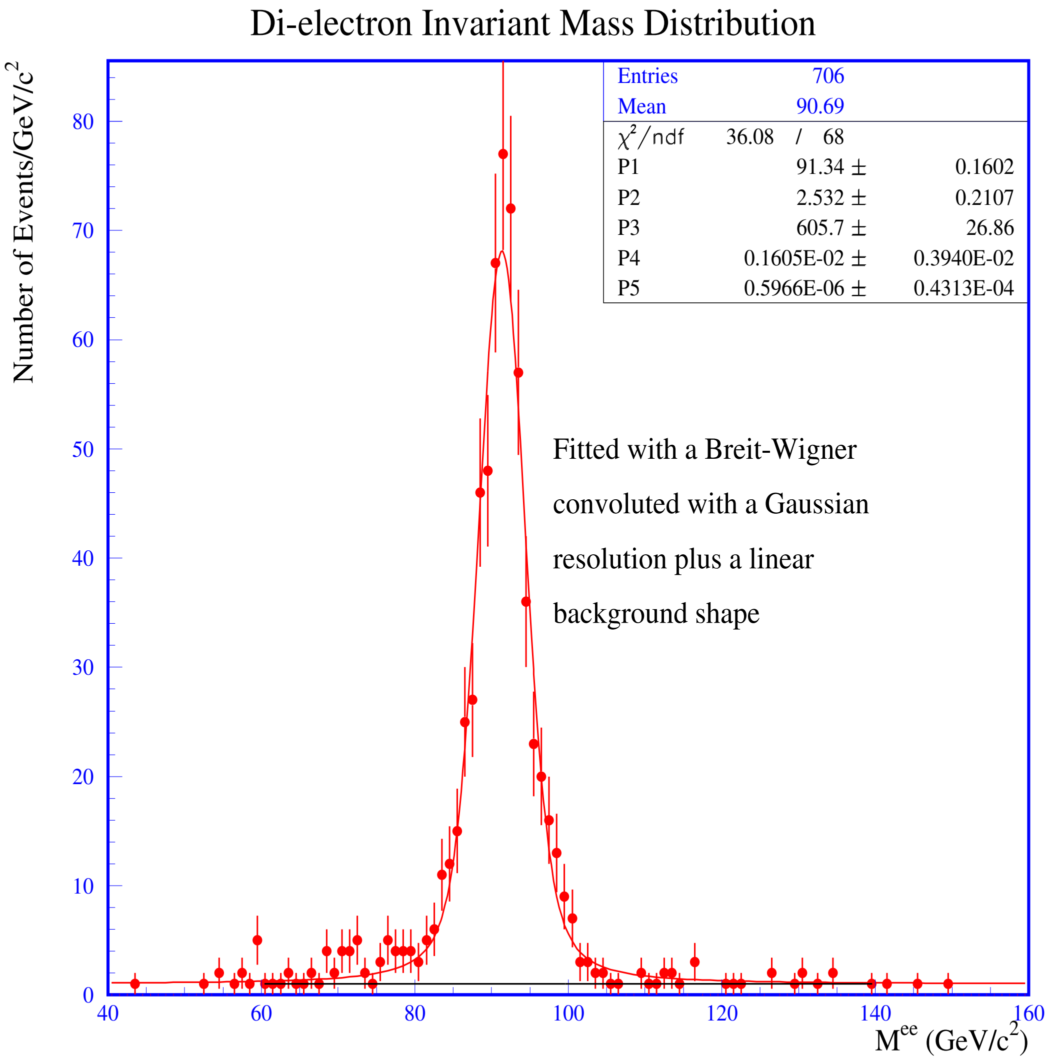

Figure 4.3: The di-electron invariant mass distribution after standard electron ID cuts. It is fitted with a Breit-Wigner convoluted with a Gaussian resolution plus a linear background shape. The line is described as $\mathrm{P3} \cdot (\mathrm{P4} + \mathrm{P5} \cdot \mathrm{M}^{ee})$ and the Breit-Wigner is described as $\frac{m^2}{(m^2 - \mathrm{P1}^2)^2 + \frac{m^4 \mathrm{P2}^2}{\mathrm{P1}^2}}$ with P1 as the fitted Z mass and P2 as the fitted Z width.

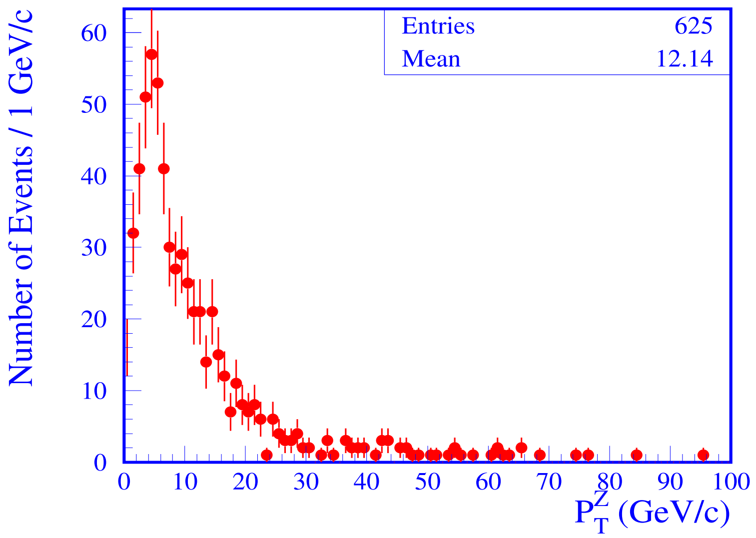

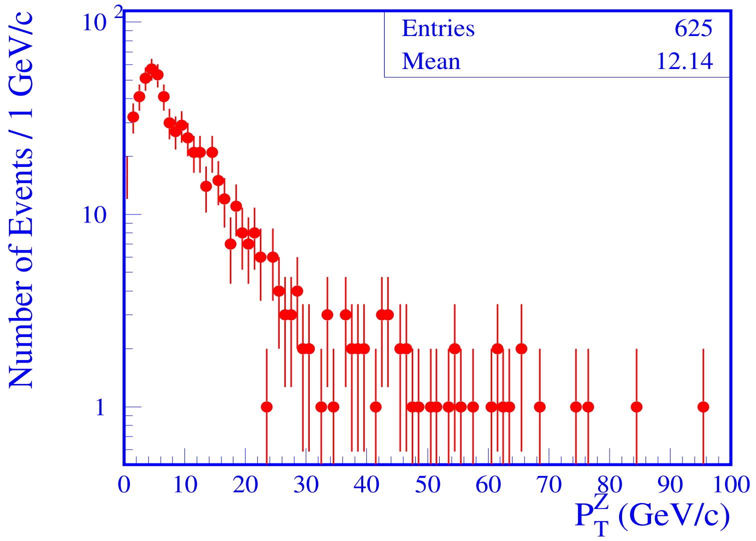

Figure 4.4: The raw p_T distribution after standard electron ID cuts. The upper plot has a linear scale and the bottom plot has a log scale for the vertical axis.

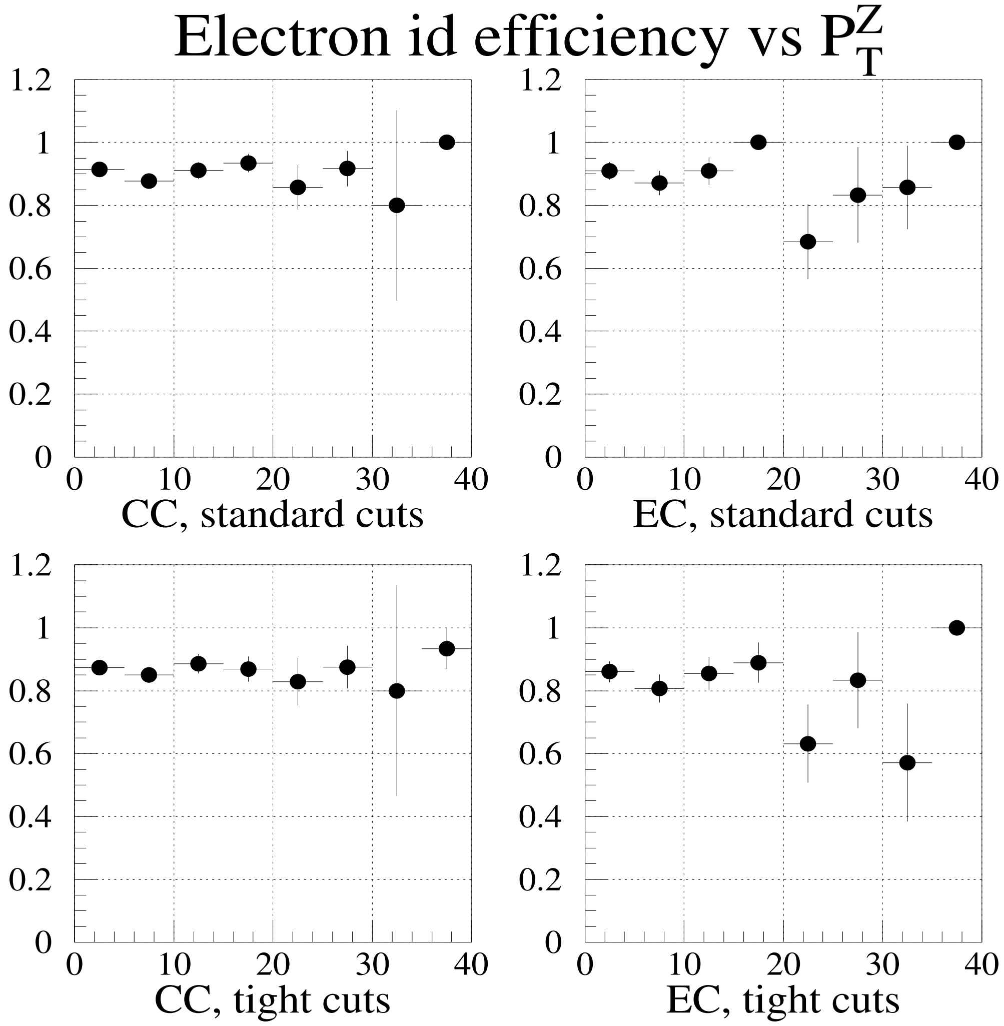

Figure 4.5: Electron ID efficiencies vs. Z p_T (GeV/c) for different electron ID cuts in both CC and EC.

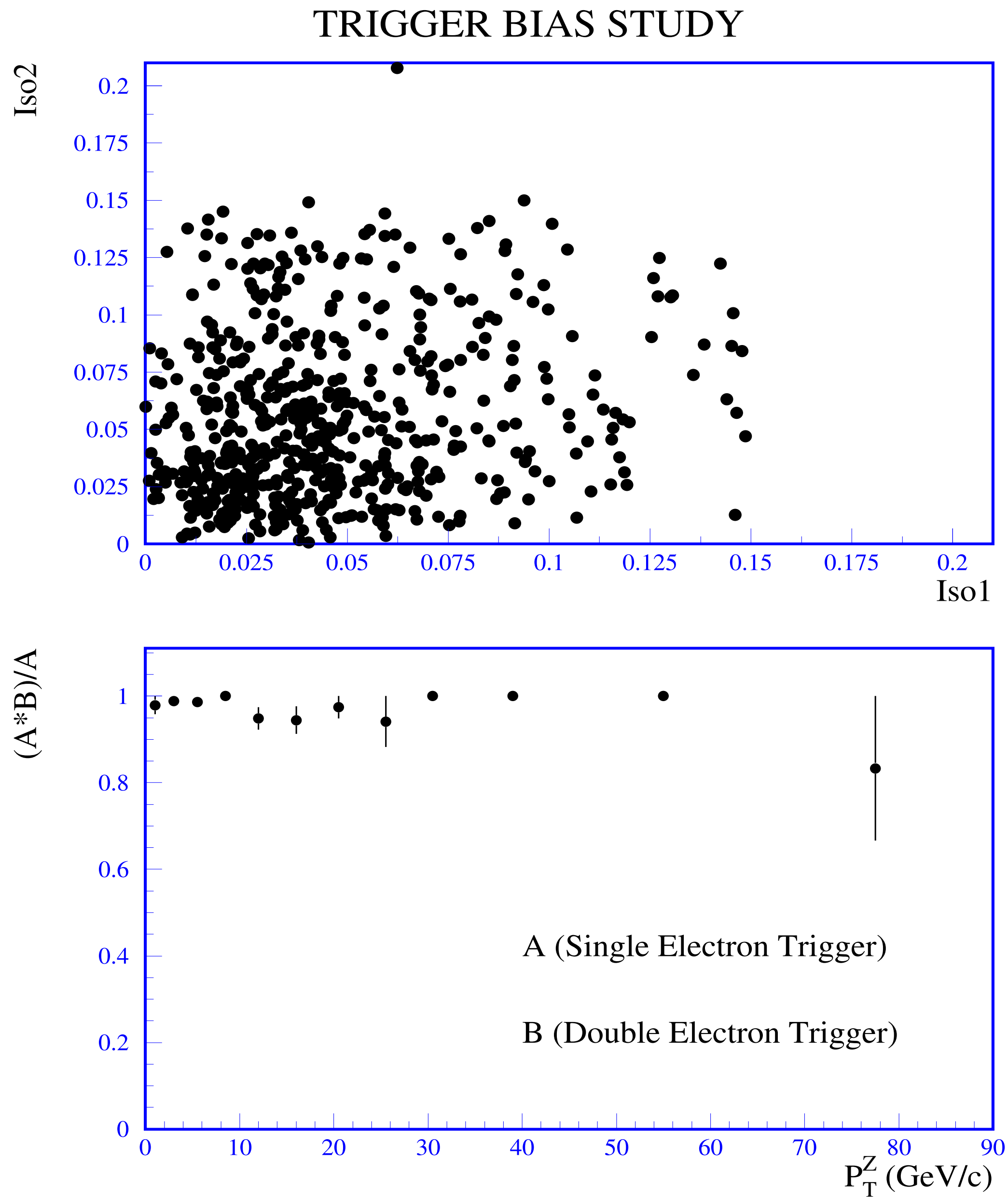

Figure 4.6: The trigger efficiency and bias study. The upper plot shows the isolation parameters of the Z electron are not correlated and the bottom plot shows the trigger efficiency as a function of Z p_T.

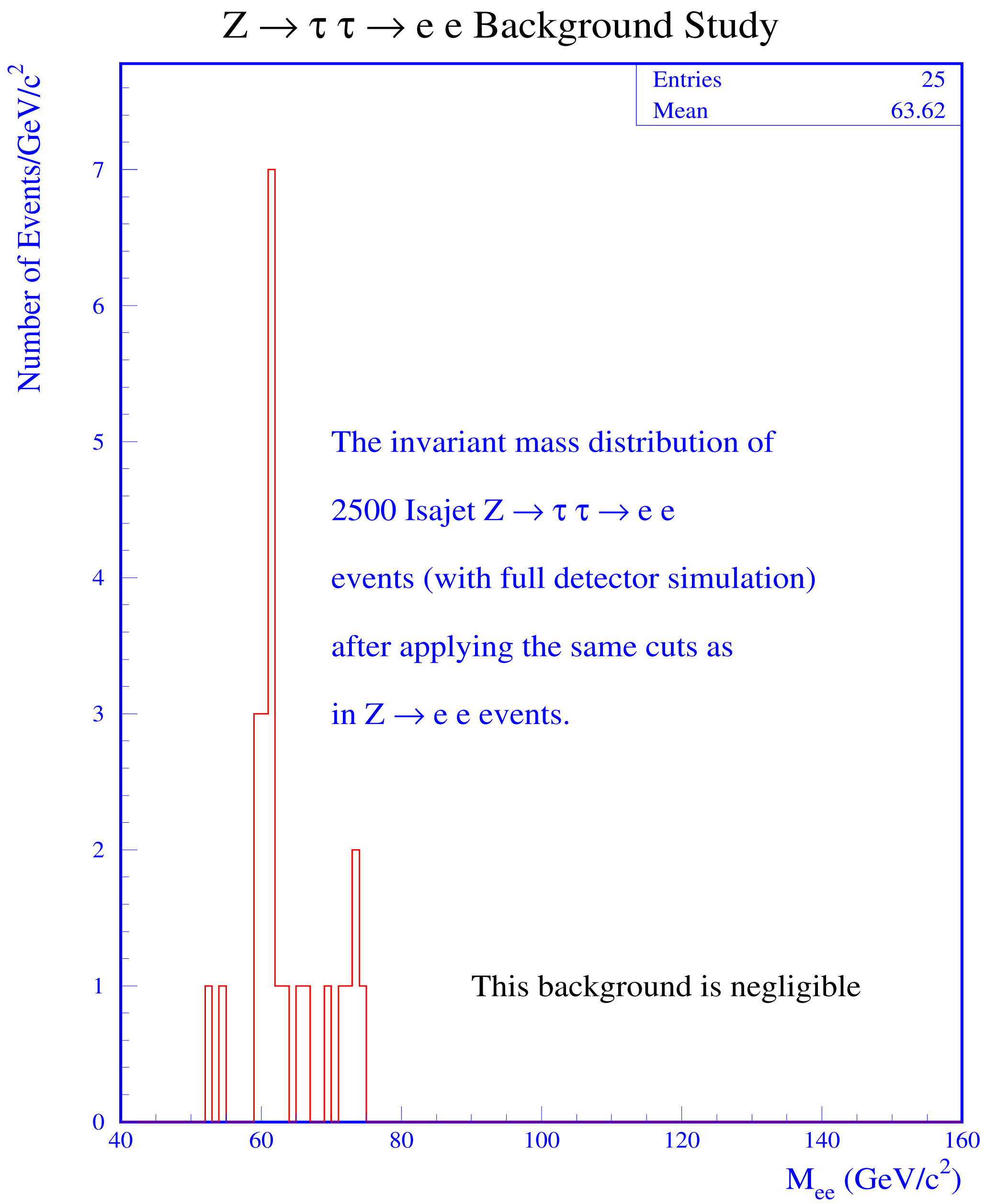

Figure 4.7: The $Z \to \tau\tau \to ee$ background estimation.

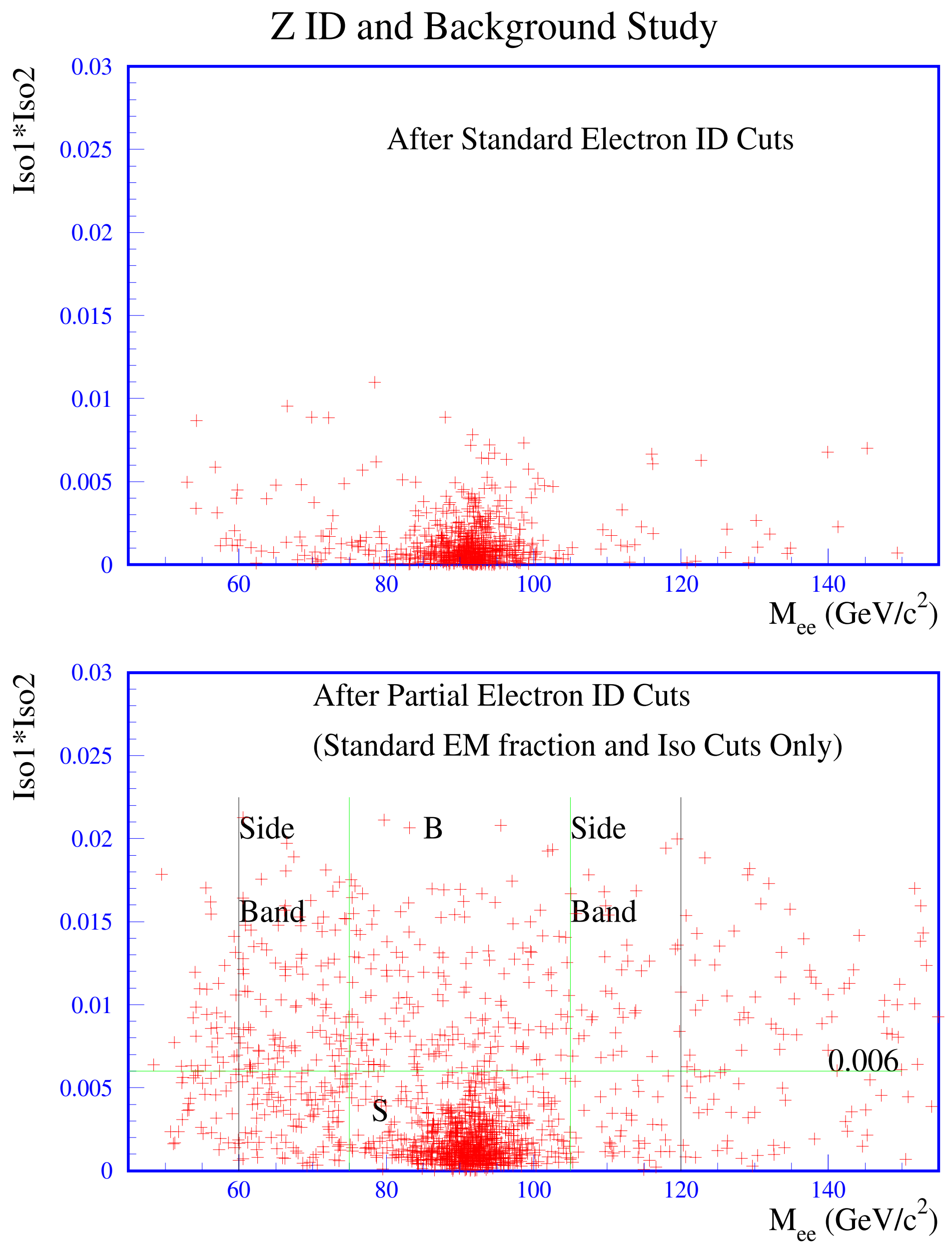

Figure 4.8: Background study. The upper plot shows the product of the two electron isolation parameters as a function of the di-electron invariant mass after the standard electron ID cuts. The bottom plot is after the partial electron ID cuts. The background events are more uniformly distributed, whereas the Z events are highly clustered in the S region.

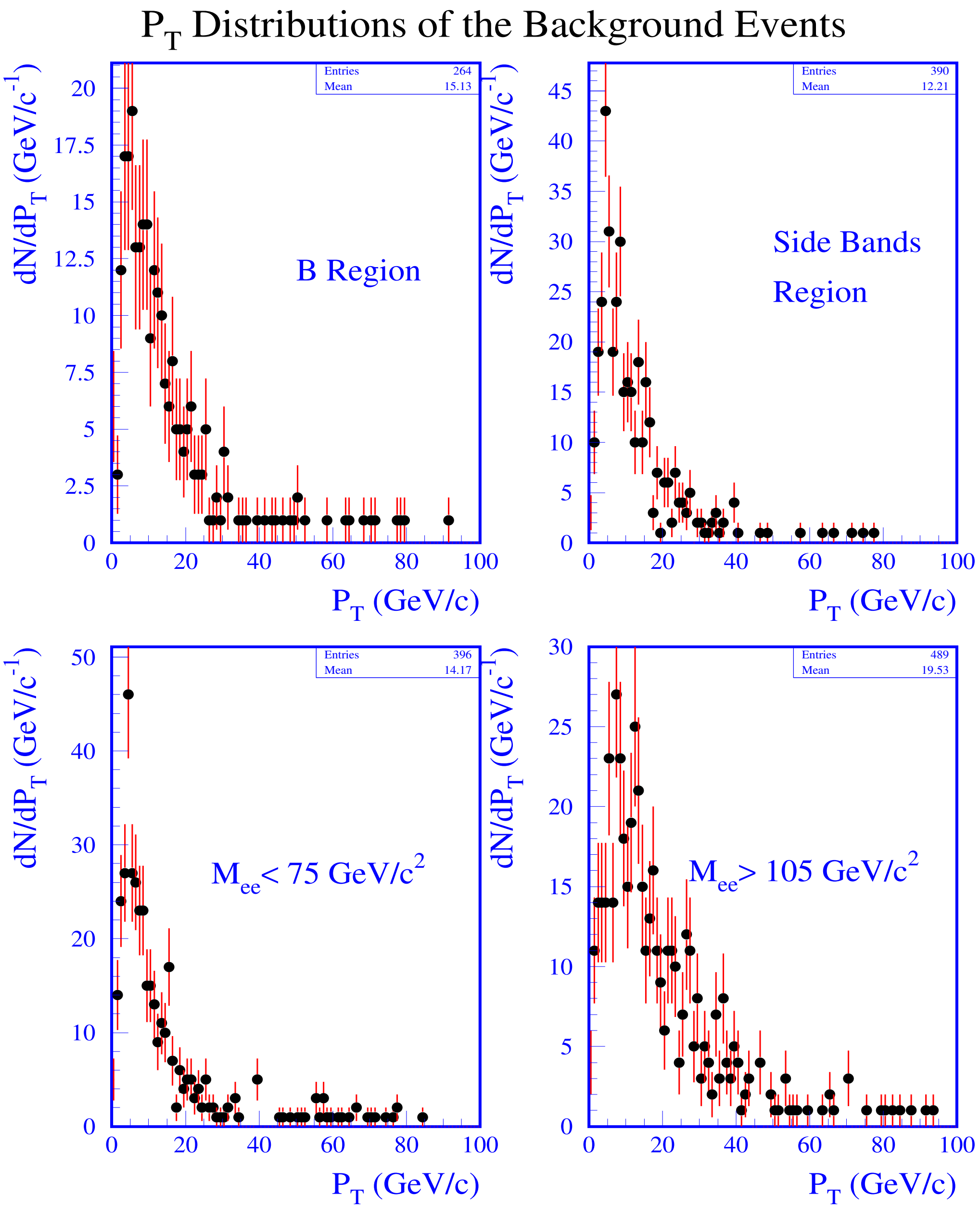

Figure 4.9: Background p_T distributions.

Chapter 5

Fast Monte Carlo Simulation of Z Production

5.1 Introduction

The reconstructed Z p_T distribution is biased by the kinematic (E_T) cuts, fiducial cuts, electron ID cuts, triggers, and resolution smearing. These effects need to be well modeled for the Z p_T measurement. A fast Monte Carlo program was developed to accomplish this [31].

5.2 Fast Monte Carlo Simulation

The starting point for the fast Monte Carlo (MC) simulation is the calculated double differential cross section, $d^2\sigma/dp_T^Z dy_Z$, where y_Z is the rapidity of Z. It contains most physical information for Z production. Theoretical calculations by Arnold-Kauffman [13] and Ladinsky-Yuan [15] are available and used as inputs. Fig. 5.1 shows an example of the double differential cross section calculated by Ladinsky and Yuan [15]. Z bosons are then generated according to the double differential cross sections and decay into e^+ and e^- with the angular distributions of $(1 \pm \cos\theta^\star)^2$, where $\theta^\star$ is the polar angle in the center of mass frame with respect to the proton-beam direction.

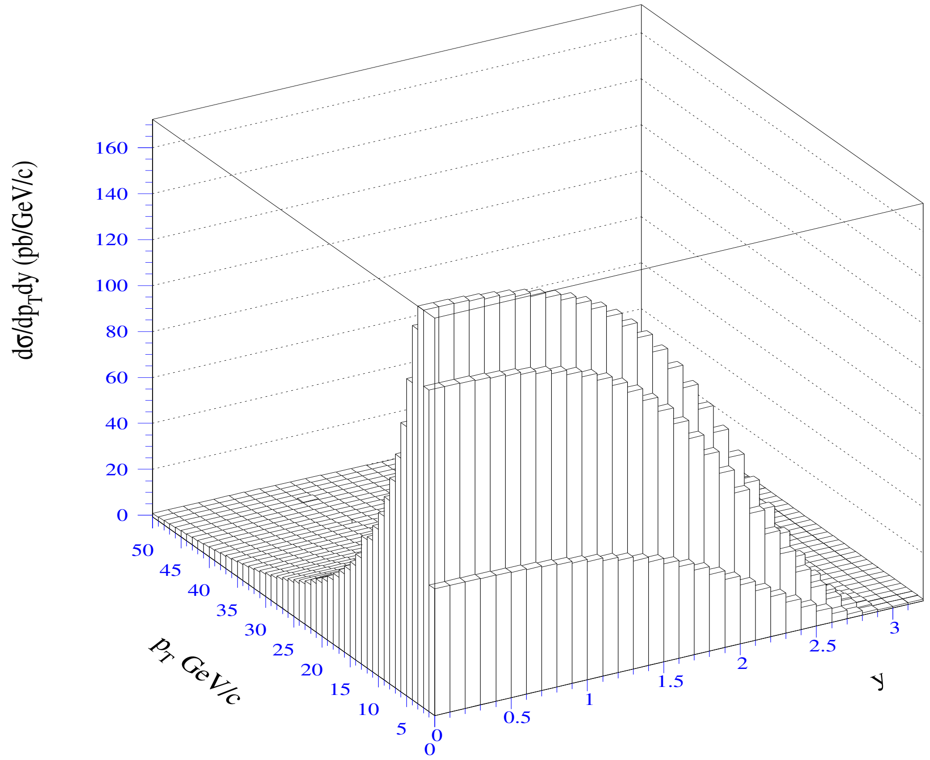

Figure 5.1: The double differential cross section for Z production. It is symmetrical between $+y$ and $-y$. Only the positive half is shown.

A relativistic Breit-Wigner shape is used to model the Z resonance line shape. The formula used is given in Eq. 5.1.

$$f(m) = \frac{m^2}{(m^2 - m_Z^2)^2 + \frac{m^4\Gamma_Z^2}{m_Z^2}} \tag{5.1}$$

where m_Z and Γ_Z are the mass and width of the Z boson. The parton luminosity change over the Breit-Wigner resonance region is modeled by an exponential decay factor, $e^{-\beta m}$, with $\beta = 0.009$ and is about 24%.

The recent results of $m_Z = 91.188$ GeV/c^2 and $\Gamma_Z = 2.493$ GeV/c^2 by the LEP experiments [5] are used to generate Z events.

5.2.1 Simple Detector and Event Selection Model

The Z electron detection and selection processes are simulated with a simple model.

The simple model is based on a set of input parameters extracted from the data. The model has the following features:

1. The event vertex distribution along the beam (z) direction is modeled with a Gaussian shape. For the 1992-1993 collider run, the collision center at DØ was not exactly at the detector center. Its mean and width are extracted from the Z candidate data sample before the selection cuts with $\overline{z}_{vertex} = -10.03 \pm 0.35$ cm, and $\sigma_z = 28.4 \pm 0.3$ cm as shown in Fig. 5.2.

2. The electron angular resolutions are modeled with Gaussian shapes as well. The upper limit of the standard deviations of these detector effects are extracted from Z data by fitting the difference ($\Delta\theta$ and $\Delta\phi$) of the measured Z electron calorimeter angles (θ_C and ϕ_C) and tracking angles

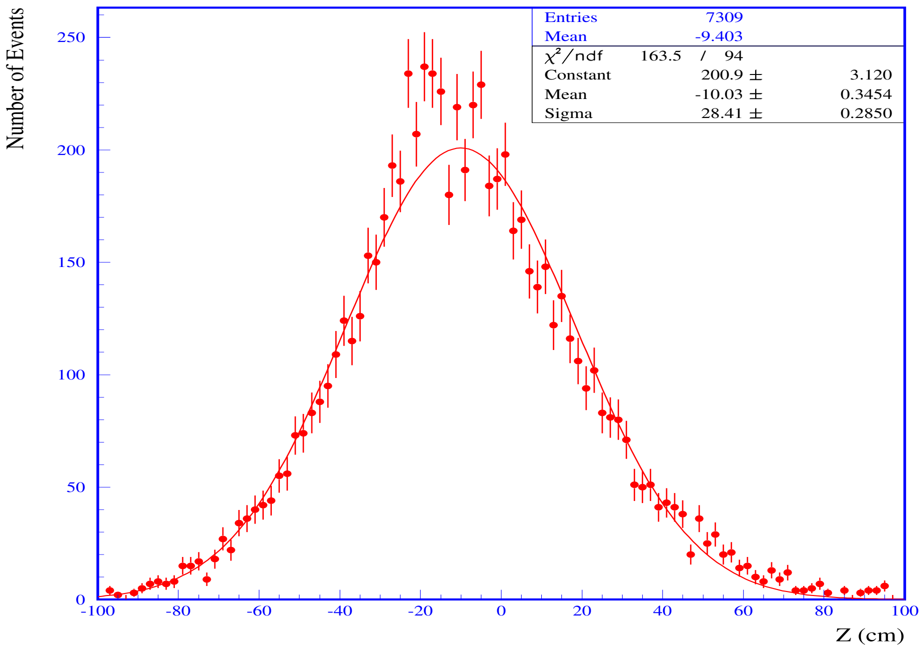

Figure 5.2: Event vertex distribution along the beam (z) direction.

(θ_T and ϕ_T) at both central (CC) and end (EC) calorimeter regions as shown in Fig. 5.3. The tracking angles result from fitting of the hits in the tracking chambers and the calorimeter angles are determined by connecting the center of gravity of the electron shower in the calorimeter and the event vertex position fitted by the tracking chambers. As shown in the equations below:

$$\Delta\theta = \theta_T - \theta_C, \quad \Delta\phi = \phi_T - \phi_C \tag{5.2}$$

$$\delta\Delta\theta = \sqrt{(\delta\theta_T)^2 + (\delta\theta_C)^2}, \quad \delta\Delta\phi = \sqrt{(\delta\phi_T)^2 + (\delta\phi_C)^2} \tag{5.3}$$

$$\delta\Delta\theta > \delta\theta_T, \quad \delta\Delta\theta > \delta\theta_C \tag{5.4}$$

$$\delta\Delta\phi > \delta\phi_T, \quad \delta\Delta\phi > \delta\phi_C \tag{5.5}$$

The standard deviations of the differences of the tracking angles and the calorimeter angles ($\delta\Delta\theta$ and $\delta\Delta\phi$) give the upper limits for the angular resolutions using either calorimeter angles or tracking angles and are listed in Table 5.1.

	CC (mr)	EC (mr)
$\delta\Delta\theta$	32.4 ± 1.2	9.5 ± 0.9
$\delta\Delta\phi$	4.7 ± 1.2	9.7 ± 0.6

Table 5.1: The upper limits of the electron angular resolutions.

We can also use $R_{\delta\theta} = \frac{\delta\theta_C}{\delta\theta_T}$ and $R_{\delta\phi} = \frac{\delta\phi_C}{\delta\phi_T}$ from expected resolutions; $\Delta\theta = \theta_T - \theta_C$ and $\Delta\phi = \phi_T - \phi_C$ from Z data to extract $\delta\theta_C$, $\delta\theta_T$, $\delta\phi_C$, and $\delta\phi_T$ separately. The procedure is described below:

From the tracking resolutions in $r - \phi$ and z ($\sigma_{r-\phi trk}$ and σ_{ztrk}), the calorimeter position resolutions (σ_{zcal} and $\sigma_{\phi cal}$), and the z vertex position resolution of the track fitting (σ_{vtx}) as discussed in chapter 3 and listed in Table 5.2,

	CC	EC
$\sigma_{r-\phi trk}$[19]	150 μm	200 μm
σ_{ztrk}	4 mm[22]	200 μm[19]
σ_{zcal}[22]	$\sim$ 6 mm	$\sim$ 2 mm
$\sigma_{\phi cal}$	$\sim$ 2 mm[22]	$\sim$ 1.4 mm[19]
σ_{vtx}[33]	$\sim$ 2 cm	$\sim$ 2 cm

Table 5.2: The numbers used in estimating the ratios of tracking and calorimeter angular resolutions. The $\sim$ signs mean averages approximately within 10% of errors.

we can roughly estimate the ratios ($R_{\delta\theta}$ and $R_{\delta\phi}$) of the calorimeter and tracking angular resolutions as the following:

$$\delta\theta_C \sim \frac{\sqrt{\sigma_{vtx}^2 + \sigma_{zcal}^2}}{D^{em3}}, \quad \delta\theta_T \sim \frac{\sqrt{2}\sigma_{ztrk}}{D^{trk}} \tag{5.6}$$

$$R_{\delta\theta} = \frac{\delta\theta_C}{\delta\theta_T} \sim \frac{\sqrt{\sigma_{vtx}^2 + \sigma_{zcal}^2} \cdot D^{trk}}{\sqrt{2}\sigma_{ztrk} \cdot D^{em3}} \tag{5.7}$$

$$\delta\phi_C \sim \frac{\sigma_{\phi cal}}{D^{em3}}, \quad \delta\phi_T \sim \frac{\sqrt{2}\sigma_{r-\phi trk}}{D^{trk}} \tag{5.8}$$

$$R_{\delta\phi} = \frac{\delta\phi_C}{\delta\phi_T} \sim \frac{\sigma_{\phi cal} \cdot D^{trk}}{\sqrt{2}\sigma_{r-\phi trk} \cdot D^{em3}} \tag{5.9}$$

where D^{em3} is the distance of the EM3 layer of the EM cluster in the calorimeter to the event vertex and D^{trk} is the length of the CDC or FDC portion of the track. Because the radius of the EM3 layer of the central calorimeter and the thickness of CDC are 91.6 cm and 20.1 cm respectively, the $\frac{D^{em3}}{D^{trk}}$ (CC) is $\frac{91.6}{20.1} = 4.6$. Since the distances of the EM3 layer of the end calorimeter to the detector center along the beam axis and the thickness of FDC are 178.9 cm and 30.4 cm respectively, the $< \frac{D^{em3}}{D^{trk}} >$ (EC) is $\frac{178.9}{30.4} = 5.9$. We then can obtain the ratios as listed in Table 5.3.

	CC	EC
$R_{\delta\theta}$	~ 0.8	~ 12.1
$R_{\delta\phi}$	~ 2.1	~ 0.8

Table 5.3: Estimation of $R_{\delta\theta}$ and $R_{\delta\phi}$.

Using the ratios, equation 5.3, and Table 5.1, we can estimate the tracking and calorimeter angular resolutions. The results are listed in Table 5.4 and 5.5.

	CC (mr)	EC (mr)
$\delta\theta_T$	~ 25.3	~ 0.8
$\delta\phi_T$	~ 2.0	~ 7.6

Table 5.4: Electron angular resolutions from tracking.

	CC (mr)	EC (mr)
$\delta\theta_C$	~ 20.2	~ 9.5
$\delta\phi_C$	~ 4.2	~ 6.1

Table 5.5: Electron angular resolutions from calorimeter.

In the data, we use the tracking angle for Z electron direction if the electron track is available. Gaussian distributions using the 1 σ values in Table 5.4 and Table 5.5 for the angular resolutions from tracking and calorimeter are used in the fast Monte Carlo simulation for both (a) (using tracking angles for both electrons) and (b) (using tracking angles for most of the electrons and calorimeter angles for a small fraction, $\approx 6.5\%$, of all electrons) samples discussed in section 4.4.4.

Since the electron p_T is calculated as:

$$p_T^e = p^e \cdot \sin\theta \tag{5.10}$$

and the measurement error of the electron p_T is:

$$\frac{\delta p_T^e}{p_T^e} = \sqrt{(\frac{\delta p^e}{p^e})^2 + (\frac{\delta\theta}{\tan\theta})^2} \tag{5.11}$$

the poorer angular resolution for θ in the CC as shown in Fig. 5.3, Table 5.4, and Table 5.5. does not affect the Z p_T resolution very much because of the large $\tan\theta$ value there.

3. The electron energy scale and resolution are modeled by assuming the energy scale is correctly set and smearing the energy measurement with a Gaussian shape and resolution of

$$(\frac{\sigma}{E})^2 = C^2 + (\frac{S}{\sqrt{E_T}})^2 \quad \text{(CC) [32]} \tag{5.12}$$

$$(\frac{\sigma}{E})^2 = C^2 + (\frac{S}{\sqrt{E}})^2 \quad \text{(EC)} \tag{5.13}$$

where S is a sampling term and C is a constant term. The sampling term S is constrained by the test beam data and the constant term C is constrained by the measured width of Z peak. The noise term discussed in section 3.2.5 is ignored because the Z electrons have very high energy. Table 5.6[1] shows the values used in the simulation.

4. The electron trigger simulation is implemented by using the detector η dependent Level 2 turn-on curves [27] as efficiencies for electrons to pass

[1]CC, ECN, and ECS stand for central calorimeter, end calorimeter north side, and end calorimeter south side respectively.

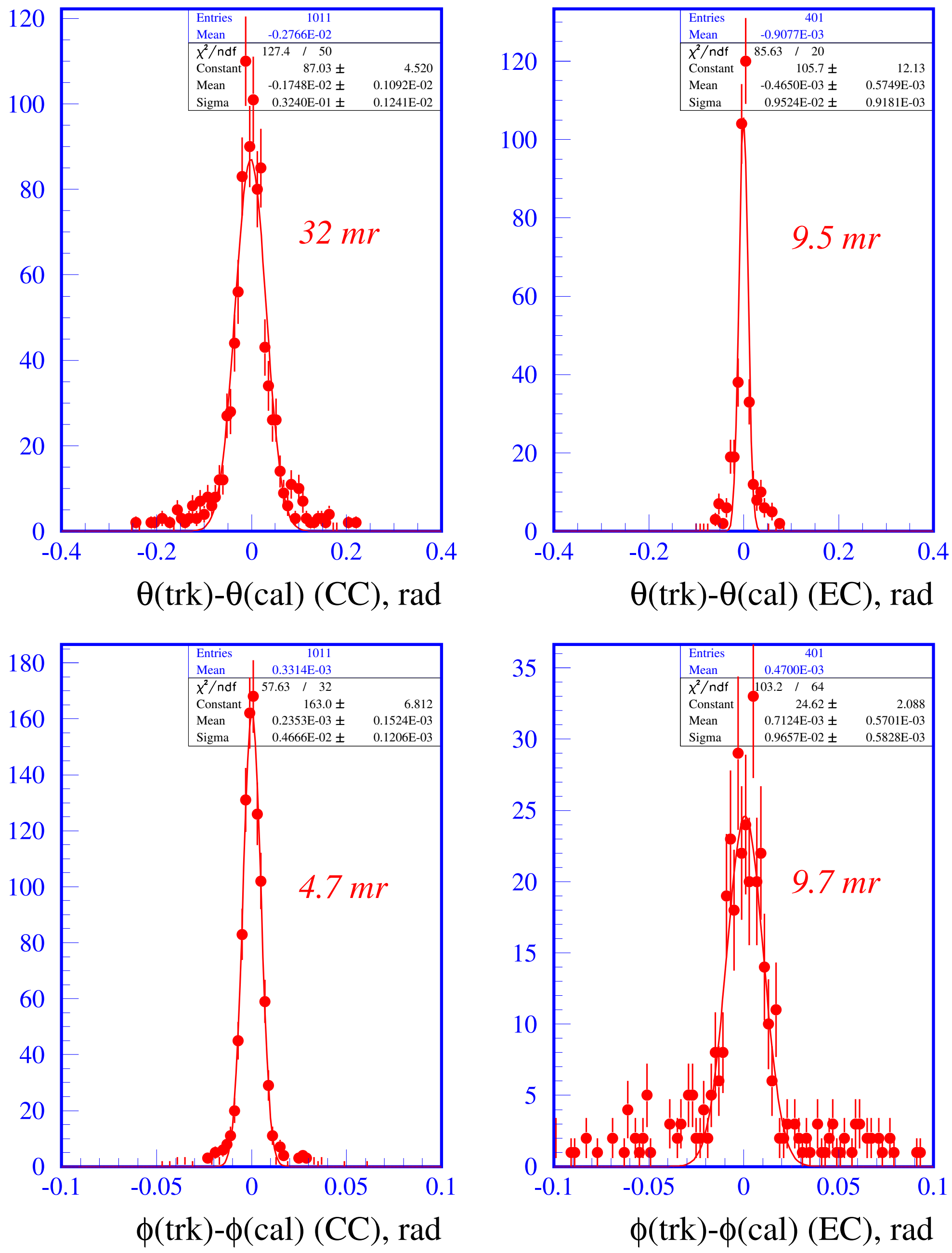

Figure 5.3: The distributions of the differences of the measured Z electron tracking angles and calorimeter angles. The lines are the Gaussian fit.

	CC	ECN	ECS
Constant Term	0.0212 ± 0.006	0.0316 ± 0.009	0.043 ± 0.01
Sampling Term	0.13 ± 0.05	0.157 ± 0.05	0.157 ± 0.05

Table 5.6: Electron energy resolution.

the filter. Level 1 efficiencies with different E_T thresholds are studied with the Z electrons and shown in Fig. 5.4 and Fig. 5.5, where the data for different calorimeter modules are folded into one module. Since Level 1 is fully efficient around E_T threshold of 10 GeV, there is no need to simulate it.

Due to uncertainty of the electron E_T measurement by the level 2 filter, the E_T threshold for the Level 2 turn-on is smeared. The level 2 turn-on curves are obtained by plotting the fraction of the electrons that passed a trigger E_T threshold as a function of the more accurate E_T from the reconstruction program with a data sample selected by a single electron trigger with an E_T threshold of 15 GeV. At the beginning of the collider run Ia, the level 2 assumed the event vertex to be at the detector center in calculating electron E_T. There is $\frac{1}{3}$ of data collected this way. A more sophisticated way (slow z) of calculating the event vertex position was implemented later at level 0 [2] to provide level 2 with more accurate information in calculating electron E_T. In the fast Monte

[2]It uses the time difference of the signal arriving at the two end scintillators to calculate z vertex position.

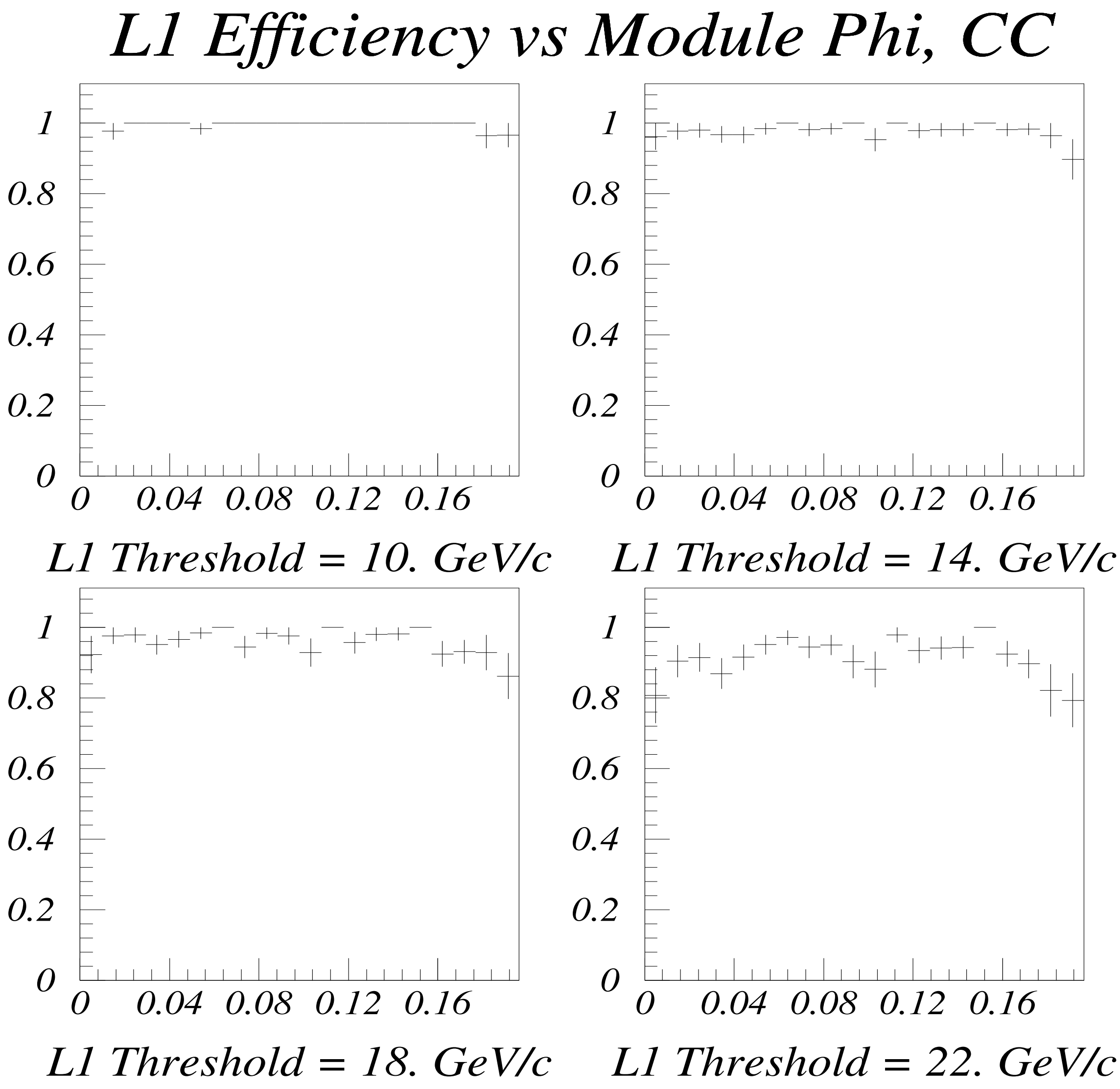

Figure 5.4: Level 1 efficiencies(vertical axes) as a function of module ϕ in CC at different E_T thresholds. The upper left plot has many points with 100% efficiencies and therefore no statistical errors.

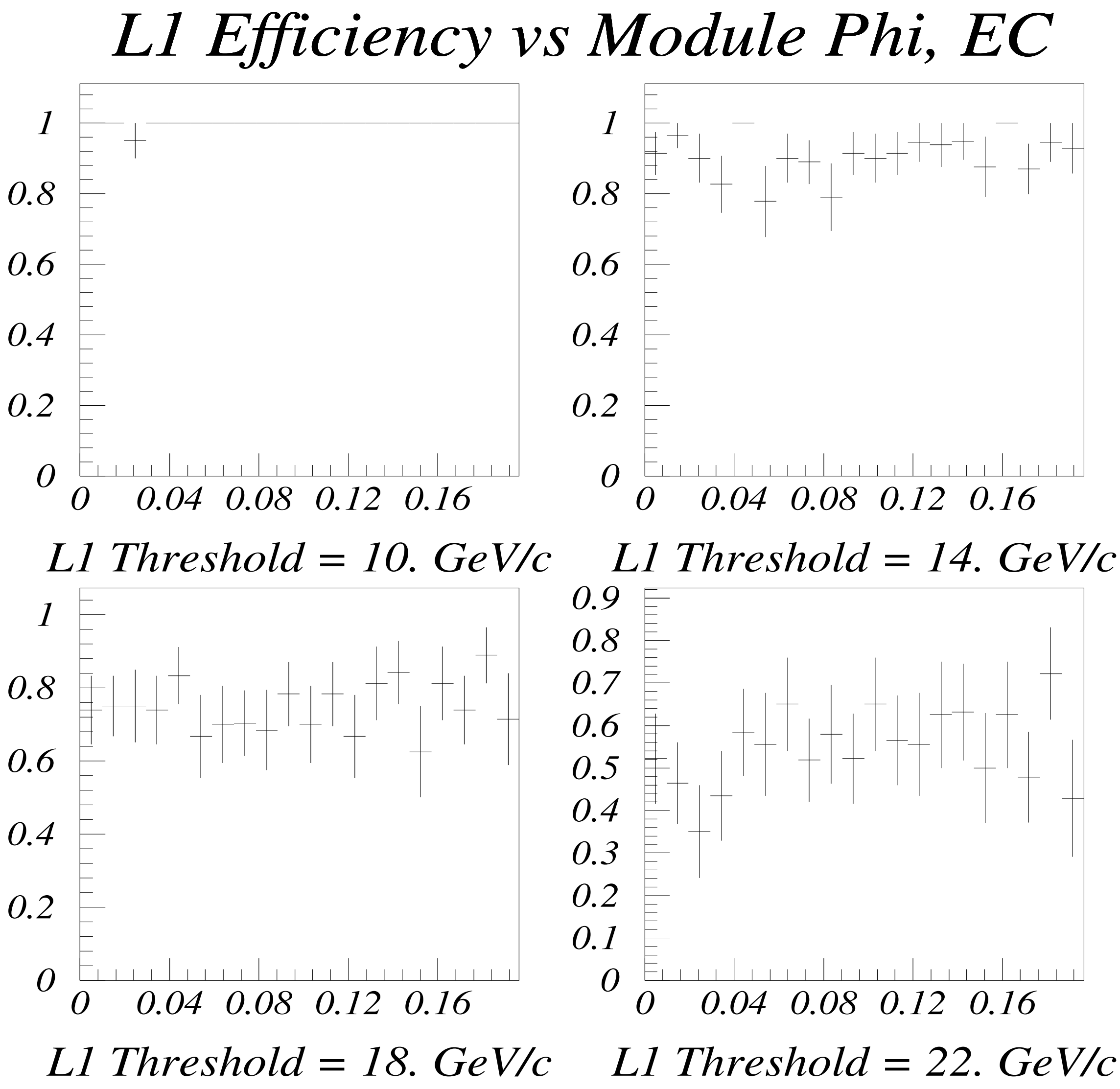

Figure 5.5: Level 1 efficiencies (vertical axes) as a function of module ϕ in EC at different E_T thresholds. The upper left plot has many points with 100% efficiencies and therefore no statistical errors.

Carlo, the change in the vertex determination is reflected by generating events with $\frac{1}{3}$ without slow z correction.

Figure 5.6-Fig. 5.9 show examples of the level 2 turn-on curve, where the percentages of the electrons passing both the trigger E_T and reconstructed E_T are plotted as a function of the reconstructed E_T for different trigger conditions.

5. The electron fiducial and kinematic cuts are set as same as in the data.

6. The electron ID cuts are simulated by applying the electron ID efficiencies obtained from the Z data sample. Shown in Table 4.7 are the electron ID efficiencies for standard and tight-loose electron ID cuts respectively. The model does not simulate the detector response to electrons, but simply decide whether a given electron passes our cuts based on the electron ID efficiency (ε). A fraction of the electrons $(1 - \varepsilon)$ is randomly rejected.

5.2.2 Comparison between the Fast Monte Carlo Simulation and Data

Detailed comparisons on many features between the Monte Carlo simulation and data are performed to establish the model.

Figure 5.10 shows the comparisons for vertex, electron pseudorapidity (η), electron E_T, and di-electron invariant mass distribution. The fraction of events with a decay electron in a given detector region is properly reproduced and the cracks in the inter cryostat regions are correctly modeled, as shown in the electron η distribution (the small disagreement in the EC regions is due to the fact that there are more background events in the EC regions and does not significantly affect the p_T measurement). The agreement in the invariant mass distribution indicates that the electron energy resolution is properly modeled.

Good agreement is also shown in Figure 5.11 for the two electron angular difference distributions ($\Delta\phi^{ee}$ and $\Delta\theta^{ee}$).

Since the Z momentum is known, comparisons are also made for the longitudinal distributions. Good agreements in the Z rapidity and Feynman X distributions [3] as shown in Fig. 5.12 indicate that the longitudinal production properties are also well modeled.

[3] $X_Z = \frac{2P_L^Z}{\sqrt{s}}$, where P_L^Z is the Z longitudinal momentum and $\sqrt{s}$ is the total center of mass energy.

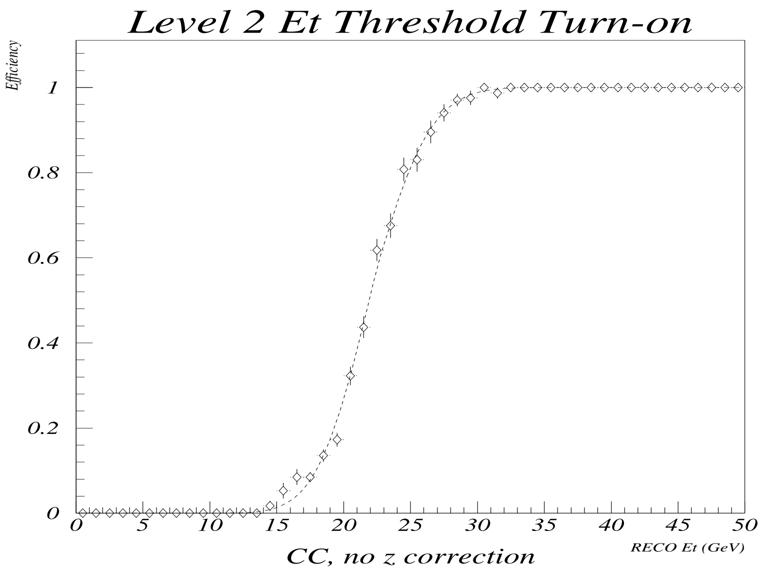

Figure 5.6: Turn-on curve for CC electrons without slow z correction.

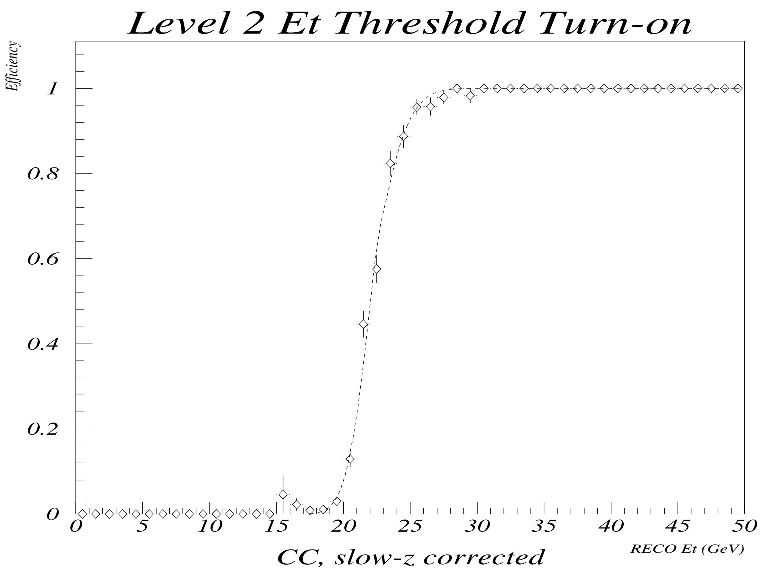

Figure 5.7: Turn-on curve for CC electrons with slow z correction.

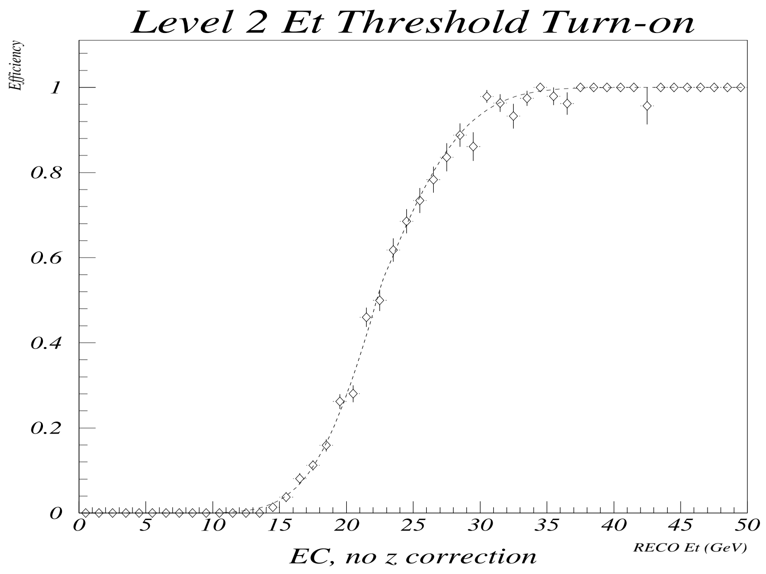

Figure 5.8: Turn-on curve for EC electrons without slow z correction.

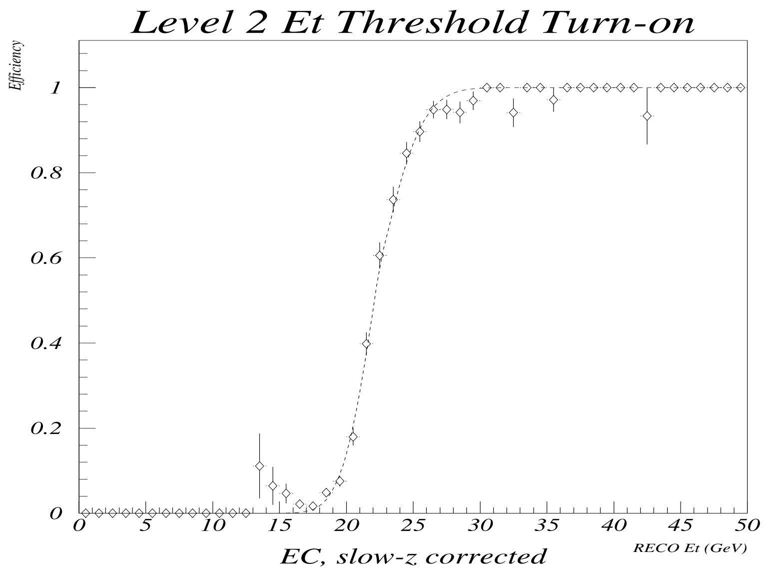

Figure 5.9: Turn-on curve for EC electrons with slow z correction.

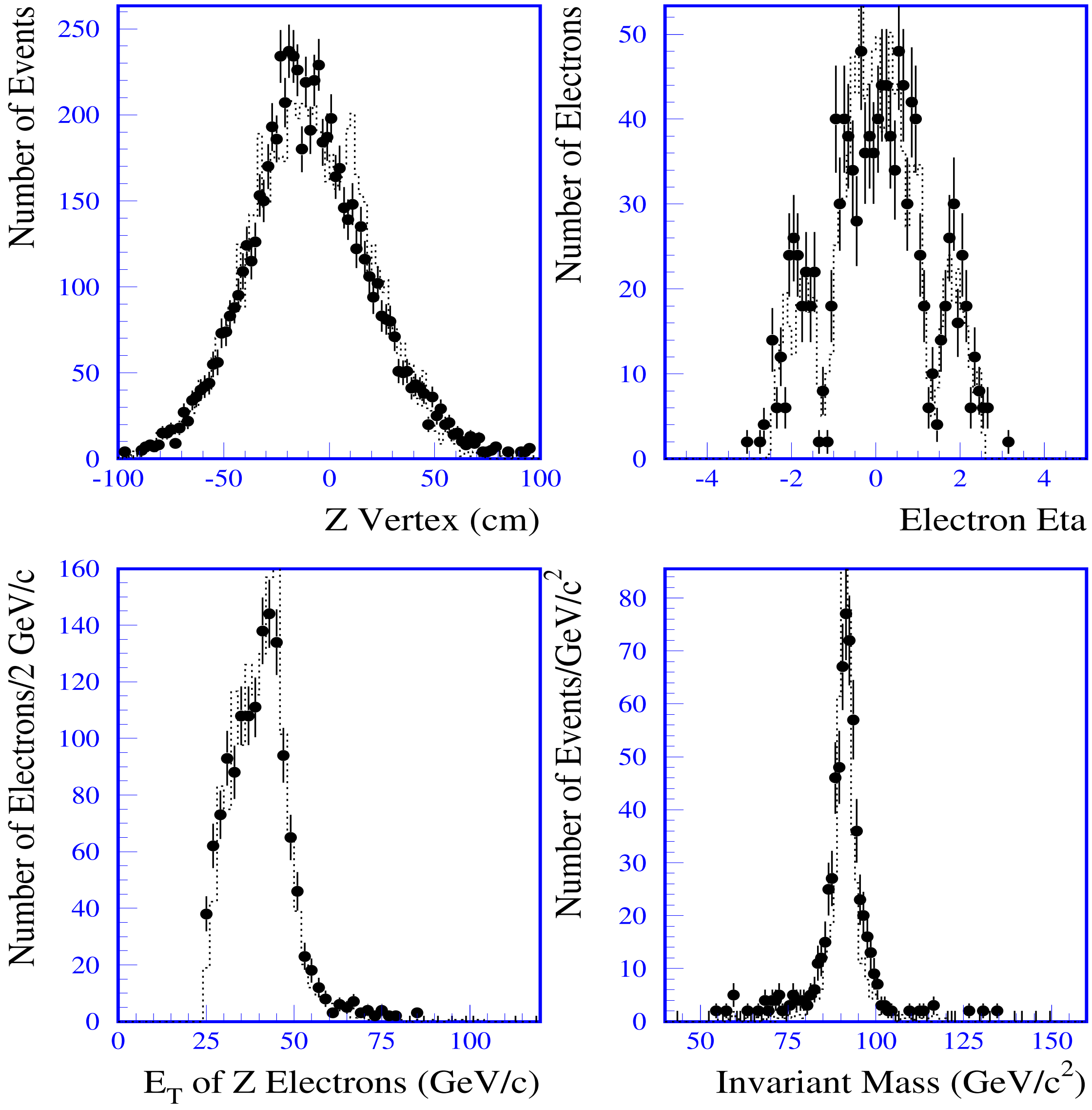

Figure 5.10: Comparison of the fast Monte Carlo predictions and data: z vertex, electron η, electron E_T, and di-electron invariant mass distributions. The solid histograms are data and the dotted histograms are MC.

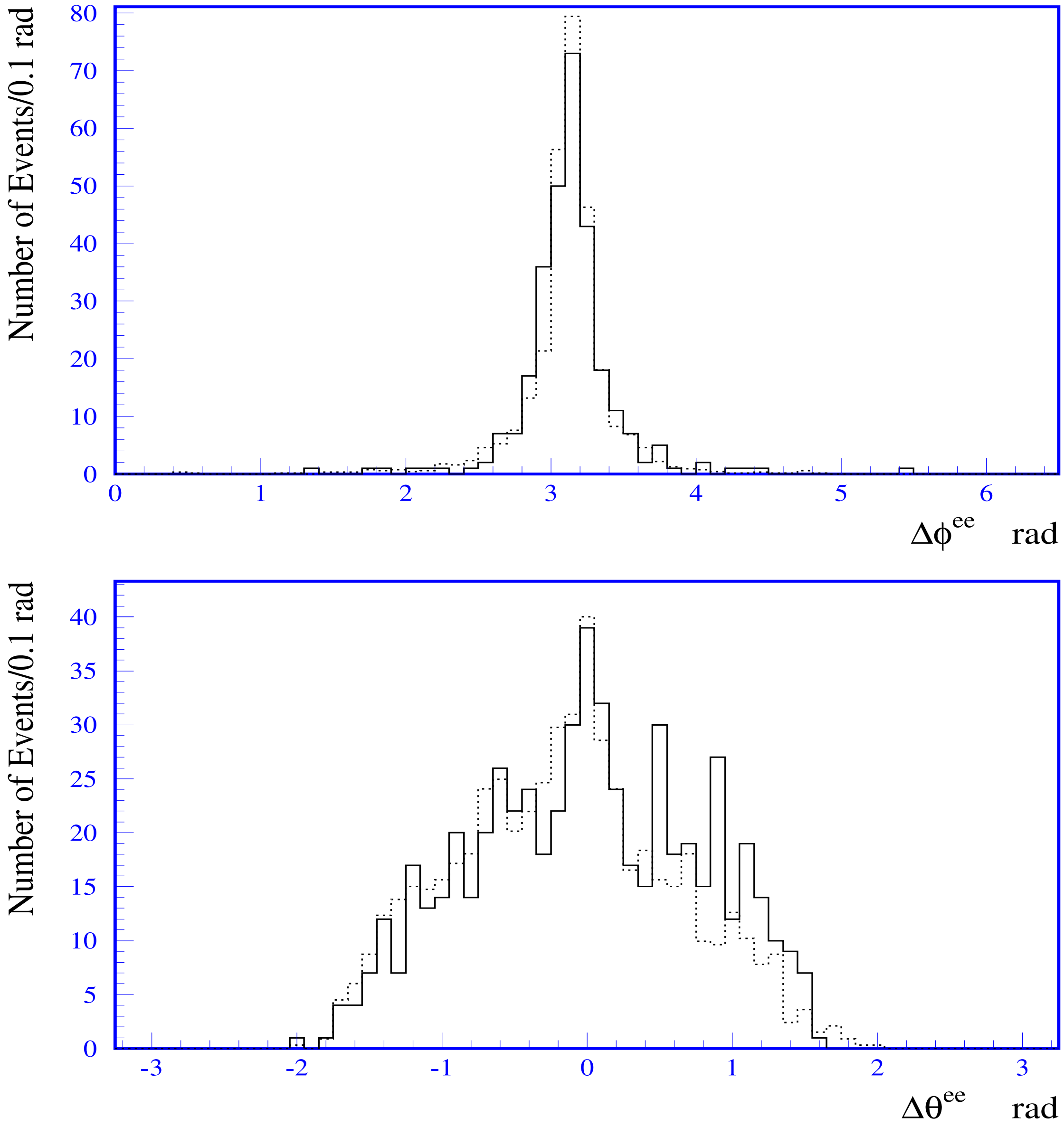

Figure 5.11: Comparison of the fast Monte Carlo predictions and data: two electron angular difference distributions ($\Delta\phi^{ee}$ and $\Delta\theta^{ee}$). The solid histograms are data and the dotted histograms are MC predictions.

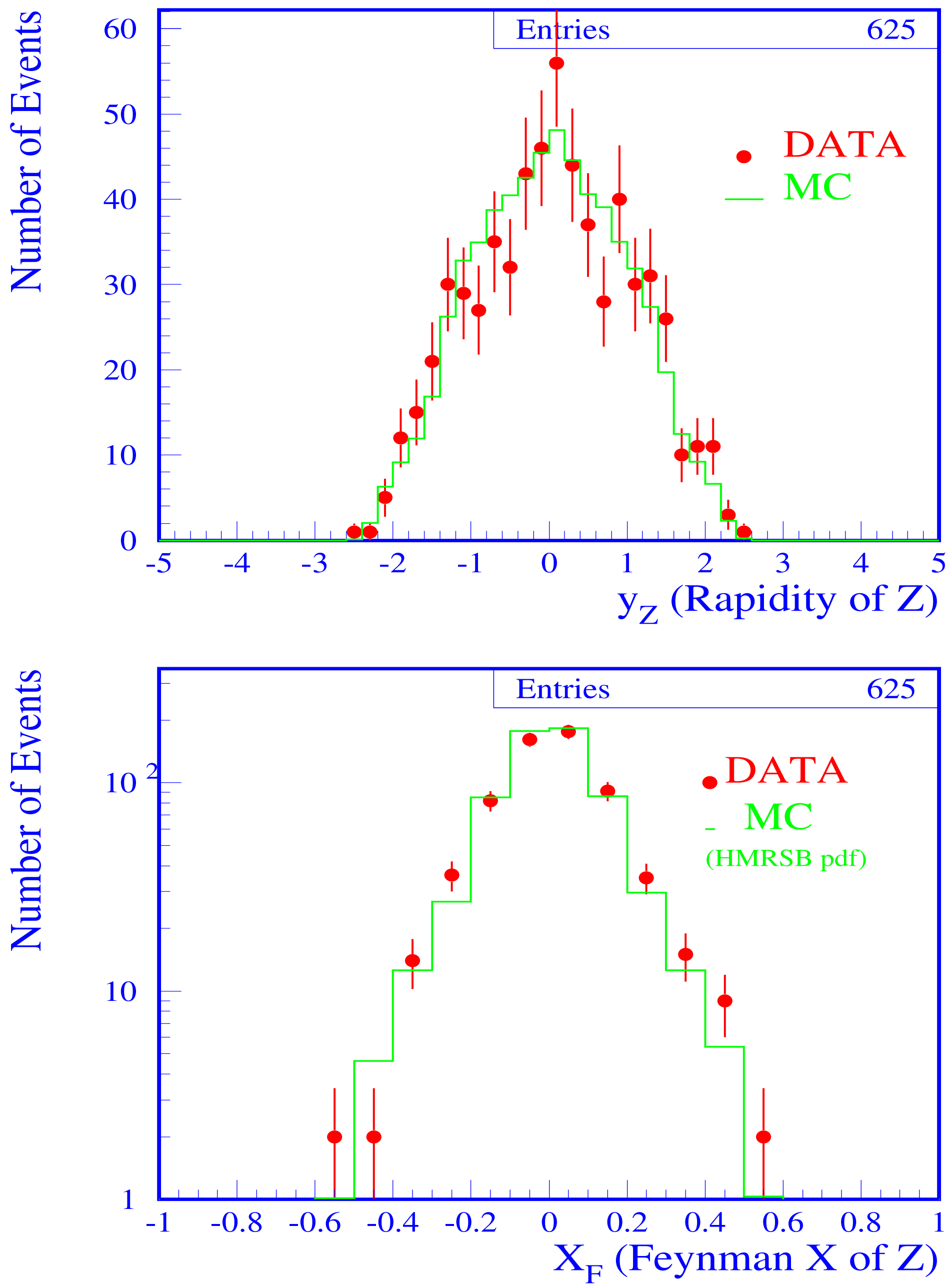

Figure 5.12: Comparison of the fast Monte Carlo predictions and data: longitudinal distributions.

Chapter 6

dN/dp_T Measurement

6.1 Introduction

Having examined the quality of the data sample and established the Monte Carlo simulation, we now proceed to measure the inclusive p_T^Z distribution.

p_T^Z can be reconstructed as the vector sum of the transverse momenta of 2 decay electrons. The measurement errors on p_T^Z depend on the electron energy and angular resolutions. The η component of p_T^Z, where the η direction is defined as the inner bisector of the angle between the transverse directions of the two decay electrons shown in Fig. 6.1 is relatively insensitive to the electron energy resolution and least smeared, relying mainly on the angles of the two electrons, due to the fact that most of Z electrons are decaying back to back. The η component of p_T^Z therefore can be used to calibrate the jets, recoil energy, and $\not{E}_T$. In this chapter, we compare data and theory for both p_T and p_η distributions.

Using the fast Monte Carlo program, we can study the energy and angular resolution smearing effects, as shown in Fig. 6.2 and Fig. 6.3. Here we use the default Ladinsky-Yuan production model (see section 6.2) to generate Z events; the estimated tracking angular resolutions from Table 5.4 are used for electron angular smearing in the MC. It is clear that the smearing due to the electron energy resolution is much larger than that due to the electron angular resolution. The difference of the input p_T and the smeared p_T distribution and that of the input p_η and the smeared p_η distribution are plotted in Fig. 6.4 and the rms resolutions are extracted to be 1.4 GeV/c and 0.4 GeV/c for p_T and p_η measurement respectively.

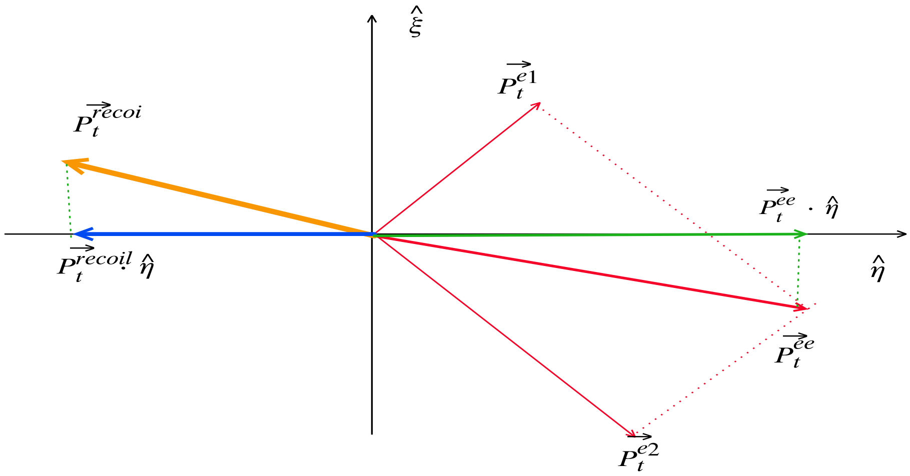

Figure 6.1: Schematic view of the η direction.

6.2 dN/dp_T Measurement

Let us first compare our data[1] with the smeared[2] theoretical predictions. Figure 6.5 shows the comparison with both Arnold-Kauffman[13] and Ladinsky-Yuan calculations[15] using their nominal values for the parameters in the nonperturbative function as described in chapter 1, $\Lambda_{\rm QCD}$ = 190 MeV, and HMRS(B) pdf in both models. The smeared theoretical predictions are normalized to the total number of events in the data. Above 7 GeV/c, the data agree with either model. Only in the low p_T region do the models need to be further modified.

[1]For the dN/dp_T measurement, the standard cuts for electron ID are used. The corresponding efficiencies are used for the fast MC.

[2]Smeared here means after applying all the detector and selection effects.

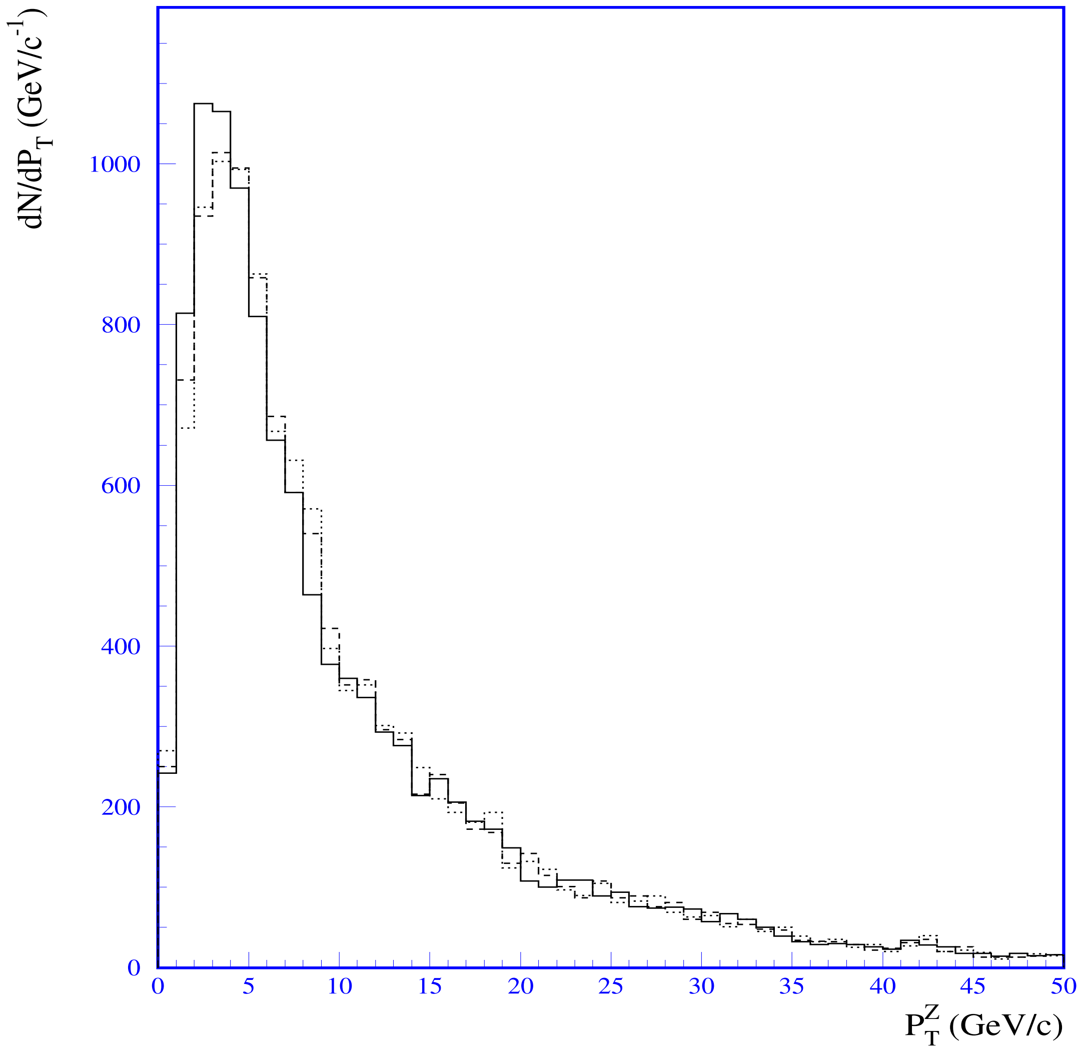

Figure 6.2: The energy and angular resolution effects on the p_T distribution (linear plot). The solid histogram is the initial p_T distribution, the dashed is after the electron energy resolution smearing, the dotted is after both electron energy and angular smearing (the estimated tracking angular resolutions from Table 5.4 are used in the MC).

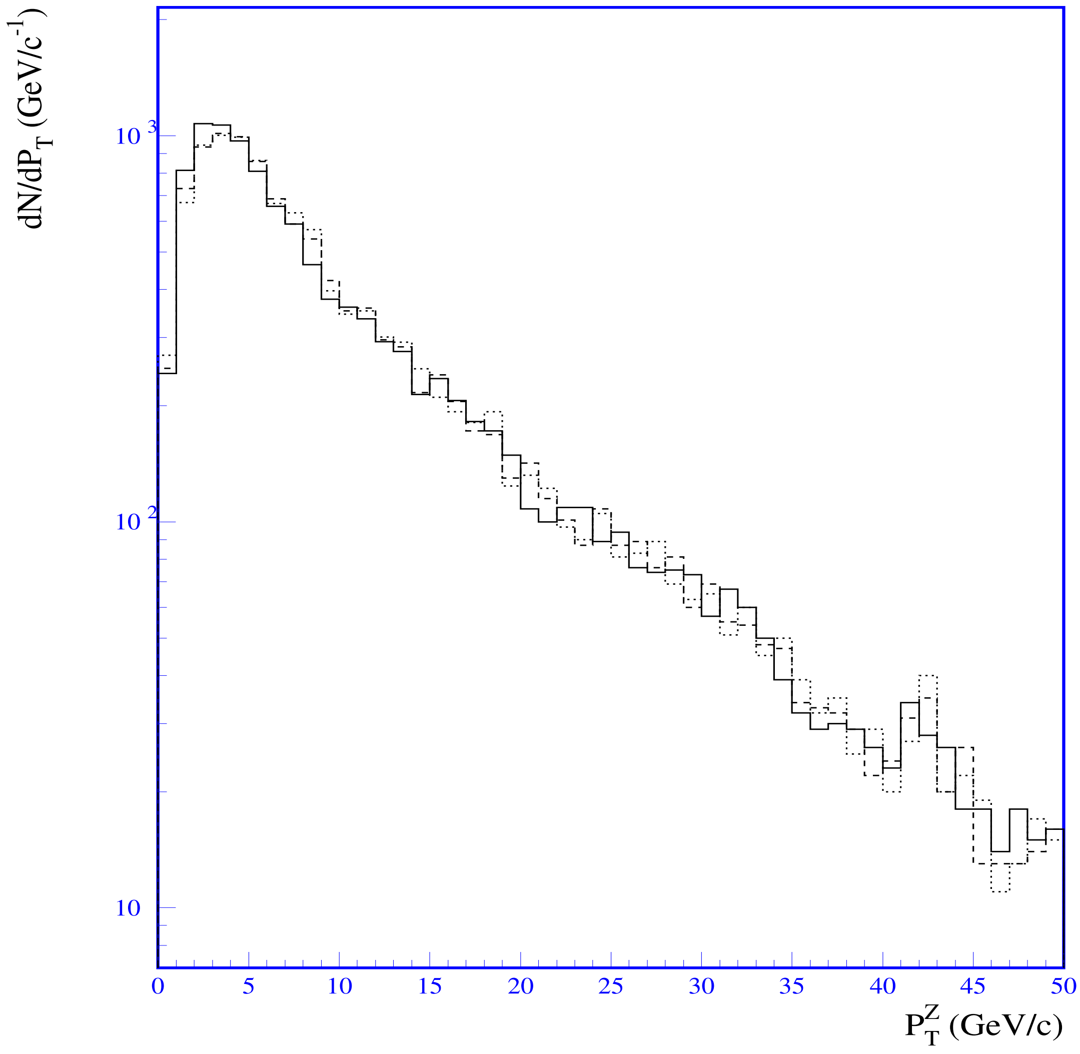

Figure 6.3: The energy and angular resolution effects on the p_T distribution (semi-log plot). The solid histogram is the initial p_T distribution, the dashed is after the electron energy resolution smearing, the dotted is after both electron energy and angular smearing (the estimated tracking angular resolutions from Table 5.4 are used in the MC).

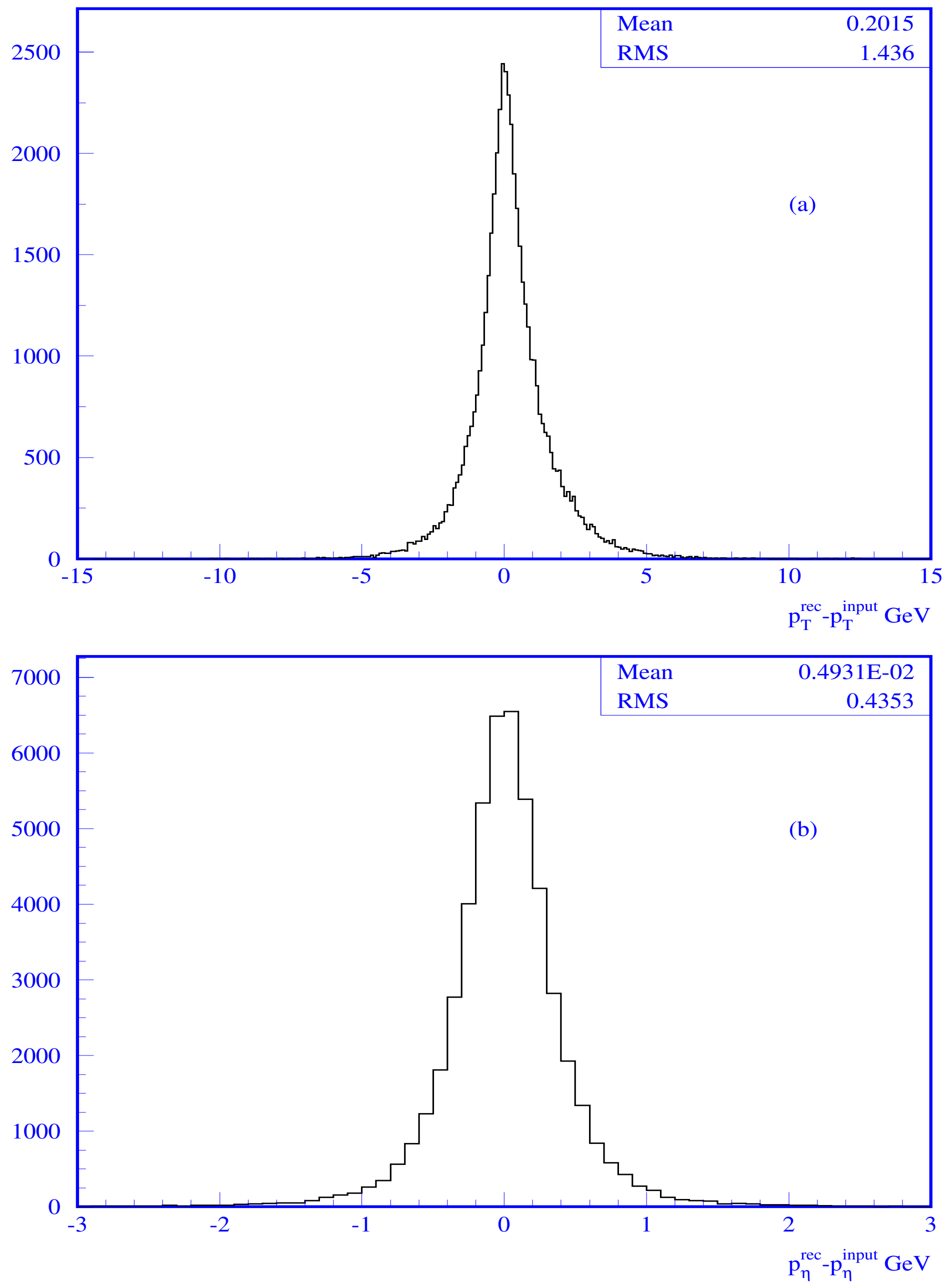

Figure 6.4: Difference between the input and smeared p_T distribution with a rms value of 1.4 GeV/c (a) and difference between the input and smeared p_η distribution with a rms value of 0.4 GeV/c (b).

6.3 dN/dp_η Measurement

Since the resolution of the p_η measurement is much better than that of the p_T measurement, comparison between data and MC is also made for the dN/dp_η distribution.

Figure 6.6 shows good agreement between MC and data. Again, the smeared theoretical predictions are normalized to the total number of events in the data. A previous measurement by the UA2 collaboration[34] showed disagreement.

6.4 Optimization of the Parameters in the Nonperturbative Function

The parameters in the nonperturbative function are tuned to better fit the measured Z p_T distribution. Using MC, the peak position of the predicted p_T distribution is found to be sensitive to the value of g_2. The values of g_2 are increased or decreased by $\pm\sigma$ in the Ladinsky-Yuan parameterization as discussed in 1.10 and the double differential cross sections are recalculated and smeared. The χ^2 fits between the smeared theoretical predictions and the data are calculated and plotted in Fig. 6.7. The points in Fig. 6.7 are fitted with a polynomial function and the minimum of the fitted curve gives the best value of g_2 ($\sim g_2^0 + 2\sigma$). The error of the fitted g_2 value is estimated to be the excursion needed in g_2 to give $\Delta\chi^2 = 1$ and is about ± 0.1 GeV^2 from Fig. 6.7.

It favors a set of parameters with:

$$g_2 = g_2^0 + 2\sigma \pm \sigma = 0.58 + 2 \cdot 0.1 \pm 0.1 = 0.78 \pm 0.1 \;\; \text{GeV}^2 \tag{6.1}$$

$$g_1 = g_1^0 = 0.11^{+0.04}_{-0.03} \;\; \text{GeV}^2 \tag{6.2}$$

$$g_3 = g_3^0 = -1.5^{+0.1}_{-0.1} \;\; \text{GeV}^{-1} \tag{6.3}$$

and provides further constraint on the Ladinsky-Yuan parameterization.

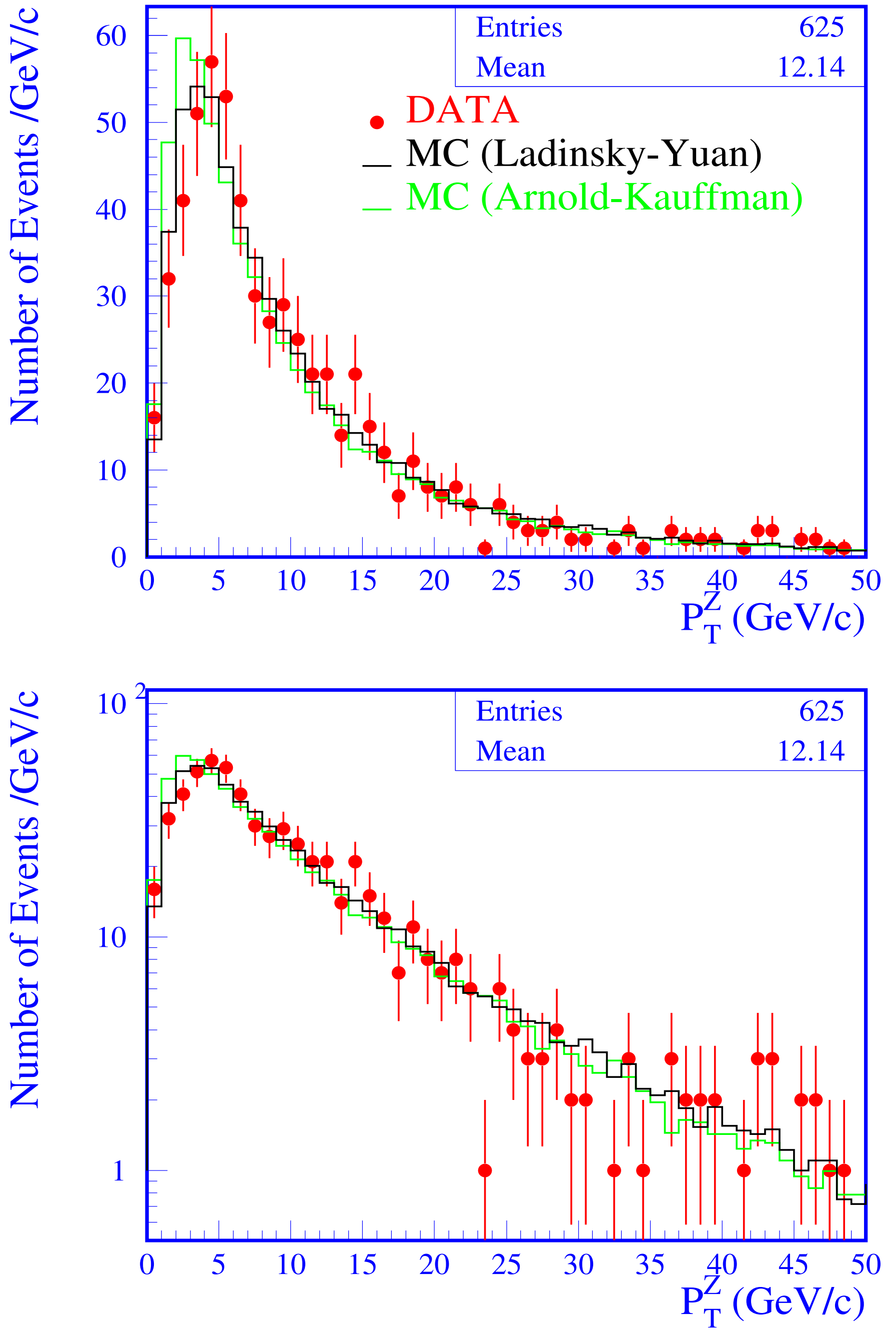

Figure 6.5: p_T^Z measurement. The bottom plot has log scale for the vertical axis.

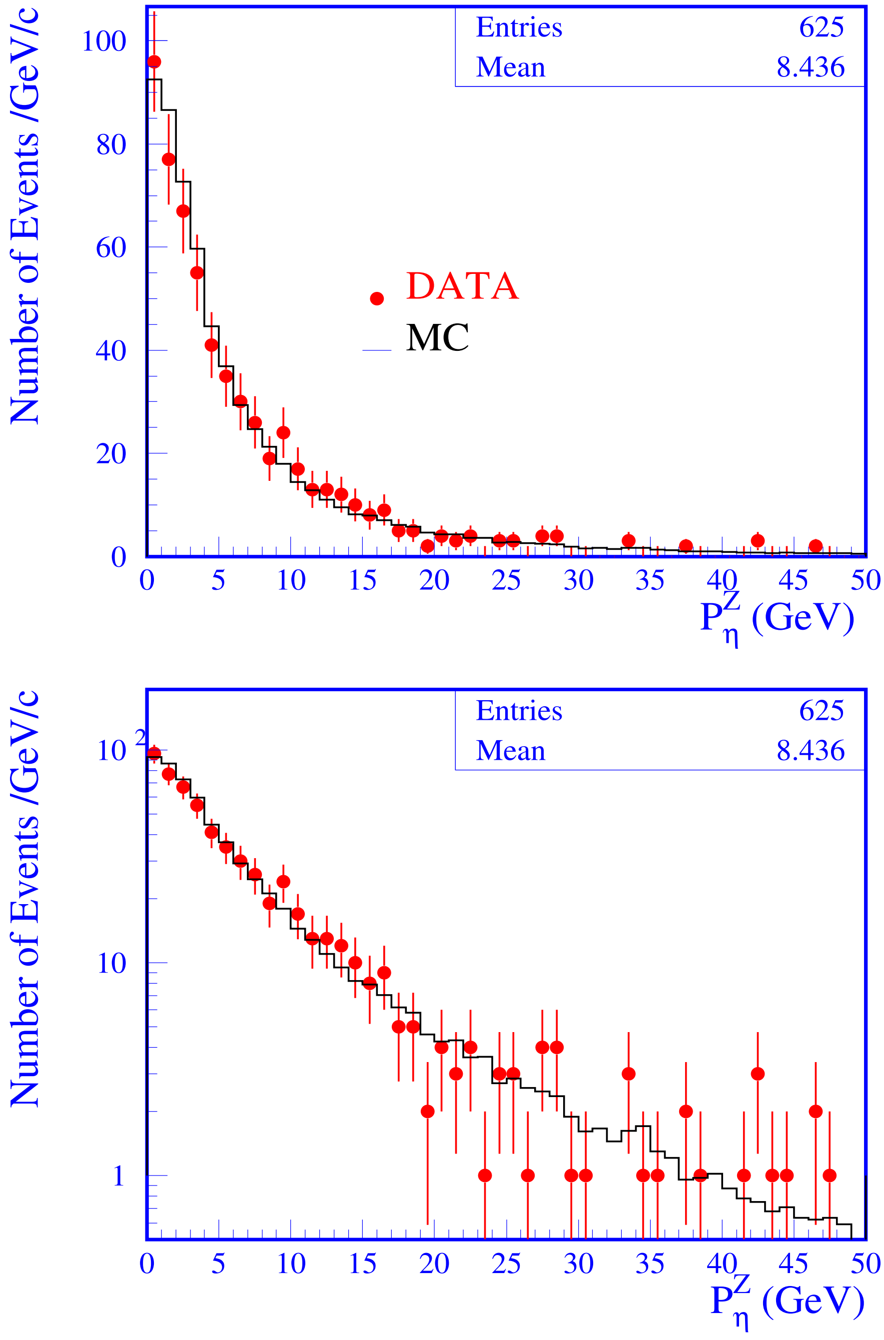

Figure 6.6: p^Z_η measurement. The default Landinsky-Yuan calculation is compared here and the bottom plot has log scale for the vertical axis.

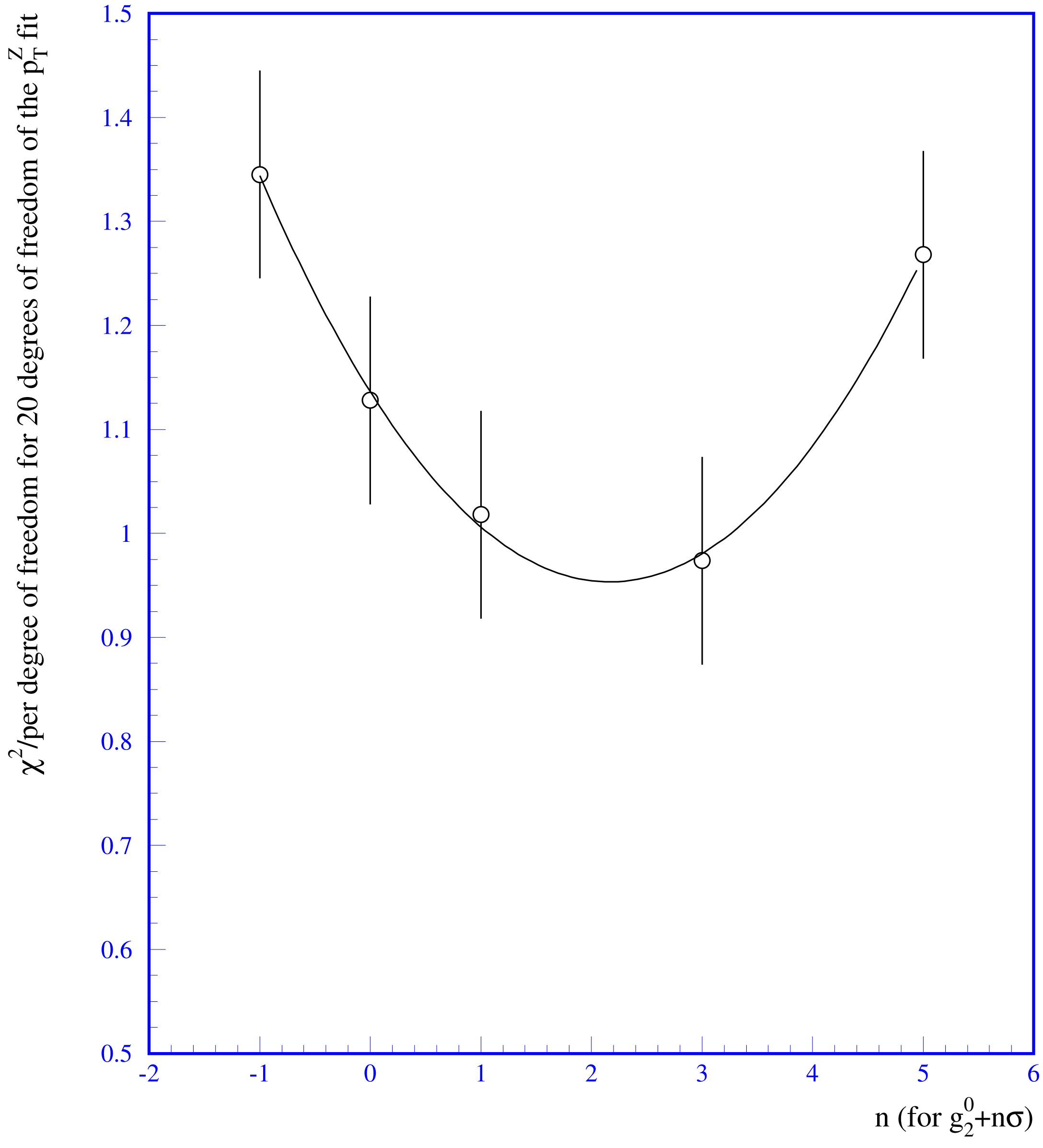

Figure 6.7: Optimization of g_2. The vertical axis is the χ^2 between data and MC p_T distributions and the horizontal axis is the number of σ's added to g_2^0 in the model.

Chapter 7

$d\sigma(p\overline{p} \longrightarrow Z)/dp_T$ Measurement

7.1 Introduction

The differential cross section is interesting because it provides important tests of our understanding of the Standard Model. Although the comparison between theoretical predictions and experimental measurement can be achieved by smearing the theory, it is desirable to unfold the detector and event selection effects on the data so that our measurement can be directly compared with any theoretical prediction.

In this chapter, the detector and selection effects on the p_T distribution and the methods used to unfold these effects are discussed. The $d\sigma/dp_T$ result is presented and its uncertainties are assessed.

7.2 Acceptance

Many Z events are lost due to the finite detector coverage and the offline selection cuts. With 150,000 generated Z events, the fast Monte Carlo program is used to study the acceptance. Table 7.1 shows the decomposition of the detector loss and acceptance due to the various cuts including all p_T values of the electrons. The Z p_T dependences of the detector acceptance and selection effects are discussed in the following section. Heavy losses occur in the Intercryostat Region (ICR) as defined in section 4.4.2 (18.3% loss) and due to the kinematic (E_T) cuts (29% loss). The overall acceptance is 37.5%.

Cut	% of Events Lost	% of Events Left
$E_T^{e1} < 25$GeV	22.55	77.45
$E_T^{e2} < 25$GeV	8.36	70.97
e1 in phi crack	6.29	66.51
e2 in phi crack	5.92	62.57
$\mid \eta(e1) \mid > 2.5$	4.61	59.68
$\mid \eta(e2) \mid > 2.5$	4.80	56.82
e1 in ICR	17.24	47.02
e2 in ICR	18.08	38.52
$M_{ee} > 105$, or $M_{ee} < 75$	2.66	37.50

Table 7.1: Event loss and acceptance

7.3 Detector and Selection Effects

With 150,000 generated Z events, the fast Monte Carlo program is also used to study the detector and selection effects[1] on the p_T distribution. Two methods are shown below.

7.3.1 1 Dimensional (1-D) Study: The Detector Response Function

The detector response function $\mathbf{A(p_T)}$ is defined[2] as the ratio of dN/dp_T^{rec} and dN/dp_T^{true}:

$$\mathbf{A(p_T)} = \frac{\mathbf{dN/dp_T^{rec}}}{\mathbf{dN/dp_T^{true}}} \tag{7.1}$$

Figure 7.1 shows the detector response function $\mathbf{A(p_T)}$ using the fitted production model (with $g_2^0 + 2\sigma$) as described in section 6.4.

Figure 7.2 shows the decomposition of $\mathbf{A(p_T)}$ for the various cuts, where we apply each cut step by step and calculate the $\mathbf{A(p_T)}$ at each step,

[1] For the $d\sigma/dp_T$ measurement, the tight-loose cuts (i.e. one electron is required to pass the tight electron ID cut and another electron is required to pass the loose cut) for electron ID are used to improve the statistics. The corresponding efficiencies are used for the fast MC. There are about 13% of the Z events with second electron without a track in this sample and the directions of these electrons are simulated with the calorimeter angular resolutions in the Monte Carlo.

[2] Bold letters denote 1 dimensional array.

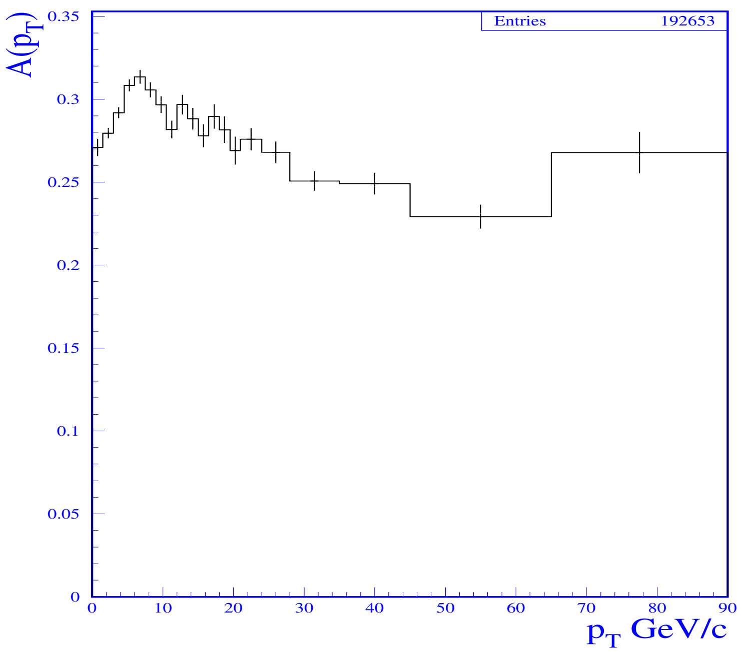

Figure 7.1: Detector response function $\mathbf{A(p_T)}$. The binning is as same as in the 2-D study discussed in the following section. The error bars indicate the statistical uncertainties of the MC sample.

the numerator in calculating $\mathbf{A(p_T)}$ at the previous step becomes the denominator of the next step.

The resolution smearing is responsible for the bump around 7 GeV/c as shown in Fig. 7.2(a) because the smearing only pushes the Z p_T up at low p_T due to the fact that Z p_T is always positive and spreads out in both directions as p_T increases. Figure 7.2(b) shows that the detector

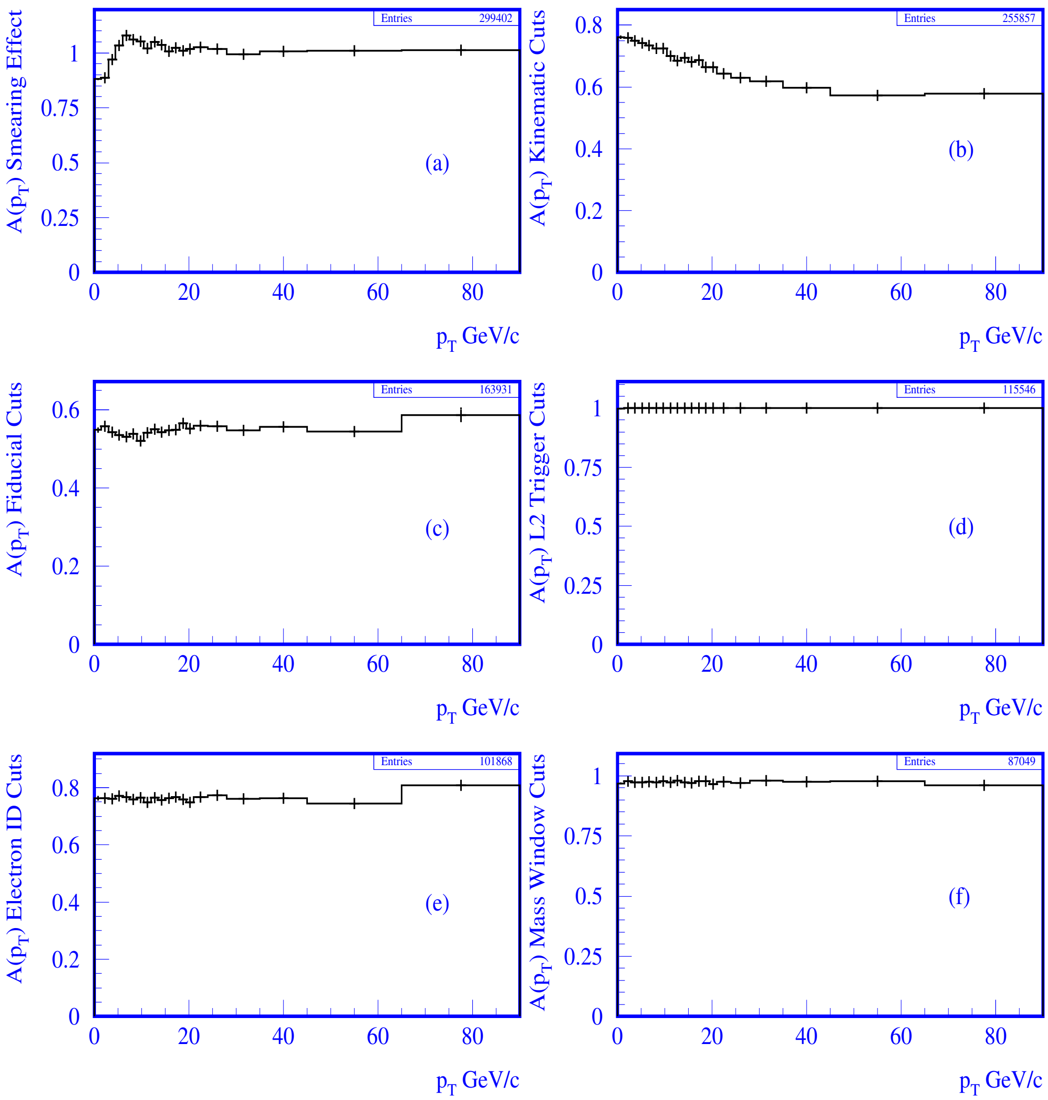

Figure 7.2: Decomposition of $\mathbf{A(p_T)}$. (a): smearing effect, (b): kinematic cut effect, (c): fiducial cut effect, (d): trigger effect, (e): electron ID cut effect, (f): mass window cut effect. The binning is as same as in the 2-D study discussed in the following section. The error bars indicate the statistical uncertainties of the MC sample.

acceptance decreases as a function of Z p_T due to the kinematic cut, because one decay electron of a high p_T Z is boosted while the other electron is deboosted, and the kinematic cut requires Z event with both electron E_T above 25 GeV. The detector acceptance is found to be flat as a function of Z p_T due to the fiducial cuts, trigger, electron ID cuts, and mass window cut, as shown in Fig. 7.2(c), 7.2(d), 7.2(e), and 7.2(f).

7.3.2 2 Dimensional (2-D) Study: Matrix Method

Figure 7.3 shows the 2-D detector and selection effects by plotting the reconstructed p_T vs. generated p_T for each event. The fitted production model[3] is used in the MC.

The smearing matrix[4] S_{ij} as shown in the vertical dimension of Fig. 7.3(a) is obtained by normalizing the reconstructed p_T distribution for a given input (generated) p_T bin with the total number of events generated in that bin. All detector resolution and acceptance, and event selection effects are present in the reconstructed p_T distribution.

[3]See section 6.2 for the choices of other variables in making the model. The HMRS(B) pdf is the default choice.

[4]`The data file is located (in WWW) at`
`http://d0sgi0.fnal.gov/publications_talks/thesis/jiang/smearing_matrix.dat.`

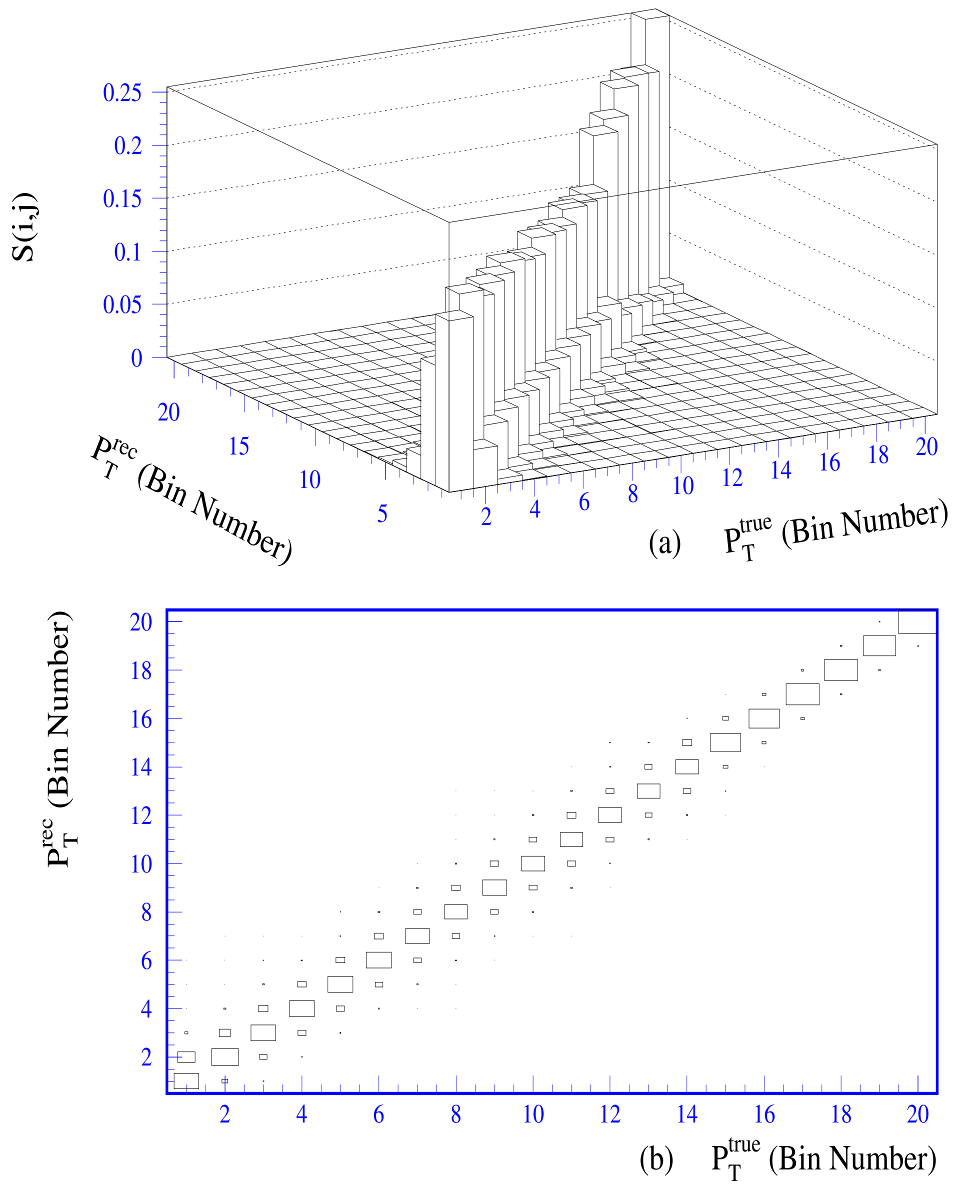

Figure 7.3: Smearing Matrix. (a): Lego plot, (b): 2-D box plot. The size of the box is proportional to the height of Fig.(a).

7.4 The procedure for obtaining $d\sigma/dp_T$

7.4.1 1-D Method

After the detector smearing, if an input p_T distribution can be found with good fit to the raw p_T data, then the input p_T distribution should be equal to the unfolded p_T distribution. With the $\mathbf{A(p_T)}$ by the fitted production model, the $d\sigma/dp_T$ can be calculated as:

$$\mathbf{d\sigma/dp_T} = \frac{\mathbf{dN(Z \to e^+e^-)/dp_T}}{\mathbf{A(p_T)} \cdot \mathrm{B} \cdot \int \mathcal{L} dt} \tag{7.2}$$

where B= 0.03366[18] is the $Z \to e^+e^-$ branching fraction, and $\int \mathcal{L} dt$= 12.8 ± 0.7 pb^{-1} is the integrated luminosity[5].

In this analysis, we only use the $\mathbf{A(p_T)}$ to estimate the systematic errors. A 2-D method discussed in the following section is believed to be less sensitive to the assumption of production model for the fast MC and used for obtaining $d\sigma/dp_T$.

[5]Only a subset of the data on tape is used, to reduce the uncertainties of the luminosity and electron ID efficiency measurements. We excluded data from the first three months of data taking, when we were trying to understand the detector and optimize the data taking condition and procedure.

7.4.2 2-D Method

We use multidimensional unfolding method based on Bayes's Theorem[36] which allows us to unfold any smeared distributions, given the smearing matrix, without the prior knowledge of the true distribution.

Principle of the 2-D Method

Let's define the smearing and unfolding matrices as S_{ij} and M_{ji} respectively, and the true and reconstructed p_T distributions as:

$$\mathbf{n} = \mathbf{dN/dp_T^{true}}, \mathbf{n}' = \mathbf{dN/dp_T^{rec}}. \tag{7.3}$$

We define:

$$n_j' = \sum_i S_{ij} \cdot n_i, \tag{7.4}$$

and

$$n_i = \sum_j M_{ji} \cdot n_j'. \tag{7.5}$$

Bayes's Theorem[35] states that M_{ji} can be expressed in terms of S_{ij} as:

$$M_{ji} = \frac{S_{ij} \cdot n_i}{\sum\limits_l S_{lj} \cdot n_l} \tag{7.6}$$

Since the true distribution is not known, a trial p_T distribution n_i^{trial} can be used to begin with. Substituting equation 7.6 into equation 7.5, we obtain:

$$n_i^{true*} = \sum_j \frac{S_{ij} \cdot n_i^{trial}}{\sum_l S_{lj} \cdot n_l^{trial}} \cdot n_j^{'} \qquad (7.7)$$

where n_i^{true*} is closer to the true p_T distribution than n_i^{trial}.

The iterative procedure is then used to get the true distribution. The procedure can be stated as the following:

1. choose the initial distribution of $\mathbf{n^{trial}}$;
2. calculate $\mathbf{n^{true*}}$;
3. make a χ^2 comparison between $\mathbf{n^{trial}}$ and $\mathbf{n^{true*}}$, where χ^2 is defined as:
$$\chi^2 = \sum_i \frac{(n_i^{trial} - n_i^{true*})^2}{n_i^{trial} + n_i^{true*}}; \qquad (7.8)$$
4. replace $\mathbf{n^{trial}}$ by $\mathbf{n^{true*}}$; and start again; if, after the second iteration the value of χ^2 is "small enough" [6], stop the iteration; otherwise go to step 2.

Smoothing the results of the unfolding with a continuous and smooth function before feeding them in the next step as the new trial distribution helps to avoid large fluctuations and make the procedure converge.

7.5 $d\sigma/dp_T$ Measurement

The $d\sigma/dp_T$ measurements described in the following sections are based on the 2-D method.

[6] The χ^2 value is set at $2 \cdot 10^{-2}$ in this analysis for 20 degrees of freedom.

7.5.1 Test of the 2-D Method

The fast Monte Carlo program is used to test if a reconstructed p_T distribution can be unfolded by the 2-D method back to a generated (true) distribution using the smearing matrix S_{ij} in Fig. 7.3.

Figure 7.4 shows how well this program works. Using MC events generated with the fitted production model, we apply the 2-D unfolding method on the reconstructed p_T distribution using a flat distribution as the initial trial distribution. The reconstructed p_T distribution contains all detector effects (fiducial cuts, electron ID efficiencies etc.) After 5 iterations, the χ^2 between the $\mathbf{n}^{\mathbf{true}*}$ of the next to last step and the $\mathbf{n}^{\mathbf{true}*}$ of the last step becomes 10^{-3}. A functional form[37]:

$$\frac{d\sigma}{dp_T} = \frac{A \cdot p_T}{(p_T^2 + B)^C \cdot [(Dp_T)^E + 1]} \tag{7.9}$$

where A, B, C, D, and E are free parameters is used to smooth the unfolded distribution before feeding it into the next step as the new trial distribution.

The exact solution is difficult to achieve, because of the finite statistical precision of the smearing matrix elements, and the fact that we are attempting to approximate the inversion of this 20 by 20 matrix. The resulting biases are discussed in section 7.6.2 below.

7.5.2 Unfolding of the Measured dN/dp_T Distribution

Now we are ready to apply the 2-D method to the measured dN/dp_T distribution after background subtraction. The total background rate (f) in the Z data sample after the tight-loose electron ID cuts is estimated to be $4.0\% \pm 1.4\%$[38].

The binning of the p_T distribution is determined as a compromise of the detector resolution and the statistical precision. Ideally, with an infinite amount of data, the smaller the bin sizes, the better. But due to the limited number of Z events, we must consider the correlation between the statistical errors and bin sizes. We also need to take the p_T resolution of 1.4 GeV/c as shown in Fig. 6.4 into consideration. We chose 1.5 GeV/c binning for up to 21 GeV/c of Z p_T to be consistent with the p_T resolution and make the statistical uncertainties below 10% around the peak position so that the difference of the number of events between the adjacent bins in that region is larger than the statistical uncertainties. At higher p_T ($p_T > 21$ GeV/c) , bin sizes of 3, 4, 7, 10, 20, and 25 GeV/c are chosen. After 3 iterations, the unfolding procedure converges and the unfolded p_T distribution is divided by $B \cdot \int \mathcal{L} dt$ to normalize to $d\sigma/dp_T$. The results are shown in Fig. 7.5 and Fig. 7.6. The unfolded data is compared with the Arnold-Kauffman theoretical band, which means any curve inside the band is within the allowed theoretical error; and the default theoretical prediction from Ladinsky-Yuan (dotted curve). The

Arnold-Kauffman theoretical band is established by considering:

- The effect of non-perturbative physics. At small p_T, when $p_T < \Lambda_{\mathrm{QCD}}$, confinement effects set in and α_s blows up. These non-perturbative effects are parameterized and are accounted for in the resummation procedure. Different choices of the parameterization leads to a p_T dependent variation in the predicted $d\sigma/dp_T$. The variation is taken as a theoretical error. It is $\approx 40\%$ at $p_T = 1$ GeV/c, and reduces to about 2% at $p_T = 10$ GeV/c.
- The choice of structure function and Λ_{QCD}. The result using HMRS(B) set with $\Lambda_{\mathrm{QCD}} = 190$ MeV is different from that using HMRS(E) set with $\Lambda_{\mathrm{QCD}} = 100$ MeV by 10 to 15 %. This effect is expected to shift $d\sigma/dp_T$ prediction up and down rather uniformly over all p_T.
- The contributions from higher order processes. For the matching result, an estimate of the higher order contributions is simply taken as the difference between the matched and the perturbative results at $p_T = 50$ GeV/c. This procedure gives an uncertainty of $\approx 10\%$ from neglecting higher order contributions.
- The choice of renormalization and factorization scales. The uncertainty is estimated by choosing $Q^2 = M_Z^2$ and $Q^2 = p_T^2$. The difference in the perturbative result is $\approx 10\%$.

As shown in Fig. 7.5 and Fig. 7.6, the unfolded data agree with the theoretical calculations. The agreement is however not perfect, as our data favor a slightly harder $d\sigma/dp_T$ at the low p_T region.

7.6 The Uncertainties of the $d\sigma/dp_T$ Measurement

7.6.1 Estimation of the Statistical Uncertainties

After the iterative procedure described above has converged, one obtains the unfolded distribution **n**. Since the resolution smearing moved events from bin to bin, the unfolding procedure leads to correlation in the uncertainties.

Since the statistical uncertainty on the measured p_T distribution is given as:

$$\Delta n_i^{'} = \frac{\sqrt{dN_i^{'}}}{dp_T^i} \tag{7.10}$$

Then the statistical uncertainty on the unfolded p_T distribution is:

$$\Delta n_j = \sum_i M_{ji} \Delta n_i^{'} \tag{7.11}$$

and the covariance can be expressed as:

$$(\Delta n_i)(\Delta n_j) = \sum_{kl} M_{ki} \Delta n_k^{'} M_{lj} \Delta n_l^{'} \quad (7.12)$$

Given the fact that the number of events in each bin of the measured p_T distribution follows a Poisson distribution and is independent, the expectation value becomes:

$$\begin{aligned}
E_{ij} &= < (\Delta n_i)(\Delta n_j) > & (7.13)\\
&= < \sum_{kl} M_{ki} \Delta n'_k M_{lj} \Delta n_l^{'} > & (7.14)\\
&= \sum_{kl} M_{ki} M_{lj} (< \Delta n'_k >)^2 \delta_{kl} & (7.15)\\
&= \sum_{k} M_{ki} M_{kj} (< \Delta n'_k >)^2 & (7.16)\\
&= \sum_{k} M_{ki} M_{kj} \frac{n_k^{'}}{dp_T^k} & (7.17)
\end{aligned}$$

The square-root of the diagonal elements of E_{ij} gives the statistical errors for the unfolded p_T distribution.

7.6.2 Estimation of the Systematic Uncertainties

The sources of the systematic uncertainties are:

- the uncertainty of the integrated luminosity: $\int \mathcal{L} dt = 12.8 \pm 0.7$ pb^{-1},
- the uncertainty of the total background rate estimation: $f = 4.0\% \pm 1.4\%$,
- the errors of the unfolding method,

– the assumptions made in the fast Monte Carlo simulation.

Errors due to the Unfolding Method

The errors of the unfolding method have bin by bin structure and introduce biases to the unfolding result. The MC test results in Fig. 7.4 are used to estimate this biases as:

$$\frac{n^{\text{unfolded}} - n^{\text{true}}}{n^{\text{true}}} \tag{7.18}$$

The bin by bin biases and their statistical uncertainties are listed in Table 7.2. We correct the biases for our final unfolding result.

Errors due to the Assumptions Made in the Fast Monte Carlo Simulation

The following is a list of assumptions made in the fast Monte Carlo simulation, described in section 6.2.1 and their contributions to the uncertainties in the corrections for acceptance, selection efficiencies, and resolution smearing.

– **The Electron Selection Efficiencies**

  The electron selection efficiencies are the combined electron ID and tracking efficiencies. We increase or decrease them simultaneously within their uncertainties ($\pm\sigma$) as listed in Table 7.2. The resulting differences in $\mathbf{A}(\mathbf{p_T})$ are defined as the errors due to the electron selection efficiency uncertainties. The relative errors are calculated as:

$$\frac{\mathbf{A(p_T)}^{\varepsilon(+\sigma)} - \mathbf{A(p_T)}^{\varepsilon(-\sigma)}}{\mathbf{2} \cdot \mathbf{A(p_T)}^{\varepsilon}} \tag{7.19}$$

and the results are 4.8% for all p_T bins.

- **The Electron Energy Resolution**

  The amount of resolution smearing in the fast Monte Carlo simulation affects the smearing matrix and therefore the $d\sigma/dp_T$ result. For the electron energy resolution, we again increase or decrease the terms in the energy resolution parameterizations within its uncertainties ($\pm\sigma$) as listed in Table 5.6. For each variation, a new detector response function, $\mathbf{A(p_T)}$, is constructed using the fast Monte Carlo program. The resulting differences in $\mathbf{A(p_T)}$ are defined as the errors due to the electron energy resolution uncertainties. The relative errors can be calculated as:

$$\frac{\mathbf{A(p_T)}^{(+\sigma_\mathbf{E})} - \mathbf{A(p_T)}^{(-\sigma_\mathbf{E})}}{\mathbf{2} \cdot \mathbf{A(p_T)}} \tag{7.20}$$

  The results are smoothed (the relative errors are fitted) and the bin by bin errors are listed in Table 7.2.

- **The Electron Angular Resolution**

  Due to the uncertainties in our calculation of the angular resolutions (Table 5.4 and Table 5.5) we make the conservative estimation that the 1 σ uncertainty on each resolution is given by half its value.

We again increase or decrease the terms in the angular resolutions within their uncertainties ($\pm\sigma$). For each variation, a new detector response function, $\mathbf{A(p_T)}$, is constructed using the fast Monte Carlo program. The resulting differences in $\mathbf{A(p_T)}$ are defined as the errors due to the electron angular resolution uncertainties. The relative errors can be calculated as:

$$\frac{\mathbf{A(p_T)^{(+\sigma_{ang})} - A(p_T)^{(-\sigma_{ang})}}}{\mathbf{2 \cdot A(p_T)}} \tag{7.21}$$

The results are also smoothed and the bin by bin errors are again listed in Table 7.2.

- **The Input Production Model**

  To evaluate the errors introduced by the assumed production model in the fast Monte Carlo simulation, a model which has a flat p_T distribution is generated. Two smearing matrices, S_{ij}^{flat} and $S_{ij}^{assumed}$, are constructed using the flat and assumed model respectively.

  A reconstructed p_T distribution is unfolded using both S_{ij}^{flat} and $S_{ij}^{assumed}$. The unfolded p_T distributions by both matrices are shown in Fig. 7.7 and it is clear that the two results are almost identical and this error is negligible.

The errors due to the sources listed above are added to the diagonal elements of the covariance matrix, E_{ij}, in quadrature and the resulting matrix is the final covariance matrix[7], σ_{ij}. The square root of the diagonal elements of the final covariance matrix gives the bin by bin error for the unfolded p_T distribution.

Using the final covariance matrix, we can obtain a χ^2 when making comparisons with theoretical predictions. The χ^2 can be calculated as:

$$\chi^2 = \sum_{i,j}(D_i - T_i) \cdot \sigma_{ij}^{-1} \cdot (D_j - T_j) \tag{7.22}$$

where $D_{i,j}$ and $T_{i,j}$ are the data and theoretical predictions respectively.

The correlation coefficient[8] between neighboring bins is given by:

$$\rho_{ij} = \frac{\sigma_{ij}}{\sqrt{\sigma_{ii} \cdot \sigma_{jj}}} \tag{7.23}$$

The numerical results and the errors of the $d\sigma/dp_T$ measurement for each p_T bin are listed in Table 7.2. The errors due to luminosity (5.4%), total background rate (1.4%), and electron identification (4.8%) uncertainties are combined in quadrature to yield an overall error of 7.3%, which is not shown in Table 7.2.

[7] The data file is located (in WWW) at
`http://d0sgi0.fnal.gov/publications_talks/thesis/jiang/covariance_matrix.dat`.

[8] The data file is located (in WWW) at
`http://d0sgi0.fnal.gov/publications_talks/thesis/jiang/correlation_coefficient.dat`.

7.6.3 Fitting of the Unfolded p_T Distribution

The unfolded p_T spectrum is fitted with the functional form in equation 7.9 for fast reproduction of our result. The fitted values and their uncertainties for A, B, C, D, and E are shown in Table 7.3 when we choose the unit of p_T as GeV/c and the unit of $d\sigma/dp_T$ as pb/GeV/c in equation 7.9. The χ^2 defined in equation 7.22 is calculated to be 0.77 (for 20 degrees of freedom) between the unfolded data and this functional fit.

bin #	Δp_T	evts	$d\sigma/dp_T$	err1	bias	err2	errE	errA	$d\sigma^c/dp_T$	err tot
1	0-1.5	36	167	13.8	4.2	1.6	2.4	0.4	160	14.1
2	1.5-3	61	366	9.28	-4.6	1.1	2.2	0.4	383	9.61
3	3-4.5	103	484	8.21	-1.4	1.0	2.0	0.5	491	8.53
4	4.5-6	84	434	8.36	2.1	1.1	1.9	0.6	425	8.66
5	6-7.5	67	357	9.00	4.8	1.2	1.7	0.6	340	9.26
6	7.5-9	63	309	9.90	1.5	1.4	1.6	0.7	304	10.1
7	9-10.5	48	259	10.6	1.1	1.5	1.4	0.7	256	10.9
8	10.5-12	47	230	11.7	-2.2	1.7	1.3	0.8	235	11.9
9	12-13.5	35	181	12.7	-1.4	1.8	1.2	0.9	184	12.9
10	13.5-15	28	149	14.2	1.1	2.0	1.0	0.9	148	14.4
11	15-16.5	25	126	15.4	-1.4	2.1	0.9	1.0	128	15.6
12	16.5-18	18	103	16.6	-1.7	2.3	0.8	1.1	104	16.8
13	18-19.5	19	98	18.3	-0.6	2.6	0.7	1.1	99	18.5
14	19.5-21	17	88	18.9	-1.1	2.7	0.6	1.2	89	19.1
15	21-24	23	65	27.2	1.6	3.7	0.5	1.3	63	27.4
16	24-28	22	45	35.6	-1.1	4.6	0.3	1.5	45	35.9
17	28-35	17	22	54.2	-1.2	6.1	0.1	1.7	23	54.5
18	35-45	14	13	75.2	-0.5	8.7	0.0	2.1	13	75.7
19	45-65	21	10	95.5	1.3	14.9	0.2	2.7	10	96.7
20	65-90	8	2.8	171.	4.6	26.1	2.1	4.2	2.7	173

Table 7.2: $d\sigma/dp_T$ measurement result and errors. Column 1 gives the bin number, column 2 (Δp_T) gives the p_T range in GeV/c, column 3 (evts) gives the observed events in each bin, column 4 ($d\sigma/dp_T$) gives the measured differential cross section in pb/GeV/c, column 5 (err1) gives the relative statistical errors for $d\sigma^c/dp_T$ in percentage, column 6 (bias) gives the relative biases introduced by the unfolding method in percentage, column 7 (err2) gives the relative statistical errors of the column 6 in percentage, column 8 (errE) gives the relative errors from the uncertainties of the energy resolutions in percentage, column 9 (errA) gives the relative errors from the uncertainties of the angular resolutions in percentage, column 10 ($d\sigma/dp_T$) gives the differential cross section after correcting the unfolding biases in pb/GeV/c, and the last column gives the total relative errors in percentage by adding column 5, 7, 8, and 9 in quadrature.

	A	B	C	D	E
fit	96044	41.6	1.69	0.6	1.0e-3
δ fit	$\pm$ 30520	$\pm$ 4.8	$\pm$ 0.05	$\pm$ 0.5	$\pm$ 0.5 e-3

Table 7.3: The fit parameters of parameterizations for the Z p_T spectrum.

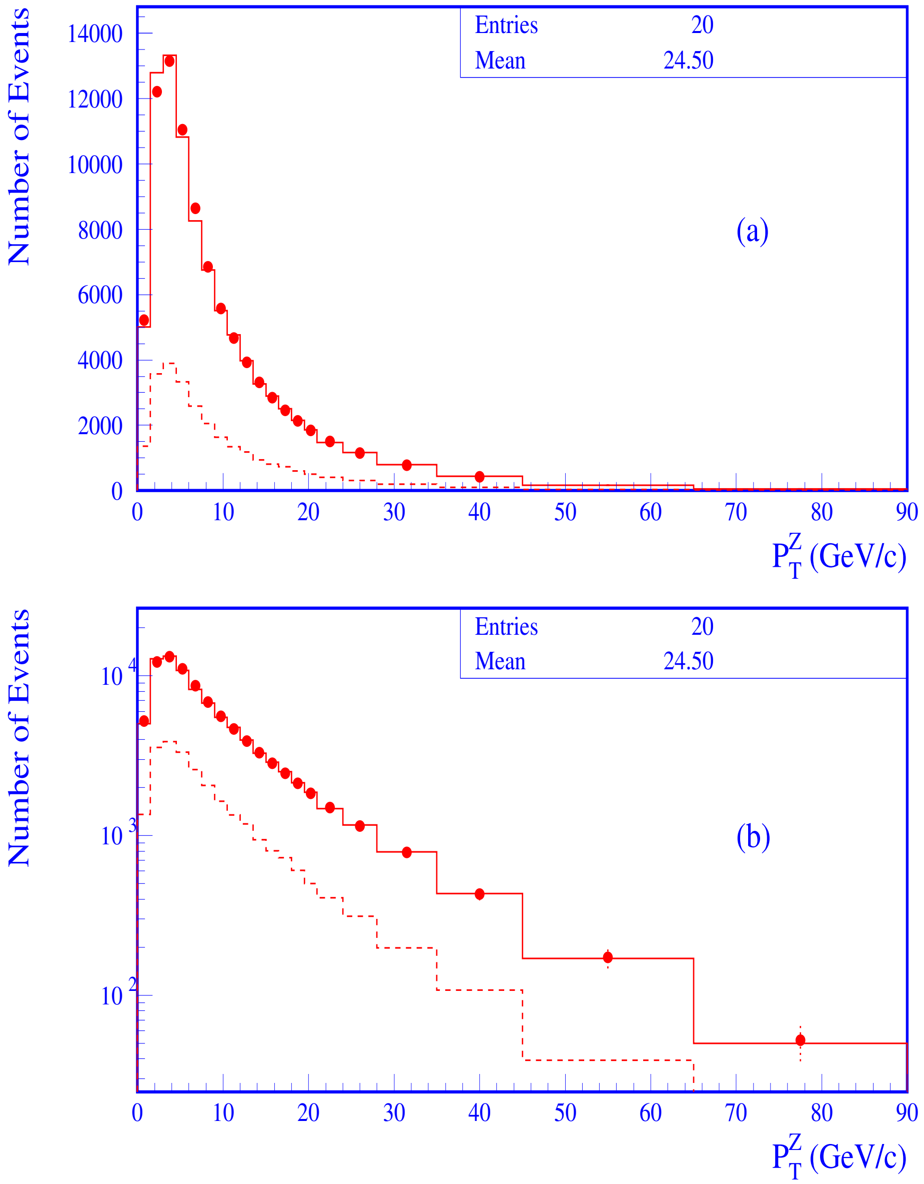

Figure 7.4: Test of the 2-D unfolding method. (a): Linear plot, (b): Semi-log plot. The dashed histograms are the reconstructed p_T distributions that contains all detector effects (fiducial cuts, electron ID efficiencies etc.), the dots are the unfolded p_T distributions, and the solid histograms are the input p_T distributions as references. Again the fitted production model is used in generating the MC events.

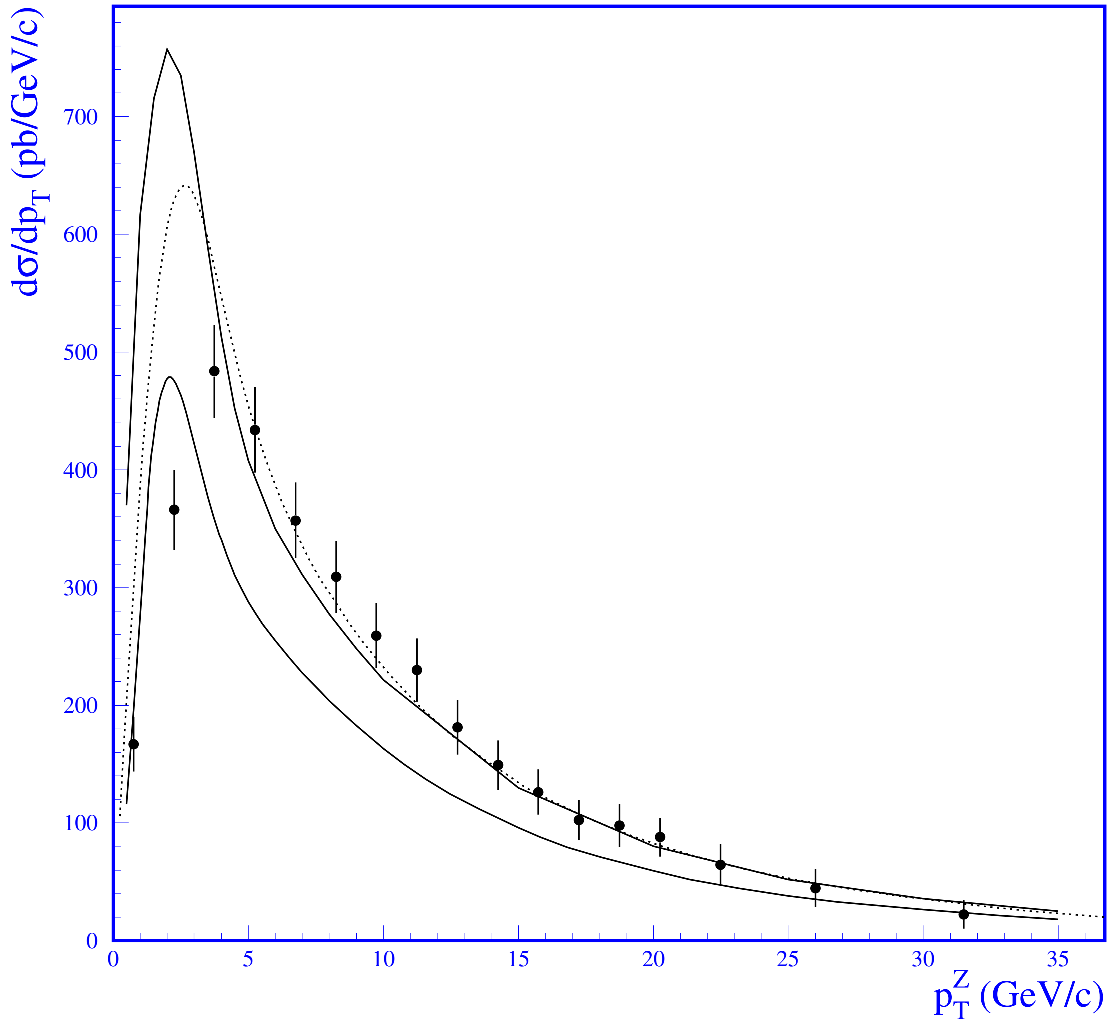

Figure 7.5: $d\sigma/dp_T$ measurement (linear plot to focus on the low p_T region). The dots are the unfolded data, the solid curves are the Arnold-Kauffman theoretical bands, any curve inside the band is within the allowed theoretical error. The dotted curve is the prediction from Ladinsky-Yuan (CTEQ2M pdf). The error bars on the data points represent statistical errors only (see section 7.6.1 for details).

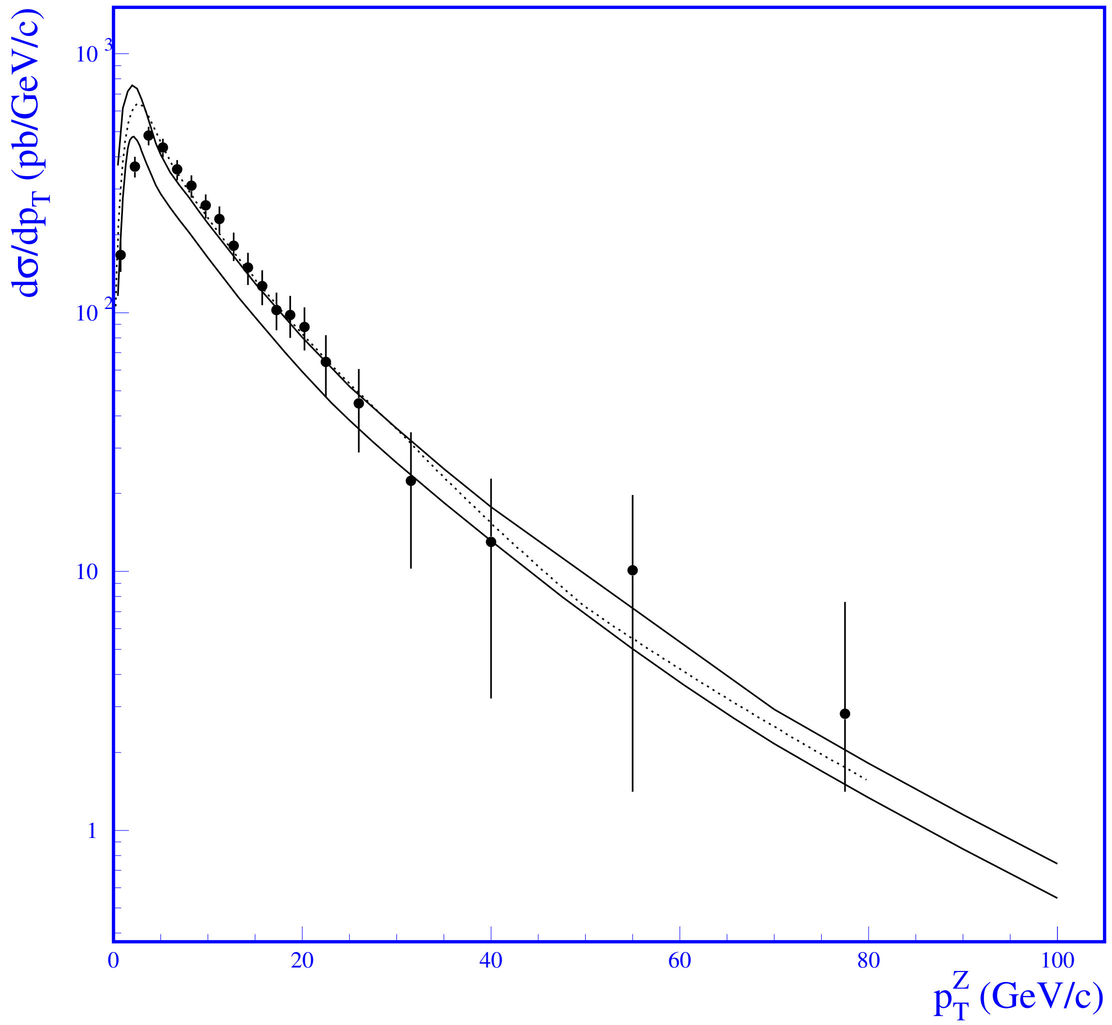

Figure 7.6: $d\sigma/dp_T$ measurement (semi-log plot). The dots are the unfolded data, the solid curves are the Arnold-Kauffman theoretical bands, any curve inside the band is within the allowed theoretical error. The dotted curve is the prediction from Ladinsky-Yuan (CTEQ2M pdf). The error bars on the data points represent statistical errors only (see section 7.6.1 for details).

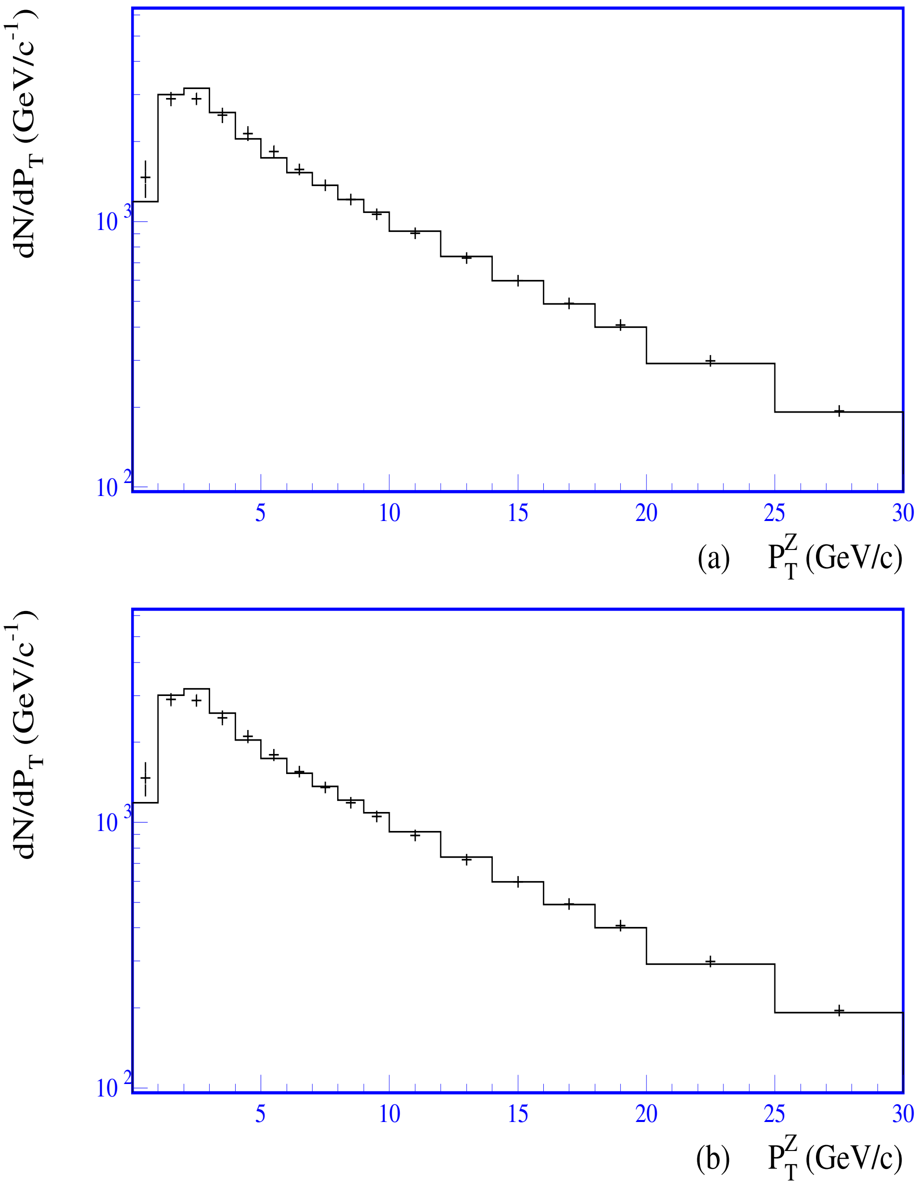

Figure 7.7: The dependence of the unfolding result on the input production models in constructing S_{ij}. The histograms are the input distributions and the points are the unfolded distributions. (a): using S_{ij}^{flat}, (b): using $S_{ij}^{assumed}$.

Chapter 8

Conclusion

We have measured the inclusive distribution of the transverse momenta (p_T) of Z bosons produced in $p\overline{p}$ interactions at $\sqrt{s} = 1800$ GeV. The reconstructed p_T distribution has been unfolded to take into account the effects of our experimental resolution, acceptance, and efficiency, enabling a measurement of the differential cross section $d\sigma/dp_T$ for Z boson production. Theoretical predictions of this differential cross section require resummation techniques at low p_T which incorporate nonperturbative (i.e. uncalculable) phenomena using previous data in Drell-Yan ($q\overline{q}$ annihilation) processes. Our data prefer a harder p_T spectrum than predicted by these models. Using the Ladinsky-Yuan parameterization[15] we obtain a good fit to our data by varying only the g_2 parameter to the value of 0.78 ± 0.1 GeV^2.

Bibliography

[1] Val L. Fitch and Jonathan L. Rosner, Elementary Particle Physics in the Second Half of the 20th Century, Chapter 6 of *Twentieth Century Physics* (eds. L.M. Brown, A. Pais and B. Pippard (IOP/AIP, Philadelphia, 1994).

[2] S.L. Glashow, Nucl. Phys. **B22**, (1961)579; A. Salam in Proc. 8th Nobel Symposium, p.367, ed. N.Svertholm (Almqvist and Phys. Wiksell, Stockholm, 1968); S. Weinberg, Phys. Rev. Lett. **19**, (1967)1264; S.L. Glashow, J.Iliopoulos, and L. Maiani, Phys. Rev. **D2**, (1970)1285.

[3] See for example, Donald H. Perkins, Introduction to High Energy Physics, Addison-Wesley Publishing Company, 1982, pp 353.

[4] UA1 Collaboration, G.Arnison *et al.*, Phys. Lett. **122B**, (1983)103; UA2 Collaboration, M.Banner *et al.*, Phys. Lett. **122B**, (1983)476; UA1 Collaboration, G.Arnison *et al.*, Phys. Lett. **126B**, (1983)398; UA2 Collaboration, P.Bagnaia *et al.*, Phys. Lett. **129B**, (1983)130.

[5] The LEP collaborations: ALEPH, DELPHI, L3 and OPAL. Phys. Lett. **B276**, 247 (1992).

[6] LEP report LEPEWWG/94-02, 12 July 1994, submitted to 27th International Conference on High Energy Physics, Glascow, Scotland, 20-27 July 1994.

[7] SLD Collaboration, K. Abe *et al.*, Phys. Rev. Lett. **73**(1994)23.

[8] DØ Collaboration, S. Abachi *et al.*, Fermilab report FERMILAB-CONF-93-396-E, December 1993, presented by Q. Zhu at Ninth Topical Workshop on Proton-Antiproton Collider Physics, Oct. 18-22, 1993.

[9] DØ Collaboration, S. Abachi *et al.*,presented by N. Graf at Ninth Topical Workshop on Proton-Antiproton Collider Physics, Oct. 18-22, 1993.

[10] DØ Collaboration, S. Abachi *et al.*, Phys. Rev. Lett. **74**, (1995)2632; CDF Collaboration, F. Abe *et al.*, Phys. Rev. Lett. **74**, (1995)2626.

[11] A.S. Ito *et al.*, Phys. Rev. **D23**(1981)604.

[12] J. Collins, D. Soper and G. Sterman, *Nucl. Phys.* **B250** (1985) 199.

[13] P. B. Arnold and R. P. Kauffman, *Nucl. Phys.* **B349**(1991)381; P. B. Arnold and M. H. Reno, *Nucl. Phys.* **B319** (1989)37.

[14] See for example, Francis Halzen and Alan D. Martin, Quarks and Leptons: An Introductory Course in Modern Particle Physics, John Wiley & Sons, Inc., 1984, pp 248.

[15] G. A. Ladinsky and C.-P. Yuan, Phys. Rev. bf D50(1994)R4239.

[16] C. Davies, B. Weber and W.J. Stirling, *Nucl. Phys.* **B256** (1989)413.

[17] J. Paradiso, PhD thesis, Massachusetts Institute of Technology (1981).

[18] *Review of Particle Properties*, Phys. Rev.**D50**(1994)1173.

[19] S. Abachi, *et al.*, Nucl. Instr. Meth. **A338**, pp 185-253 (1994).

[20] Design Report, The DØ Experiment at the Fermilab $p\overline{p}$ collider, November 1984.

[21] J.F. Detoeuf *et al.*, Nucl. Instr. and Methods in Phys. Res. **A265**, 157 (1988); **A279**, 310 (1989).

[22] E. Flattum, private communication.

[23] H. Aihara *et al.*, *Design, Construction, and Performance of the Electromagnetic Module of the DØ End Calorimeter*, Nucl. Instr. & Meth. **A 325**, 393 (1993).

[24] R. Engelmann *et al.*, Nucl. Instr. and Methods **216**, 45 (1983).

[25] M. Narain, *Proceedings of the DPF'92 meeting at Fermilab*, 1678.

[26] W.G.D. Dharmaratna, Terry Heuring, DØ Note **1577** , Dec. 1992.

[27] P. Grudberg, private communication.

[28] E. Kearns, PhD thesis, Harvard University, June 1990 (unpublished).

[29] G. Eppley, private communication.

[30] T. Sjöstrand. Computer Physics Commun. **82**, 74(1994).

[31] J. Sculli, private communication. The framework of this fast Monte Carlo program was originally written by Prof. John Sculli. It has been modified to accommodate some of the features discussed in this thesis.

[32] Q. Zhu, PhD thesis, New York University, April 1994 (unpublished).

[33] J. Sculli, private communication.

[34] J. Alitti, *et al.*, Z. Phys. C **47**, pp 523, 1990.

[35] See for example, D. Moore and G.P. McCabe, Introduction to the Practice of Statistics, W.H. Freeman and Company. 1993.

[36] G.D'Agostini, DESY 94-099, June 1994, A Multidimensional Unfolding Method Based on Bayes's Theorem.

[37] Similar functional form can be found in J.S.T. Ng, PhD thesis, Harvard University, June 1991 (unpublished) and B. Winer, PhD thesis, University of California, Berkeley, 1991 (unpublished).

[38] J. Yang, PhD thesis, New York University, May 1995 (unpublished).